Accepted Manuscript

Ruthenium(II)-arene complexes with monodentate aminopyridine ligands: Insights into redox stability and electronic structures and biological activity

Flávia Marszaukowski, Ivelise Dimbarre Lao Guimarães, Juliana Paula da Silva, Luis Henrique da Silveira Lacerda, Sergio Ricardo de Lazaro, Márcio Peres de Araujo, Patrícia Castellen, Tania Toyomi Tominaga, René T. Boeré, Karen Wohnrath

PII: S0022-328X(18)30775-7

DOI: https://doi.org/10.1016/j.jorganchem.2018.11.036

Reference: JOM 20656

To appear in: *Journal of Organometallic Chemistry*

Received Date: 4 September 2018

Revised Date: 28 November 2018

Accepted Date: 30 November 2018

Please cite this article as: Flá. Marszaukowski, I.D. Lao Guimarães, J.P. da Silva, L.H. da Silveira Lacerda, S.R. de Lazaro, Má.Peres. de Araujo, Patrí. Castellen, T.T. Tominaga, René.T. Boeré, K. Wohnrath, Ruthenium(II)-arene complexes with monodentate aminopyridine ligands: Insights into redox stability and electronic structures and biological activity, *Journal of Organometallic Chemistry* (2019), doi: https://doi.org/10.1016/j.jorganchem.2018.11.036.

Ruthenium(II)-arene complexes with monodentate aminopyridine ligands: insights into redox stability and electronic structures and biological activity†

Flávia Marszaukowski[a], Ivelise Dimbarre Lao Guimarães[a], Juliana Paula da Silva[a], Luis Henrique da Silveira Lacerda[a], Sergio Ricardo de Lazaro[a], Márcio Peres de Araujo[b], Patrícia Castellen[a], Tania Toyomi Tominaga[c], René T. Boeré[d] and Karen Wohnrath[a]*

Graphical abstract

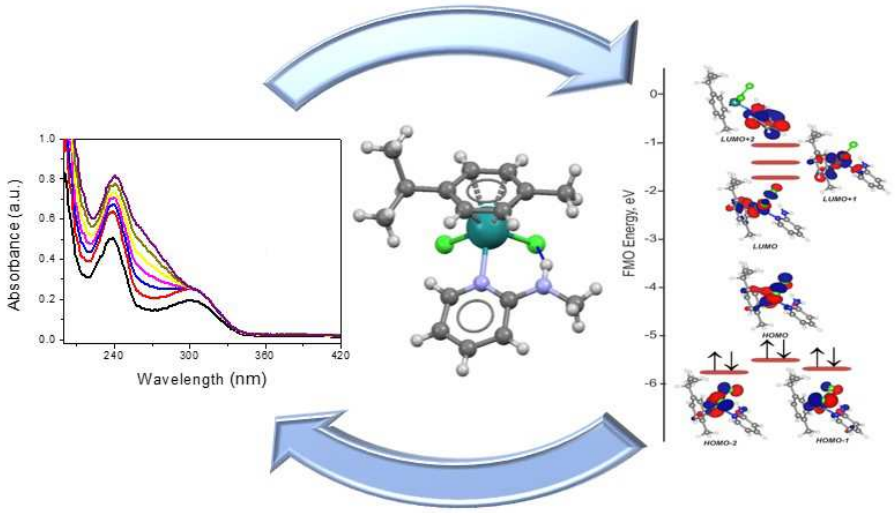

Ruthenium(II)-arene complexes with monodentate aminopyridine ligands: insights into redox stability, electronic structures and biological activity†

Flávia Marszaukowski[a], Ivelise Dimbarre Lao Guimarães[a], Juliana Paula da Silva[a], Luis Henrique da Silveira Lacerda[a], Sergio Ricardo de Lazaro[a], Márcio Peres de Araujo[b], Patrícia Castellen[a], Tania Toyomi Tominaga[c], René T. Boeré[d] and Karen Wohnrath[a]*

[a] *Departamento de Química, Universidade Estadual de Ponta Grossa, Av. Gal. Carlos Cavalcanti, 4748, Uvaranas, CEP 84030-900, Ponta Grossa - PR, Brasil.*

[b] *Departamento de Química, Universidade Federal do Paraná, Rua Coronel Francisco Heraclito dos Santos, 100 - Jardim das Américas, CEP 81531-990, Curitiba – PR, Brasil.*

[c] *Departamento de Física, Universidade Estadual do Centro-Oeste, Rua Simeão Camargo Varela de Sá, 03, Vila Carli, CEP 85040-080, Guarapuava – PR, Brasil.*

[d] *Department of Chemistry and Biochemistry, University of Lethbridge, 4401University Drive, Lethbridge, Alberta, Canada T1K 3M4*

† Supplementary information (SI) available: X-ray crystallography data; DFT computed and crystallographic structure depictions; vibrational spectroscopic data; archival NMR data; Uv-vis spectroscopic data; solubility and stability of the complexes; additional cyclic voltammograms and scan-rate studies; biological data and literature survey; Cartesian coordinates of DFT geometries. CCDC 1822445. For SI and crystallographic data in CIF or other electronic format see DOI: xxxxxx

*Corresponding author: Karen Wohnrath. karen.woh@gmail.com
Phone: +55 (42) 3220-3731

Abstract

The synthesis and spectroscopic characterization of four ruthenium(II) arene complexes with monodentate pyridine derivatives ([(^{6}–*p*-cymene)$RuCl_2L$]: L = 2-aminopyridine, 2-methylaminopyridine, 2-benzylaminopyridine, and pyridine) are reported. Full characterization was undertaken using ^{1}H and ^{13}C NMR spectroscopy, vibrational and electronic spectroscopies and crystallography (2-methylaminopyridine derivative). UB3LYP//(6-31+G(d),SPK-DZCD) density functional theory calculations determined the molecular and electronic structures. Cyclic voltammetry determined a large electrochemical stability window (>2.2 V) extending well beyond the physiological E°. Interactions with CT-DNA and BSA, and activity against four cell lines (HeLa, B16F10, HEp-2 and Vero) were evaluated. The 2-methylaminopyridine shows weak cytotoxicity (IC_{50} = 346 mol L^{-1}) towards HeLa cells. All the complexes interact with DNA at relatively high concentrations as determined by UV-vis spectroscopic titration. Results of circular dichroism spectroscopy, ethidium bromide competition, fluorescence spectroscopy and DNA viscosity measurements identify electrostatic interactions between partly hydrolyzed cationic complexes and the phosphate backbone of DNA as the most likely interaction mode. Slower rates of hydrolysis may be the origin of lower cytotoxicity for ^{1} these complexes.

Keywords:

Ruthenium(II)-arene; pyridine ligands; DNA interaction; BSA interaction; cytotoxicity; crystal structure.

Abbreviations table

B16F10
Murine melanoma cell line

BSA
Bovine serum albumin

CT-DNA
Calf-Thymus deoxyribonucleic acid

DMSO
Dimethyl sulfoxide

EtBr
Ethidium bromide

HeLa
Cervical carcinoma cell line

HEp-2
Laryngeal carcinoma cell line

PBS
Phosphate buffer

RAPTA
Ruthenium arene PTA

TBAP
Tetrabutylammonium perchlorate

Vero
Kidney murine cell line

1. Introduction

Interest in utilizing ruthenium-based metal complexes as vital new drugs for the treatment of cancer, either to replace platinum therapies where resistance has developed or to expand the therapeutic range of tumor types, remains very strong [1-9]. Whereas all the platinum-based drugs in clinical use are based on square-planar L_2PtCl_2 in the classic *cis* configuration, the range of structures, ligand-types and geometries of ruthenium complexes which have demonstrated anti-proliferative action is extremely diverse. In this regard, a strong warning has recently been given against making false generalizations (low toxicity because of similarity to iron; slow rates of ligand exchange; activation is by reduction to Ru(II); specific accumulation in cancerous tissues; uptake mediated by transferrin) about ruthenium cytotoxic agents [7]. In short, different types of ruthenium-based metallodrugs are under investigation, with distinctive behaviors. One class of ruthenium complex that differs significantly in structure and properties from the platinum-type agents are (^{6}-arene)ruthenium(II) tripodal organometallic complexes, the vast majority of which have either one (type A) or two (type B: E = NR) nitrogen donor ligands (Chart 1). The remaining coordination sites are almost always occupied by chlorides. The type A complexes are thus neutral ruthenium complexes with ^{1}-pyridyl ligands [1]. In the chelated type B complexes, the second donor group "E" is frequently nitrogen but can also be oxygen or carbon moieties [5]. There are now numerous derivates of type A where the nitrogen ligand is a simple pyridine group [10-19].

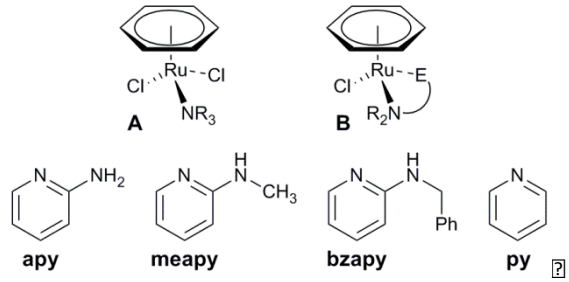

Chart 1 Structure types and ligands of importance to this work.

In the first step of a larger research program utilizing pyridine-based ligands of both types A and B, we wished to investigate the cytotoxicity of a selected series of simple neutral 2-aminopyridine complexes incorporating the ligands 2-aminopyridine (**apy)**, 2-methylaminopyridine **(meapy)** and 2-benzylaminopyridine **(bzapy)** (Chart 1). 2-Aminopyridines are important nitrogen-containing ligands due to a strong nitrogen

donor in the ring, while the aromatic amino substituent provides additional electronic and hydrogen-bonding stability. Such complexes have attracted considerable interest recently because of their applications in pharmaceutical research, for instance glucokinase activators [6] or selective inhibitors of neuronal nitric oxide synthase [21]. Herein we report on the synthesis, structures and biological activity of four [(^{6}-*p*-cymene)$RuCl_2L$] complexes **1** – **3** where L = **apy, meapy and bzapy**, respectively. In addition to cytotoxicity tests *in vitro* against cancer and normal cell lines (HeLa, B16F10, HEp-2 and Vero), studies on the interaction of the complexes with DNA and BSA were undertaken to search for understanding of biological activity. The long-known complex **4** of the parent ligand **py** was included for comparison to the aminopyridines [13,22-25]. Complex **4** did not display any cytotoxic effect as previously reported in the literature [26].

While this work was in progress, studies of a number of other type-A pyridine complexes appeared in the literature [24-28]. The biological properties of these analogues, in particular the substituted 2-phenylaminopyridine derivatives reported by Richter *et al*. [27], serve as interesting parallels to our results. By incorporating remote carboxylate donor groups at the 4-position of the NC_6H_4X rings, moderate antiproliferative activity was observed. A comparison of this closely parallel series with **1** to **4** (i.e. with and without these remote donor groups) proved helpful for delineating their structure-property relationships.

Quantum calculations on ruthenium complexes are relatively rare in the literature but there has been an increase in interest in using such such methods to investigate molecular structures [29-30] and catalysis [31] of Ru complexes. Kreitner and co-authors applied Density Functional Theory (DFT) in a study of excited state behaviour of cyclometalated *bis*(tridentate)ruthenium(II) complexes [32], while Das and co-authors investigated the interaction of aquated ruthenium(III) complexes with DNA base pairs using computational methods [33]. Herein we employ DFT computational methods to provide a basic understanding of the electronic structures of the title complexes to provide insights into their spectroscopic and redox behaviours *in vitro* and *in vivo*. To date, these aspects of ruthenium-arene complexes have been unduly ignored despite an intensive literature regarding their potential utility, or otherwise, as new antiproliferative agents.

2. Experimental section

2.1. Materials and general methods

$RuCl_3.3H_2O$ was purchased from Strem and the precursor complex [{(η^6-*p*-cymene)Ru(μ-Cl)Cl}$_2$] was prepared according to published procedures [34,35]. Ligands **apy**, **meapy, bzapy** and **py**, as well as α-phellandrene, calf thymus DNA (CT-DNA), bovine serum albumin (BSA) and tetrabutylammonium perchlorate (TBAP) were purchased from Sigma-Aldrich and used without further purification. The solvents were rigorously purified by standard procedures [36]. All synthesis manipulations were carried out under an argon atmosphere using modified Schlenk techniques.

2.2. Physical measurements

FT-IR spectra (4000-550 cm^{-1}) were recorded on a DRS-8000/Shimadzu IRPrestige-21 spectrometer. Raman spectra (40-4400 cm^{-1}) were obtained with a Bruker Senterra dispersive Raman microscope. UV-vis spectra (0.1 mmol) were recorded on a Varian Cary 50 Bio spectrophotometer using quartz cells, in the range 200-900 nm. Conductivity values were obtained using an Infolab WTW TetraCon® 325 conductivity bridge in a thermostated bath held at 25.0 °C. Aqueous solution of $1{\cdot}10^{-3}$ $mol{\cdot}L^{-1}$ NaCl was used as the 1:1 electrolyte standard, where the conductivity value for this solution was 124.7 $\mu S{\cdot}cm^{-1}$. [^{n}Bu$_4$N][ClO_4] was used similarly used as the standard in CH_3CN, for which the molar conductance is 197.1 $\mu S{\cdot}cm^{-1}$ [37]. X-ray crystallography was undertaken for complex **2** using Cu K_α radiation at 100 K on a Rigaku-Oxford Diffraction SuperNova diffractometer equipped with a Pilatus 200K HPAD detector. Details of the structure solution and refinement are provided in the SI. The structure is complicated by wholesale disorder of the **meapy** ligand, presence of $CHCl_3$ solvent and $Z' = 2$. CCDC 1822445 contains the supplementary crystallographic data for this paper.

1D and 2D solution-phase NMR experiments (^{1}H, ^{13}C, ^{1}H–^{1}H gCOSY, ^{1}H–^{13}C gHSQC, and ^{1}H–^{13}C gHMBC) were recorded on a Bruker Model DRX, 400 MHz spectrometer, at probe temperature using, in general, 20 mg samples of complexes dissolved in $CDCl_3$, containing a trace amount of tretramethylsilane (TMS) that was

used as an internal reference (0 ppm). The ^{1}H and ^{13}C NMR spectra were acquired with 16 and 2048 scans; spectral widths (sw) of 6393.862 and 25510.203 Hz; relaxation delays (d1) of 1 and 0.2 s; and 90° and 80° pulse lengths, respectively. The $^{1}H–^{1}H$ gCOSY, $^{1}H–^{13}C$ gHSQC and $^{1}H–^{13}C$ gHMBC, spectra were acquired with 8, 16, and 8 scans and spectral widths of 4595.588 for F2 and 18852.455 for F1, respectively. The relaxation delay of 1 s, with 256 data points at F1 and 4 K at F2 were the same in all 2D NMR experiments. Archival spectral data is presented in the SI.

2.3. Computational methodology

DFT calculations in gas phase, zero Kelvin and vacuum were carried out on **1** as an electronic model for all the complexes and on **2** to verify the geometry due to the disorder encountered in the X-ray diffraction study. All models were fully optimized from 10^{-6} Hartree and 10^{-8} Hartree for self-consistent field (SCF) based on the Hartree-Fock formalism and total energy criteria, respectively. Harmonic frequency calculations were undertaken to confirm that the geometries are at least local minima on the potential energy surface. Similar calculations were undertaken for $\mathbf{1}^{+}$ (doublet), $\mathbf{1}^{2+}$ (singlet and triplet), $\mathbf{1}^{-}$ (doublet) and $\mathbf{1}^{2-}$ (singlet and triplet) to help interpret the voltammetry results. In this study, all calculations were performed on GAUSSIAN09 program using B3LYP [38] functional with Gaussian-type 6-31+G(d) basis set for C, H, N, P, and F atoms; whereas the all-electron, relativistically corrected, Sapporo double-zeta (SPK-DZCD) basis set was applied to describe the Ru atom [39].

2.4. Electrochemistry

Cyclic voltammetric experiments were recorded on a potentiostat/galvanostat μAutolab (Type III, Metrohm-Eco Chemie) connected to a computer with GPES 4.9 (General Purpose Electrochemical System) software. The measurements were performed in nitrogen atmosphere at room temperature in dry CH_3CN with tetrabutylammonium perchlorate (TBAP Sigma-Aldrich) in $1.0\ 10^{-3}$ mol L^{-1} as a supporting electrolyte. The electrochemical cell was equipped with a glassy carbon (A = 3 mm^2) working electrode, a platinum foil auxiliary electrode and Ag/AgCl as the reference electrode in a Luggin capillary probe. Voltammograms were performed at a scan rate of 50 to 2000 V s^{-1}, with complex concentrations of 1 mM. The

ferrocenium/ferrocene redox couple was used as an internal reference ($E_{1/2}$ = 0.46 V *vs* Ag/AgCl).

2.5. Synthesis of complexes 1 - 4

Synthesis of [(η^6-*p*-cymene)$RuCl_2$(apy)] (**1**). Complex **1** was synthesized according to the literature method [40]. A solution of the precursor (100 mg, 0.16 mmol) with an excess of 2-aminopyridine (76 mg, 0.82 mmol) in toluene (10 mL) was stirred for 12 h at room temperature. The orange solid that precipitated was filtered off, washed with diethyl ether and dried under vacuum. Yield: 82 mg, 63%. Elemental analysis (%) calcd. for $C_{15}H_{20}Cl_2N_2Ru$ (400.34 g·mol^{-1}): C, 45.01; H, 5.04; N, 7.00. Found (%): C, 44.92; H, 5.17; N, 6.70. Its identity was established by agreement of the ^{1}H NMR and IR with the original report. ^{1}H NMR: (see Table 2). ^{13}C (400 MHz, $CDCl_3$, δ ppm): 18.21 (C^a); 22.27 (C^g); 30.49 (C^f); 81.70 (C^c); 82.97 (C^d); 97.75 (C^b); 103.05 (C^e); 112.21 (C^k); 114.04 (C^i); 138.47 (C^j); 152.24 (C^h); 162.59 (C^l). (FTIR, cm^{-1}): 3372 and 3290 $\nu_{asN\text{-}H}$ (w); 3040 $\nu_{asCsp^2\text{-}H}$ (w); 2966 and 2863 $\nu_{asCsp^3\text{-}H}$ (w); 1594 $\nu_{asC=N}$ (s); 1611, 1469 and 1438 $\nu_{asC=C}$ (s); 1251 $\nu_{C\text{-}H}$ (w); 1061 ν_{as}c (w); 753 $\delta_{C\text{-}H}$ (s). UV-vis. (CH_3CN, Max nm): 419 (420 mol^{-1}·L·cm^{-1}), 292 (5600 mol^{-1}·L·cm^{-1}), 233 (9200 mol^{-1}·L·cm^{-1}).

Synthesis of [(η^6-*p*-cymene)$RuCl_2$(meapy)] (**2**). A solution of the precursor (200 mg, 0.32 mmol) with an excess of 2-methylaminopyridine (173 mg, 1.60 mmol) in toluene (10 mL) was stirred for 4 h at room temperature. The orange solid that precipitated was filtered off, washed with diethyl ether and dried under vacuum. Yield: 238.7 mg, 88.5%. An analytical sample was obtained by vapour diffusion of diethyl ether into a concentrated $CHCl_3$ solution at RT (with some occluded $CHCl_3$). Elemental analysis (%) calcd. for $C_{16}H_{22}Cl_2N_2Ru$·0.17$CHCl_3$ (414.32 g·mol^{-1}): C, 44.68; H, 5.14; N, 6.45. Found (%): C, 44.25; H, 5.09; N, 6.64. Removal of residual $CHCl_3$ was achieved by redissolving and precipitating with diethyl ether. Final purity was monitored by very careful NMR measurements showing the absence of C or H containing impurities. ^{1}H NMR: (see Table 2). ^{13}C (400 MHz, $CDCl_3$, δ ppm): 18.14 (C^a); 22.50 (C^g); 30.12 (C^f); 30.51 (C^m); 82.07 (C^c); 82.74 (C^d); 97.34 (C^b); 103.47 (C^e); 108.81 (C^k); 113.28 (C^i); 138.99 (C^j); 153.62 (C^h); 163.13 (C^l). (FTIR, cm^{-1}): 3259 $\nu_{asN\text{-}H}$ (w); 3051 $\nu_{asCsp^2\text{-}H}$ (w); 2953 and 2870 $\nu_{asCsp^3\text{-}H}$ (w); 1573 $\nu_{asC=N}$ (s); 1615, 1473 and 1429 $\nu_{asC=C}$ (s); 1259 $\nu_{C\text{-}H}$ (w); 1073 ν_{as}c (w); 853 $\delta_{C\text{-}H}$ (s), 749 $\delta_{C\text{-}H}$ (s). UV-vis. (CH_3CN, Max nm): 419 (800 mol^{-1}·L·cm^{-1}), 305 (5400 mol^{-1}·L·cm^{-1}), 242 (22000 mol^{-1}·L·cm^{-1}).

Synthesis of [(η^6-*p*-cymene)$RuCl_2$(bzapy)] (**3**). Complex **3** was synthesized according to the literature method [40]. A solution of the precursor (200 mg, 0.32 mmol) with an excess of 2-benzylaminopyridine (300 mg, 1.60 mmol) in toluene (10 mL) was stirred for 4 h at room temperature. The orange solid that precipitated was filtered off, washed with diethyl ether and dried under vacuum. Yield: 237.4 mg (74.3%). Elemental analysis (%) calcd. for $C_{15}H_{20}Cl_2N_2Ru$ (400.34 g·mol^{-1}): C, 53.88; H, 5.34; N, 5.71. Found (%): C, 53.62; H, 5.37; N, 6.75. It proved impossible to obtain this complex in pure crystalline form and crystals suitable for X-ray diffraction could not be obtained. To obtain pure material, it was repeatedly dissolved and re-precipitated as an amorphous solid with ether, followed by vacuum drying. Finally, the identity and purity could be confirmed by very careful ^{1}H NMR analysis. ^{1}H NMR (see Table 2). ^{13}C (400 MHz, $CDCl_3$, δ ppm): 19.49 (C^a); 23.67 (C^g); 31.91 (C^f); 49.12 (C^m); 83.43 (C^c); 84.10 (C^d); 98.91 (C^b); 104.84 (C^e); 109.08 (C^k); 115.06 (C^i); 128.99 (C^p); 130.39 (C^o); 138.84 (C^n); 140.38 (C^j); 154.96 (C^h); 163.22 (C^l). (FTIR, cm^{-1}): 3238 ν_{asN-H} (w); 3046 ν_{asCsp^2-H} (w); 2953 and 2860 ν_{asCsp^3-H} (w); 1573 $\nu_{asC=N}$ (s); 1618, 1475 and 1434 $\nu_{asC=C}$ (s); 1237 ν_{C-H} (w); 1067 ν_{as}c (w); 843 δ_{C-H} (s), 763 and 703 δ_{C-H} (s). UV-vis. (CH_3CN, Max nm): 420 (600 mol^{-1}·L·cm^{-1}), 305 (4400 mol^{-1}·L·cm^{-1}), 242 (17200 mol^{-1}·L·cm^{-1}).

Synthesis of [(η^6-*p*-cymene)$RuCl_2$(py)] (**4**). The complex **4** was synthesized according to the previously reported method [41-42]. A solution of the precursor (100 mg, 0.16 mmol) with an excess of pyridine (30 mg, 0.37 mmol) in toluene (5 mL) was stirred for 4 h at room temperature. The orange solid that precipitated was filtered off, washed with diethyl ether and dried under vacuum. Yield: 108.5 mg (80.2%). Elemental analysis (%) calcd. for $C_{15}H_{20}Cl_2N_2Ru$ (400.34 g·mol^{-1}): C, 46.76; H, 4.97; N, 3.64. Found (%): C, 46.75; H, 4.74; N, 3.94. Its identity and purity were established by agreement of the ^{1}H NMR data with ref [40]. ^{1}H NMR (see Table 2). ^{13}C (400 MHz, $CDCl_3$, δ ppm): 19.61 (C^a); 23.71 (C^g); 32.08 (C^f); 83.68 (C^c); 84.26 (C^d); 95.51 (C^b); 104.99 (C^e); 125.94 (C^i); 138.97 (C^j); 156.36 (C^h). (FTIR, cm^{-1}): 3046 ν_{asCsp^2-H} (w); 2963 and 2852 ν_{asCsp^3-H} (w); 1531 $\nu_{asC=N}$ (s); 1600, 1468 and 1437 $\nu_{asC=C}$ (s); 1210 ν_{C-H} (w); 1067 ν_{as}c (w); 881 δ_{C-H} (s). UV-vis. (CH_3CN, Max nm): 408 (720 mol^{-1}·L·cm^{-1}), 244 (28200 mol^{-1}·L·cm^{-1}).

2.6. DNA interaction studies

All measurements with *calf-thymus deoxyribonucleic acid* (CT-DNA) were taken in a PBS buffer (NaCl 0.137 mol; KCl 2.68·10^{-3} mol; KH_2PO_4 1.47·10^{-3} mol;

Na_2HPO_4 0.016 mol; *p*H 7.6). The CT-DNA concentration per nucleotide was determined by absorption spectrophotometric analysis using a molar absorption coefficient of 6600 mol^{-1} L cm^{-1} at 260 nm [43]. The spectroscopic titrations were carried out by adding increasing amounts of CT-DNA to a solution of the complex in a quartz cell and recording the UV–vis spectrum after each addition. The binding affinities (K_b) were obtained by using the Benesi-Hildebrand equation: [DNA]/($_a$- $_f$) = [DNA]/($_b$- $_f$) + 1/[K_b($_b$- $_f$)] [44], where $_a$ is the apparent molar absorptivity, which corresponds to the ratio between an absorption of the measurement and a concentration of the complex ($A_{observed}$ [complex]); $_f$ is molar absorptivity of the free complex (without addition of DNA); $_b$ is molar absorptivity of the DNA-bound complex; K_b is the binding constant. Plotting a graph of [DNA]/($_a$ - $_f$) *versus* [DNA] gives the ratio of the angular and linear coefficients of intrinsic binding (K_b) between the complex and DNA.

Ru-complex/CT-DNA solution viscosities at different concentration ratios were measured using a Lovis 2000 M/ME Rolling-Ball Viscometer maintained at 25 °C in a constant temperature bath. Aqueous solutions of CT-DNA were studied by viscosity measurements at ambient pressure. The DNA concentration was fixed at 20 mol L^{-1}, and flow time was measured with a digital stopwatch. The mean values of three measurements were used to evaluate the viscosity of the samples. Specific viscosity was plotted as a function of DNA and Ru-complex concentrations. The values for relative specific viscosity (/ $_0$)$^{1/3}$, where $_0$ and are the specific viscosity contributions of DNA in the absence ($_0$) and in the presence of the complex ( ), were plotted against [complex]/[DNA] [45].

Circular dichroism spectra were measured on a Jasco J-810 spectropolarimeter equipped with a Peltier temperature control unit held at 25°C (Jasco Corp. Tokyo, Japan). CT-DNA and Ru-complexes were measured alone or at different mixture concentrations in PBS (*p*H 7.6) in a 1 mm path length quartz cell between 220 and 340 nm at a scanning speed of 100 nm min^{-1} and by the averaging of 10 scans. The absence of CD signal for Ru-complexes (200 μmol L^{-1}) was verified. Modification of the mixture signal was monitored after addition of Ru-complexes solutions to a fixed concentration of CT-DNA solution in two ratios [DNA] [Ru-Complex] 1:1 and 1:2.

Interaction of Ru-complexes with DNA was studied by ethidium bromide (EtBr) competition assays. All measurements were performed on a Varian Cary Eclipse Fluorescence Spectrophotometer using a 1 cm pathlength cuvette. These competition

experiments were carried out in PBS (pH 7.6), by keeping the molar ratio of DNA (nucleotide) to EtBr (5:1) constant and varying the Ru-complex concentrations (0-420 μmol L^{-1}). The excitation wavelength was 530 nm, and the emission range was set between 550 and 700 nm for all bromide fluorescence measurements.

2.7. BSA interaction studies

Circular dichroism spectra of *bovine serum albumin* (BSA) were recorded using a Jasco J-720 Spectropolarimeter at 25°C The measurements in presence and absence of the complexes were made in the range of 203–260 nm using a 0.1 cm cell with ten scans averaged for each CD spectra. The BSA concentration was maintained at 2.5 mol L^{-1}, and the molar ratio of complexes to BSA concentration was 1:2, 1:1 and 10:1. The thermal denaturation experiments were performed over 15–95°C, with intensity measurements taken at 208 and 222 nm, every 5 C°. Melting temperatures were calculated with sigmoidal fit employing the software Origin (Microcal).

2.8. Cell culture and Cytotoxicity assays

In vitro cytotoxicity assays on cultured human tumor cell lines still represent the standard method for initial screening of antitumor agents. The complexes were assayed against human cell lines: cervical carcinoma HeLa (ATCC® CCL-2™), the complexes **1** and **2** were assayed against human laryngeal carcinoma HEp-2 (ATCC CCL-23) and the complex **1** against the murine melanoma B16F10 (ATCC® CCL-6475™) and Vero Cell (ATCC CCL-81) derived from the kidney of an African green monkey. The cells were routinely maintained with Iscove's Modified Dulbecco's medium, supplemented with 10% fetal bovine serum (FBS), at 37 °C in a humidified 5% CO_2 atm. For the cytotoxicity assay, 5 x 10^5 cells mL^{-1} were seeded in 200 L of complete medium in 96-well plates. Stock solutions were prepared by dissolving the complexes in dimethyl sulfoxide (DMSO) followed by dilution with PBS, and serial dilutions of these stock solutions were made using culture media. In this way the lowest possible DMSO concentration was used in these experiments. The cells were exposed to the complex in different concentrations for a 24 and 48 h period. However, it was necessary to deviate from the standard MTT test protocol because of the sensitivity of **1** to **4** to ligand displacement by DMSO (see below). In this modified protocol, the stock solutions were prepared by dissolving the complexes in PBS buffer. The viability of cultured cells for these protocols described above was evaluated using MTT (3-(4,5-dimethylthiazol-2-

yl)-2,5-diphenyltetrazolium bromide) assays [46]. In this method, the MTT conversion to formazan by metabolically viable cells was monitored by SpectraMax 190 Microplate Reader (Molecular Devices) at 540 nm. Cell survival rate (%) *versus* drug concentration (logarithmic scale) was plotted to determine the IC_{50} (drug concentration at which 50% of the cells are viable relative to the control), with its estimated error derived from the average of 3 trials.

3. Results and discussion

3.1. Synthesis and characterization of Ruthenium(II)-arene complex

The synthesis of the series of [(η^6-*p*-cymene)$RuCl_2L$] complexes (Scheme 1) was achieved via bridge cleavage of [{(*p*-cymene)Ru(μ-Cl)Cl}$_2$] with a 5:1 ratio of ligands L (**apy**, **meapy** and **bzapy**) in toluene at RT for **1** - **3**. Complex **4** required a 2.3:1 mole ratio of **py** in toluene at reflux to achieve complete reaction. The complexes were prepared as orange solids, stable to light and in air, with yields ranging from 63-88%. In addition, all the complexes are soluble in water, halogenated solvents and polar organic solvents such as DMSO, dichloromethane and acetonitrile, but insoluble in diethyl ether (see Figures S11 - S14). The molar conductance of CH_3CN solutions of **1** – **4** were measured ($1.00 \cdot 10^{-3}$ M) after mixing and after 24 h to determine if solvolysis was a factor for the voltammetric and electronic spectroscopic experiments. The results are convincingly attributable to non-electrolyte solutions with no change after 24 h within experimental error (Table 1) [36]. In addition, conductivity measurements on aqueous solutions of **2** were performed ($1.00 \cdot 10^{-3}$ M) to confirm the labilization of the chloride ligand and the results suggest that partial hydrolysis occurs rapidly.

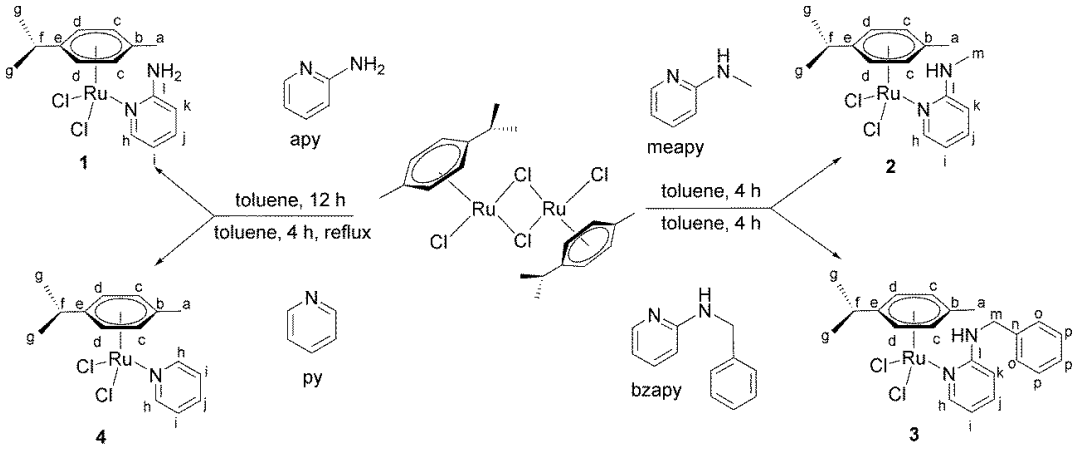

Scheme 1 Synthesis and structures of complexes **1-4**.

Table 1 Molar conductance data for the series of complexes [(^{6} *p*-cymene)$RuCl_2L$]

Complex	Λ_m CH_3CN ($\Omega^{-1}cm^{-1}$) **0 h** [a]	Λ_m CH_3CN ($\Omega^{-1}cm^{-1}$) **24 h** [a]	Λ_m H_2O ($\Omega^{-1}cm^{-1}$) [b]
1	33.4	35.5	___
2	33.3	35.1	69.8
3	31.4	32.6	___
4	35.6	36.8	___

[a] CH_3CN 1 10^{-3} mol L^{-1}. [b] H_2O 1 10^{-3} mol L^{-1}.

3.2. Molecular structures by X-ray crystallography and DFT computation

Single-crystal structures on **1** and **4** have previously been reported were deposited in the Cambridge Structural Database, version 5.38, Nov 2016 (CSD) [47] under CSD refcodes: JOBCOS [39] for **1** and MIXSOD [41] and MIXSOD01 [13] for **4**, respectively. For complex **3**, a structure of a closely related complex exists in which **bzapy** is coordinated in [(^{6}-ethylbenzoate)$RuCl_2L$] (**3b**), CSD refcode: OHICAL [48]. In this work, we report the new crystal structure of the 2-methylaminopyridine complex **2** (see Table S1, Figure S1 in the *Supplementary Information* (SI) for structure details). The derived interatomic parameters of these four structures in their crystalline lattices are compared to those from UB3LYP//6-31+G(d), SPK-DZCD hybrid DFT calculations (Table S2, Figure S2) on **2** and more extensively on **1** as a representative electronic model system. The crystal structure of **2** displayed considerable complexity, containing $CHCl_3$ solvent of crystallization, two independent molecules in the asymmetric unit and a wholesale disorder of the **meapy** ligands (only the major components of the disorder are shown in Figure 1). In each case, there are hydrogen bonds from the ligand N–H to metal-bound chloride ligands. Note that in the Ru1 molecule for the major (75% refined occupancy) component, the CH_3NH group (N2) is oriented towards the end of the cymene ligand bearing the isopropyl group (Cl1), whereas in the Ru2 molecule in the major (63% refined occupancy) component, the equivalent group (N4) is oriented towards the methyl group side of the cymene ligand (Cl3). The minor components of each disordered pair have the **meapy** groups flipped towards the opposite ends of the respective cymene ligands. The same disorder was observed for crystals grown solvent-free from diethyl ether and chlorobenzene; apparently the molecular volume of **meapy** and *para*-cymene are extremely similar.

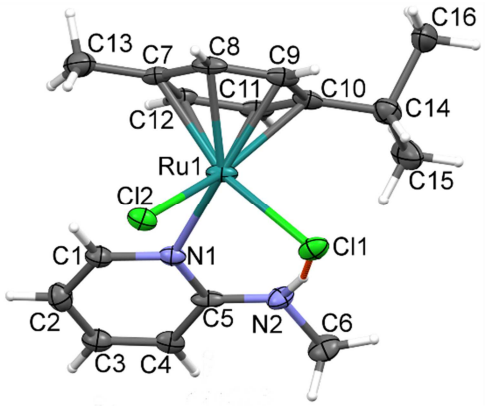

Fig. 1 Displacement ellipsoids (50% probability) plot of one of two similar independent molecular structures of **2** as found in the crystal lattice, with the atom numbering scheme. Only the major components of the **meapy** disorder models are shown. The H-bond geometry is indicated by a dashed orange line (see Table 1)

All four molecules adopt very similar molecular structures to that of **2** in their crystal lattices (see Fig. S1 in the Supporting Information). Key features are the classic "piano-stool" architecture wherein the ^{6}-arene groups fill three facial sites in the *pseudo*-octahedral geometry at ruthenium. In each case, including **4**, the coordinated pyridine ring is oriented approximately parallel to that of the ^{6}-arene albeit angled downwards by ~30°. Consideration of space filling models (Figure S3) indicates that this conformation represents a rotational minimum due to constraints between the ortho hydrogen atoms in pyridine with Cl1,2. This conformational preference is augmented by N2H2 Cl1 hydrogen bonding in **1** – **3b**, which is retained in gas-phase DFT calculated structures. Notably, the pyridyl ligands are all ^{1} coordinated through N1 in these [(^{6}-*p*-cymene)RuCl$_2$L] complexes, whereas the ^{2}-*N,N'*-chelating geometry is known in (2-aminopyridine)-dichloro-bis(triphenylphosphine)-ruthenium(II), CSD refcode: IHIWAX (Figure S4) [49]. Thus, despite the 2-NHR substitution in **1**–**3**, all complexes are confirmed to be of type A (see the Introduction). Interestingly, a recent paper reports on several [(^{6}-*p*-cymene)RuCl$_2$(2-halogenated-5-aminopyridines)] with unexpected coordination from the *amino* group rather than the more basic ring N [50].

3.3. Solid state structural features from FT-IR and Raman spectra

The FT-IR spectra (Figure S5 and Table S3) contain the expected bands for the pyridine ligands in addition to those of the ^{6}-*p*-cymene and chloride ligands but have low diagnostic information save for the $_{as(N-H)}$ bands in **1**–**3** (and their absence in **4**). The observed stretching frequencies follow the inter- and intramolecular N Cl

hydrogen bonding distances from respective crystal structures of 3.234 ($\nu_{1(N-H)}$ = 3390 cm^{-1}) and 3.243 Å ($\nu_{2(N-H)}$ = 3372 cm^{-1}) in **1**, and with intramolecular distances 3.165 Å in **2** ($\nu_{(N-H)}$ = 3259 cm^{-1}) and for **3** 3.147 Å in OHICAL ($\nu_{(N-H)}$ = 3238 cm^{-1}). The correlation of N-H···Cl distances with N-H stretching frequencies is long known from the literature [51]. The Raman spectra (Figure S6, Table S4) corroborate the FT-IR results.

3.4. Solution structures as established by NMR

A full assignment of the solution-phase ^{1}H and ^{13}C NMR signals was achieved on the basis of 1D (NMR) and 2D experiments (Table S5 and Scheme S1, along with full archival spectra in Figures S7-9). These data, especially the ^{1}H spectra, provide convincing information about the solution structures and the purities of **1**–**4**, showing that (i) the *p*-cymene ring is rotationally fluxional, rendering an effective C_{2v} symmetry despite coordination to the ruthenium and (ii) the **apy**, **meapy** and **bzapy** ligands retain similar geometries in solution in $CDCl_3$ as deduced from the solid-state structures (see above). Thus, whilst the NH_2 signal in **1** integrates to 2H, it has a chemical shift (δ = 6.16) intermediate between that of hydrogen-bonded and non-hydrogen-bonded NH. By contrast, the single NH proton signals of **2** (δ = 7.28) and **3** (δ = 8.10) are deshielded. This data is consistent with the intermolecular H-bonding strengths **3** > **2** > **1** also shown by crystallographic *d*(N···Cl) data and the trend of the $\nu_{as(N-H)}$ bands in the FTIR spectra. The other ^{1}H chemical shifts correlate well with the expected substituent effects from the presence of the 2-amino groups on pyridine in **1** – **3** and its absence in **4**. The δ and the Δδ values for *p*-cymene ring protons $H_{2,3}$ are remarkably invariant for the series and quite similar to those in the chloride-bridged precursor complex (*pseudo*-AB doublets at 5.37 and 5.51 ppm, and $^{3}J_{HH}$ = 6.04 Hz). The observation of $^{3}J(H^{n},H^{m})$ = 5.0 and 5.5 Hz in spectra of **2** and **3** in $CHCl_3$ solution indicates lack of exchange of the NH signals. This is also consistent with a dominant H-bonded conformation in solution. This coupling is confirmed by gCOSY experiments (see Figure S9 in the SI).

3.5. Electronic structure from DFT calculations on 1 as a model system

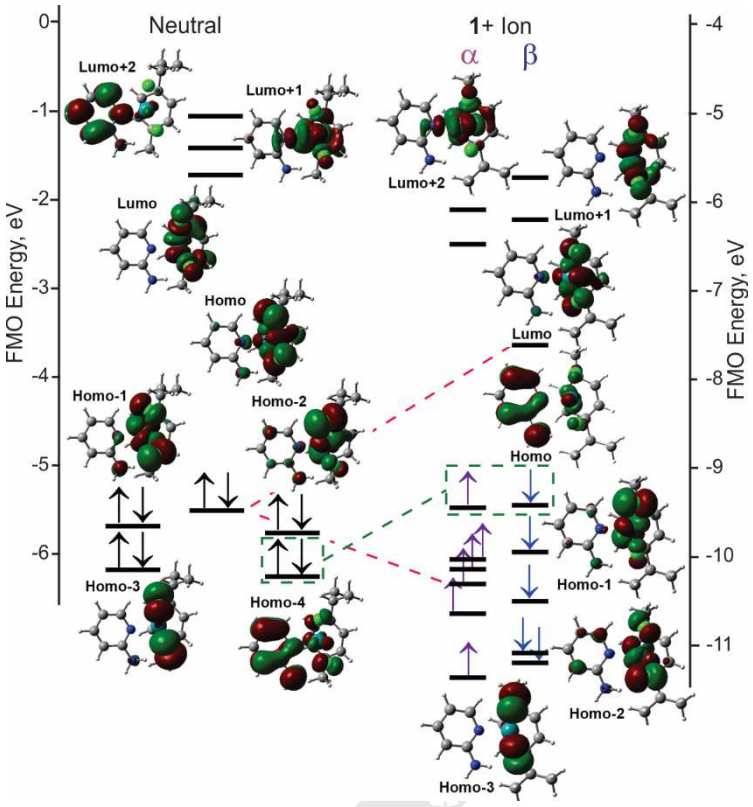

Fig. 2 Frontier molecular orbitals (FMO) and energy levels from gas phase DFT calculations on complex **1** (singlet state, left) and $\mathbf{1}^{+}$ (doublet state, right; for clarity only the -spin orbitals in $\mathbf{1}^{+}$ are shown). The energy scale at right is displaced upwards by about 4 eV.

The electronic structure of complex **1** was examined in detail using hybrid DFT calculations at the UB3LYP//6-31+G(d),SPK-DZCD level of theory. The neutral molecule was geometry optimized both in the gas phase and in an aqueous solvent model. In addition, the oxidation states −2, −1, +1 and +2 were all optimized (see Figure S10 in the SI). The need for computation was indicated to assist with assignment of the electronic absorption spectra and particularly the rather odd voltammetric behavior of the complexes (see below). All complexes optimized to a reasonable geometry with the strongest bonding between the *p*-cymene and metal in the neutral (18*e*) state, as expected (*p*-cymene ring centroid to Ru distance of 1.766 Å). Both oxidized and reduced forms have weaker bonding and the anions optimize with one chloride ligand migrating from Ru to sites that only hydrogen-bond to the NH group. In the 20*e* dianion, the arene converts to ^{4}–coordination, fully consistent with classical organometallic bonding models. All charge states display NH Cl H-bonding, either to

coordinated or displaced halides (see Fig. S10). The following discussion deals specifically with neutral **1** in the gas-phase model.

The calculated electronic structure presented in Figure 2 (left) indicates that the highest occupied orbitals (HOMO, HOMO-1, HOMO-2, corresponding closely to the t_{2g} set of the *pseudo*-octahedral geometry) have mixed Ru 3*d* orbitals and Cl 2*p*-π* character along with minor participation from C 2*p* orbitals of the *p*-cymene ring. These three frontier molecular orbitals (FMO) are almost degenerate and lying only slightly lower in energy are two (accidentally) degenerate levels: HOMO-3, with mostly non-interacting Cl p_z character, and HOMO-4, the essentially unperturbed aminopyridine filled π3 level. In turn, the two lowest unoccupied orbitals (LUMO and LUMO+1, corresponding to the e_g set) have both Ru 3*d* and significant Ru-Cl σ* character. Above these, LUMO+2 is an almost unperturbed pyridine π4 MO [52].

3.6. Electrochemical characterization in solution by voltammetry

The redox behavior of **1** – **4** was investigated by cyclic voltammetry (CV). The CVs of **1** – **4**, recorded at a glassy carbon electrode in 0.1 M TBAP/CH_3CN solutions as the supporting electrolyte (*vs*. Ag/AgCl), are shown in Figure 3 and the pertinent data are presented in Table 2 (see also Figures S11–S16 in the SI). Most importantly, and the goal of the voltammetric study undertaken for this project, is the evidence for a very wide redox stability window (E_{window} = 2.2 V), defined by the difference between E_{pa}^{I} and E_{pc}^{IV}, extending far out in both the anodic and cathodic regions. This provides direct evidence for the oft-claimed stabilization of the Ru(II) oxidation state by η^6-arene ligands [9]. This stability is only marginally affected, compared to **py** in **4**, by amino-substitution in **1** – **3**. Importantly, this range is much wider than the physiological E^o range, between ~−1V and +1V *vs*. SHE, so this class of complex can be expected to remain as Ru(II) in vivo so long as the arene ligand remains attached [53].

The detailed CV behaviour of **2**, representative of the 2-aminpyridine complexes, was studied first in the anodic region at a scan rate of 100 $mV{\cdot}s^{-1}$, whereby it exhibits two very closely-spaced chemically irreversible processes at around 1.15 and 1.23 V, designated I and II, respectively, followed by process III at E_{pa} 1.37 V, for which a small return wave can be detected. These processes could *in principle* correspond to a possible sequence of one-electron oxidations $[(\eta^6\text{-}p\text{-cymene})RuCl_2(\textbf{meapy})]^{0/+/2+/3+}$, but such closely spaced waves would be quite unusual for an isolated metal complex due to the effects of charge buildup.

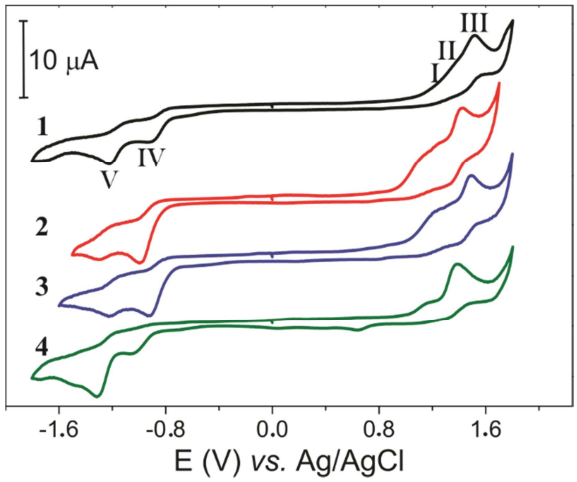

Fig. 3 Cyclic voltammograms of **1** – **4** at 2.0 10^{-3} mol L^{-1} in TBAP/ACN 0.1 mol L^{-1} *vs.* Ag/AgCl; obtained at 100 mV s^{-1}.

Further insight into these oxidation processes is provided by the computed electronic structure of the 1+ state. After removal of the first electron from a Ru(*d*)-Cl(*p*-) orbital (the HOMO at left in Figure 2), significant orbital re-organization occurs. The result is that the HOMO of the doublet state ion derives from the filled aminopyridine ligand 3 level (which is HOMO-4 of the neutral state.) The unpaired electron retains Ru(*d*) character at lower energy (it is the spin orbital that has a very similar topology to the LUMO shown on the diagram; *the energy evolution is shown in dashed red lines on Figure 2*). Because the aminopyridine orbitals are non-interacting with the metal, they do not experience the same amount of energy-lowering in the cationic state as the metal orbitals do. This suggests the possibility that second (and third) electrons in oxidation processes II (and III) come from the ligand and the metal remains Ru(III) in all these oxidized states. In short, aminopyridine ligands appear to function as redox-non-innocent ligands *in the oxidized cationic states* [54].

Table 2 Potential data for complexes **1** – **4**.

Complex	E_{pa}^{I} /V	E_{pa}^{II} /V	E_{pa}^{III} /V	E_{pc}^{III} /V	E_{m}^{III} /V	ΔE_{p}^{III} /V[b]	I_{pc}/I_{pa}^{III}[c]	E_{pc}^{IV} /V	E_{pc}^{V} /V	E_{window} /V[d]
1	1.37	1.41	1.52	1.43	1.47	0.09	0.11	-0.91	-1.22	2.28
2	1.15	1.23	1.42	1.33	1.37	0.09	0.20	-0.98	-1.30	2.13
3	1.22	1.32	1.49	1.40	1.44	0.09	0.15	-0.92	-1.22	2.14
4	1.16		1.39	1.33	1.36	0.06	0.04	-1.04	-1.32	2.20

[a] $E_{1/2} = (E_{pa} + E_{pc})/2$; [b] Measured by difference between E_{pa} and E_{pc}; [c] Evaluated as by ref [55] (to 2 V·s^{-1}); [d] Measured by difference between E_{pa}^{I} and E_{pc}^{IV}.

In the cathodic region, two irreversible reduction peaks are observed (processes IV and V, E_{pc}^{IV} at -0.98 and E_{pc}^{V} at -1.30 V, respectively). These processes can be confidently attributed to sequential occupation of the LUMO of the neutral complex (Figure 2). Although formally this involves Ru^{II}/Ru^{I} reduction, this orbital also has significant Ru-Cl σ* character. In this regard, it is interesting to observe that DFT calculations optimize to geometries where one of the Cl^{-} ions leaves the metal and attaches remotely to the NH moiety via H-bonding (see Figure S10 in the SI). Ligand dissociation could thus be responsible for the (chemical) irreversibility of these processes.

The CVs of all four complexes were also recorded upon scanning from +1.0 to +1.9 V and from -0.6 to -1.7 V over ν = 50 – 2000 mV·s^{-1} (see Figures S13-S16 in the SI). In all cases, the linearity of I_p *vs.* $\nu^{1/2}$ plots demonstrates that mass transport of these compounds to the electrode surface is diffusion-controlled. The voltammetric features (I_{pa}/I_{pc} less than unity and ΔE_{peak} values about 90 mV) show that oxidation-reduction of these compounds is chemically and electrochemically almost reversible in fast scans and irreversible at lower scan rates.

3.7. Electronic absorption spectroscopy

Electronic absorption spectra of complexes **1** – **4** were acquired in the concentration 10^{-4} mol·L^{-1}, in different solvents at RT, such as: acetonitrile, water and PBS buffer (Figure 4). The spectra in all these solvents showed similar broad low-energy bands with maxima at 389-416 nm (ε = 2100-800 L·mol^{-1}·cm^{-1}), which can be attributed to LUMO←HOMO transitions. TD-DFT calculations, carried out in CH_3CN and water solvent models, indicate that several transitions involving the cluster of

highest filled orbitals probably contribute to these bands which thus have significant *d* *d* character (albeit with covalent contributions from Cl and pyridine N orbitals).

In addition, there are two sets of higher-energy bands. The first, with maxima close to 300 nm for **1** – **3**, are noticeably absent in the spectra of **4**. These bands may involve excitation from HOMO-4 to the LUMOs or from the higher filled orbitals to LUMO+2. Probably the 2-aminopyridine orbitals are involved and are thus either LMCT or MLCT bands of modest intensity. Very intense bands at ~250 nm could include lower-lying metal electron excitation to high virtual orbitals; furthermore, *p*-cymene and pyridine * transitions. The TD-DFT calculations indicate that most bands have multiple transition contributions with varying oscillator strengths.

A noticeable feature (see the insets in Figure 4) is that the LUMO HOMO bands are blue-shifted by 12–26 nm in the aqueous spectra. There is a strong expectation that these complexes will undergo hydrolysis either partly or completely in water (Scheme 2) [18,56-58]. Our conductivity data (Section 3.2) suggest that the hydrolysis is relatively slow and thus likely to stop at a single halide replacement. Replacement of one chloride ligand by water is consistent with lowering the highest occupied FMOs due to weaker * character, and thus with a blue-shift. Since the hydrolyzed complexes will tend to be cationic (especially in the enhanced acidic environment of cancer cells), these processes have important implications for the *in vitro* biological test results (see below).

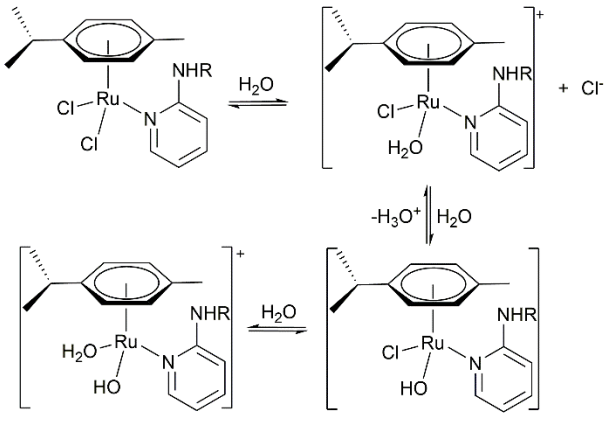

Scheme 2 Some of the equilibria connected to chloride hydrolysis in aqueous phases.

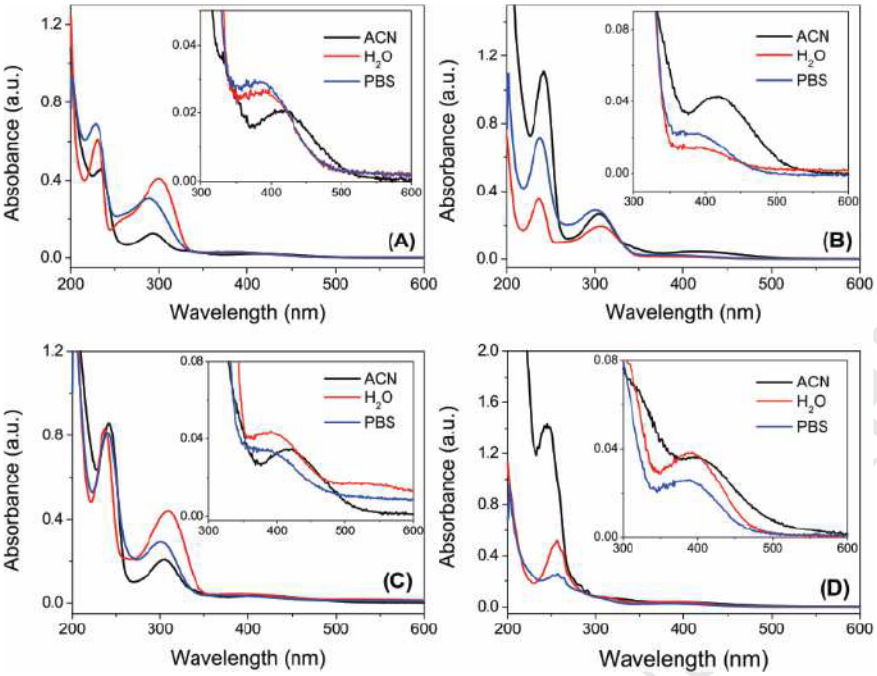

Fig. 4 UV-vis spectra of the series of complexes [(η^6-*p*-cymene)$RuCl_2L$] in acetonitrile, water and PBS buffer. In each case, the main window covers 200-600 nm, with an expanded inset from 300-600 nm. (A) Complex **1**. (B) Complex **2**. (C) Complex **3**. (D) Complex **4**. Tabulated data provided in Table S4.

3.8. DNA interaction studies

Among organometallic ruthenium complexes, a range of compounds exhibit potent anticancer activity. Many cytotoxic agents were proven to have DNA as the cellular target. These molecules elicit a range of cellular responses which implies different mechanisms of action [5,7]. The interaction of drug molecules with DNA can be categorized using simple limiting models as shown schematically in Figure 5 as non-covalent (intercalation, groove binding, electrostatic attraction) or covalent (condensation or hydrogen-bonding with nitrogen bases or condensation with phosphate of the DNA backbone).

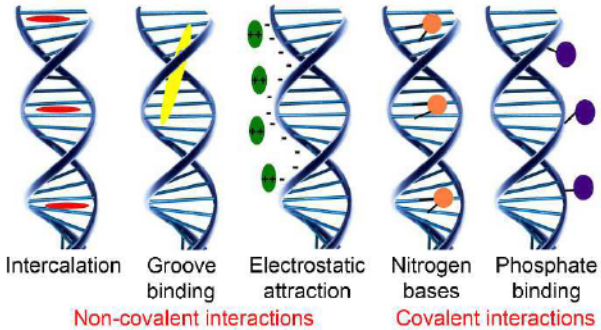

Fig. 5 Cartoons showing common modes of interaction between drug molecules and double-stranded DNA. Adapted from *Rev. Virtual Quim.*, **2015**, *7* (6), 1998-2016, with the permission of the Brazilian Chemical Society.

3.8.1. UV–vis spectroscopy

UV–vis absorption measurements have been successfully used to study the mode and magnitude of interaction of complexes **1** – **4** with CT-DNA. DNA–complex interactions are evidenced by this technique through changes in absorbance intensity and position of the absorption band. When complexes **1** – **4** were titrated with CT-DNA, hyperchromism (i.e. increased intensity) was observed, along with a small red-shift of 2-4 nm in the presence of complexes **2** and **3** (Figure 6). The binding strengths of **1** – **4** were quantified from the values of intrinsic binding constant K_b, determined using the Benesi-Hildebrand equation (Table 3) [43]. Whereas hypochromism (i.e. decreased intensity) is indicative of DNA intercalation (due to contraction of the helix and conformational changes caused by changes in the - stacking interactions), [59] hyperchromism is attributed to electrostatic interaction between complexes and the negatively charged phosphate backbone at the periphery of the double helix CT-DNA or to secondary damage of the DNA double helix structure [60-63]. The presence of complexes **1** to **4** resulted in hyperchromism in DNA absorption spectra suggesting non-intercalative binding between DNA and the complexes. This is corroborated by the size of the intrinsic binding constants K_b being in the micromolar range [64].

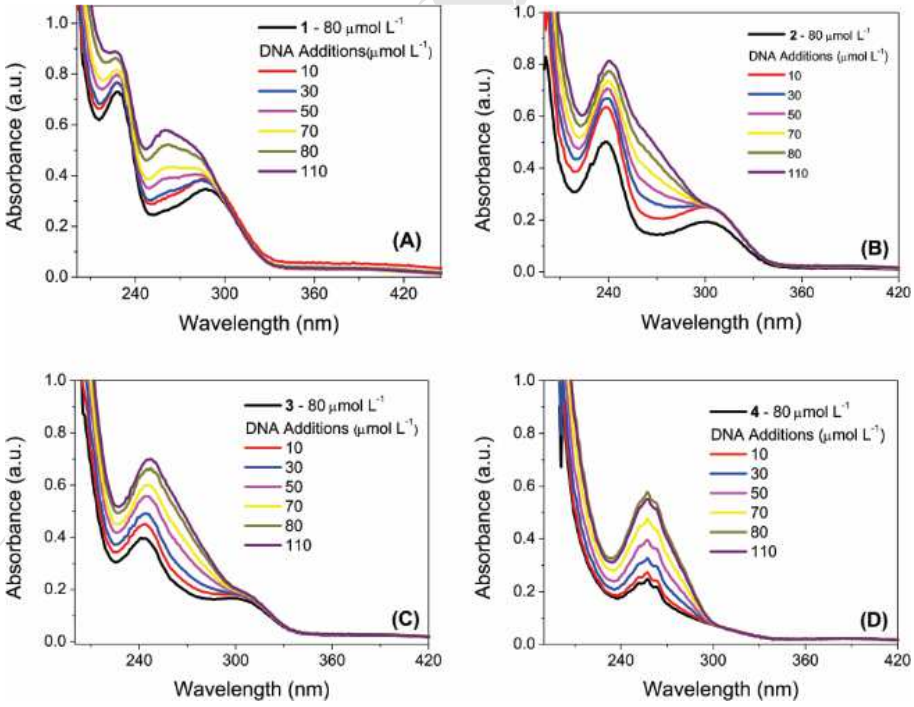

Fig. 6 Electronic spectra of the complexes in the absence and after successive additions of CT-DNA. (A) complex **1**; (B) complex **2**; (C) complex **3**; (D) complex **4**.

Table 3 Intrinsic binding constants (K_b) for interaction between CT-DNA and complexes **1** – **4.**

Complexes	**Wavelength** (nm)	K_b (M^{-1})
1	227	2.24×10^5
2	237	1.40×10^5
3	243	7.34×10^4
4	257	3.68×10^4

3.8.2. Circular dichroism spectroscopy

The circular dichroism (CD) technique is responsive to changes in the chiral structure of DNA and is used to study variations in DNA conformation upon its interaction with small molecules [65]. B-form calf thymus DNA exhibits a negative band at 245 nm caused by helicity and a positive band with maximum at 275 nm caused by base stacking [66,67].

Distinct modes of interaction can be distinguished by changes in the spectra. Intercalation clearly enhances the signal intensity of both the base stacking and helicity bands, while groove binding and electrostatic interactions cause slight perturbations on positive and negative bands. In addition, changes just in the intensity, and not shape, of the observed CD results suggest a single binding mode. Changes in the shape of CD signals may indicate multiple ligand-DNA binding modes, changes in DNA conformation or ligand–ligand interactions [68].

To verify whether binding of the complex causes any conformational change of the DNA double helix, CD spectra of CT-DNA were recorded at different complex/CT-DNA ratios (Figure 7, black lines). The addition of complexes **1**, **2** and **4** to CT-DNA slightly increased the intensity of the positive peak and decreased the intensity of the negative peak (Figure 7). These changes in the CD spectra in the presence of the complexes indicate that complexes **1**, **2** and **4** interact with CT-DNA and stabilize the right-handed B-form of CT-DNA structure. These alterations in spectra are common in groove binding and electrostatic interactions [65].

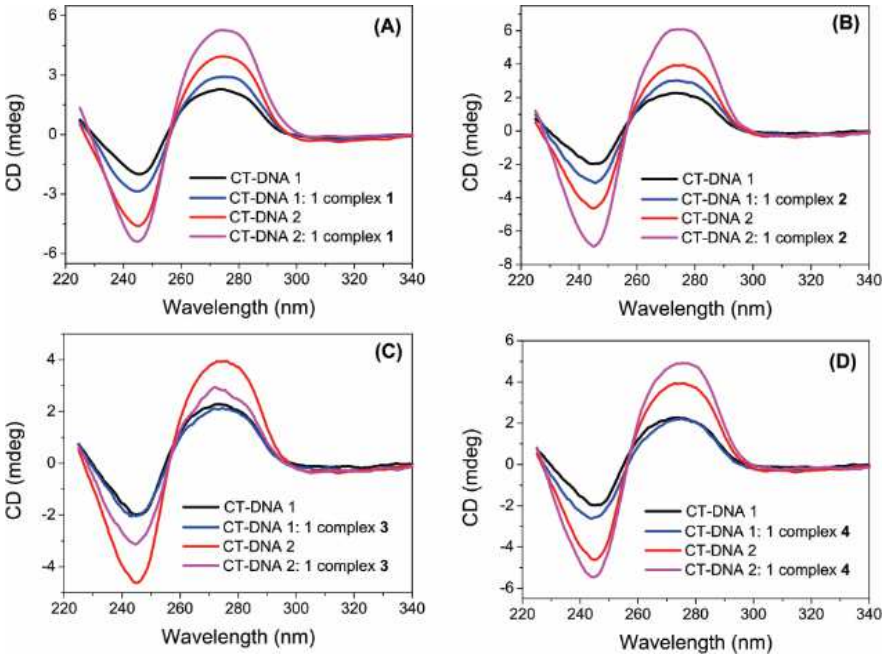

Fig. 7 CD spectra for CT-DNA (100 and 200 mol L^{-1}) in PBS buffer (pH 7.6), with addition of 200 mol L^{-1} of the complexes. (A) complex **1**; (B) complex **2**; (C) complex **3** and (D) complex **4**.

3.8.3. Ethidium bromide competition.

To confirm a non-intercalative binding mode, competition experiments with EtBr were performed. Classical intercalators displace EtBr from DNA bases, thereby decreasing its fluorescence emission [69]. Addition of complexes **1** – **4** to EtBr-DNA solutions does not alter emission intensity of EtBr by more than the dilution effect, which, together with the spectroscopic titration and CD results, indicates that these complexes are not DNA intercalators.

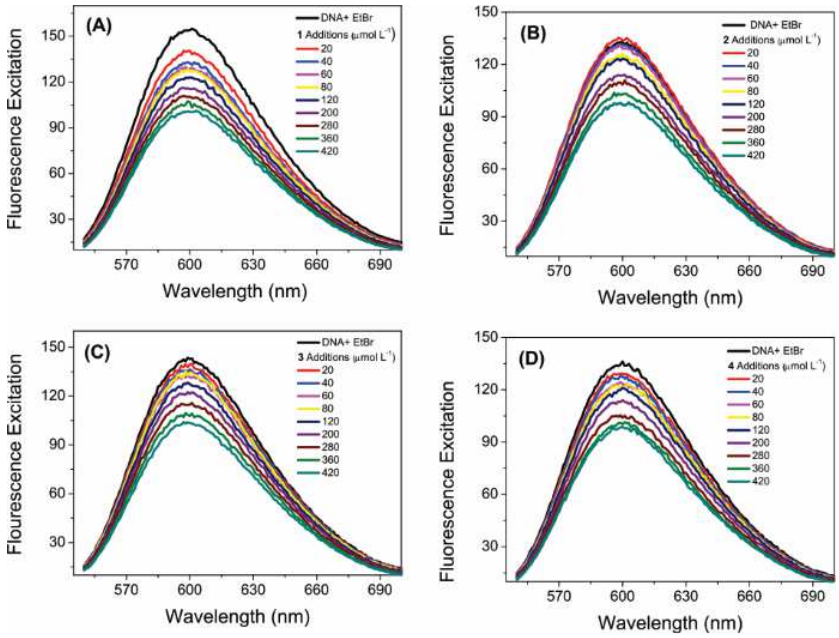

Fig. 8 Emission spectra of the EtBr/CT-DNA system, with successive additions of the complexes: (A) complex **1**; (B) complex **2**; (C) complex **3** and (D) complex **4**. Confirmed dilution effect after successive additions to PBS buffer.

3.8.4. Viscosity Measurements

Hydrodynamic measurements are considered as unequivocal tests of DNA binding models in solution, clarifying the interaction mode of a compound with the nucleic acid. An interaction between the DNA double helix and a small molecule may cause length changes in DNA and as a result viscosity changes [44]. The values of relative specific viscosity $(/ _0)^{1/3}$ were plotted against [DNA]/[complex] (Figure 9). In this study, it was observed that increasing concentrations of complexes **1** – **4** do not significantly alter the DNA viscosity. Thus, it is possible to infer that these complexes are not covalent binders, and neither partial nor classical DNA intercalators.

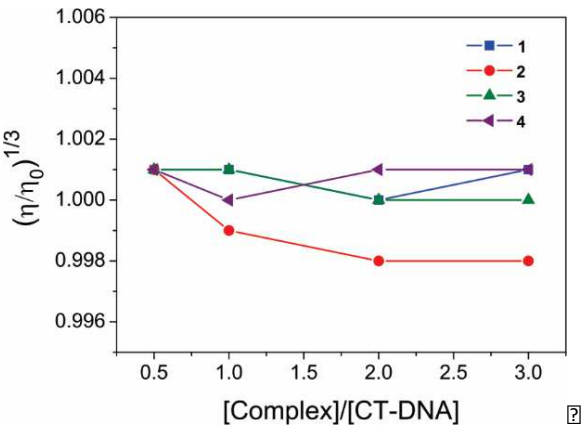

Fig. 9 Viscosity graph plotting the increase of the concentration of the complexes *vs*. the relative viscosity of the CT-DNA (20 mol L^{-1}) at 25 °C.

3.9. Cytotoxicity assays

The cytotoxic effects were examined for the [(^{6}-*p*-cymene)$RuCl_2$L] series complexes as well as for the ([(^{6}–*p*-cymene)$RuCl_2$(DMSO)] obtained *in situ*, since ^{1}H NMR (see Figure S18) tests performed for the complexes in the presence of DMSO demonstrate that there is a pyridine ligand lability with coordination by the DMSO molecule. The complexes thus formed by replacing monodentate pyridine ligands with DMSO were confirmed to also be neutral by conductivity tests (see Table S7). Coordination of DMSO in ruthenium pyridine complexes has been previously reported in the literature [18,70] and by comparison of data we can indicate that the DMSO is coordinated to the metal through sulfur [71,72].

The cytotoxic tests for [(^{6}-*p*-cymene)$RuCl_2$L] complexes in DMSO were carried out against HeLa, Hep-2, B16F10 and Vero cells line (Table 4, Figure S19), while tests carried in phosphate buffer were evaluated only against Hep-2 and B16F10 (Table 4, Figure S20). Emphasis was placed on testing against the resistive HeLa line. The results obtained using an MTT assay showed that only **2** with DMSO achieved an IC_{50} against the HeLa tumor line after a 24 h with IC_{50} = 346 mol L^{-1}. The *absence* of toxicity in aqueous solution suggests that the toxicity is due to the liberated **meapy** ligand. For the other complexes of the series with or without DMSO as well as for other tumor lines, HEp-2 and B16F10, it was not possible to determine IC_{50} values in the range of concentrations investigated.

Table 4 Cytotoxicity results for 1–4 on HeLa, HEp-2, B16F10 and Vero cell lines, after 24 h incubation performed in DMSO solution or in aqueous buffer.

Complex	IC_{50} (mol L^{-1})			
	HeLa	HEp-2	B16F10	Vero
1 – DMSO [a]	>500	>500	>500	>500
2 – DMSO [a]	346±3	>500	—	—
3 – DMSO [a]	>500	—	—	—
4 – DMSO [a]	>500	—	—	—
1 [b]	—	>630	—	—
2 [b]	—	>600	>600	—
3 [b]	—	>600	—	—
4 [b]	—	>650	—	—

[a] From DMSO stock solution; displacement of L by DMSO-S is assumed. [b] Test performed using an aqueous buffer stock solution.

The low activity of [(^{6}-*p*-cymene)$RuCl_2$L] series **1** – **4** against cancer cell lines is similar to results reported on a range of other type A complexes with simple substituted pyridines [10,12,14,16,18,28,73,74]. By contrast, the substituted aminopyridines reported by Richter *et al.* [27], bearing 4-carboxylatophenyl substituents at the amine, were shown to be more active against 8500C, MCF-7, SW-480 and 518A2 cancer cell lines, although only marginally more than the direct use of the corresponding substituted amino-pyridines in control tests [75].

3.10. BSA Interactions

An important feature of biologically active compounds is their binding to proteins. The ability to interact with proteins affects the activity of a molecule in biological systems, so protein-binding studies are carried out to reveal the potential of new drug molecules. Bovine serum albumin protein is frequently used in these protein-binding studies because of its structural homology with human serum albumin (HSA). In order to characterize binding of complexes **1** – **4** to BSA, we carried out circular dichroism studies. The protein conformation was not significantly altered in the presence of complexes **1** – **4** (Figure S17 in the SI). We further investigated the thermal stability of BSA in the presence of complexes **1** – **4**. When bound to a protein, small molecules tend to enhance the thermal stability, resulting in increased melting temperatures (*Tm*) [76]. Thermal stability curves for BSA-complexes and BSA alone were plotted from 15 to 95ºC, as shown in Figure 10. The melting temperature (*Tm*) of BSA was estimated in 72.1ºC and in the presence of complexes **1** – **4**, temperature varied from 67.2 to 75.4ºC, which indicates no significant increase in BSA stability. The addition of complexes **1** – **4** did not increase the melting temperature (*Tm*) of

BSA. In sum, the CD spectra and thermal stability results indicate that there is no interaction between BSA and complexes **1** – **4**.

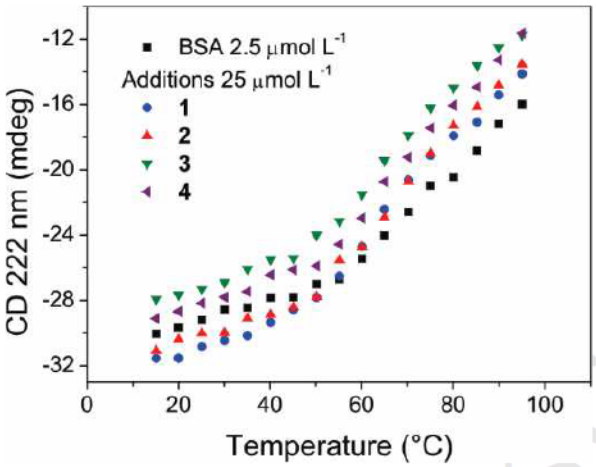

Fig. 10 CD spectra monitoring thermal denaturation of BSA in PBS buffer (pH 7.6) in the presence and absence of the [(η^6-*p*-cymene)$RuCl_2$(L)] series. Temperature range (15-90 °C).

4. Summary and conclusions

In line with virtually all type A complexes with pyridine or small-substituents pyridine derivatives [10], **1**, **3** and **4** show no cytotoxicity, while **2** (in DMSO) shows some activity, attributable most likely to just the **meapy**. Our DNA interaction tests provide evidence for interaction with DNA and lack of protein interactions with BSA. Of the possible modes of interaction (Figure 5), only non-covalent interactions need be considered for the measured interaction strengths. Intercalation can be ruled out definitively by EtBr fluorescence and the DNA solution viscosity measurements. Since these small molecules are not optimal for groove binding (which depends on strong dispersive interactions) the most likely interaction is electrostatic binding between the partly hydrolyzed mono-cationic forms of complexes **1** – **4**. Whereas it had been hoped that the benzyl group in **3** would be optimal for intercalation with DNA, apparently all these complexes pre-associate with the DNA backbone but do not proceed to intercalative or covalent linkage. Since our measurements show relatively slow rates of hydrolysis, the low activity of **1** – **4** may be due to lower than expected concentrations of active species in the conducted assays.

This study also provides valuable evidence for the high redox-stability of type-A [(η^6-*p*-cymene)$RuCl_2$L] complexes and provides the first detailed computational investigation of the electronic structures of this class of complex. These provide insights

into the unusual voltammetry of oxidation and the assignment of electronic absorption spectra, results which we hope will be generally useful for the further development of organometallic ruthenium-based cytotoxic agents. Finally, our work confirms the unsuitability of the standard MMT protocol for cytotoxicity testing using DMSO to prepare stock solutions for ^{1}-pyridyl type A complexes.

Acknowledgments

The authors thank the Brazilian agencies (CNPq PVE 401271/2014-5 and CAPES) for generous financial support through grants and scholarships. We acknowledge the Laboratory of Spectroscopy and Calorimetry at Brazilian Biosciences National Laboratory (LNBio), CNPEM, Campinas, Brazil for their support with the use of the spectropolarimeter and Prof. Christiane Philippini F. Borges from UEPG for providing access to the Fluorescence Spectrophotometer. We thank the University of Lethbridge for purchasing the SuperNova X-ray diffractometer and the anonymous referees for directing us to the literature regarding unsuitability of DMSO in the MMT protocols.

Notes and references

1. L. Zeng, P. Gupta, Y. Chen, E. Wang, L. Ji, H., Z. S. Chen, Chem. Soc. Rev. 46 (2017) 5771-5804.
2. U. Ndagi, N. Mhlongo, M. E. Soliman, Drug Des. Devel. Ther. 11 (2017) 599-616.
3. B. S. Murray, M. V. Babak, C. G. Hartinger, P. J. Dyson, Coord. Chem. Rev. 306 (2016) 86-114.
4. J. K. Liang, H. J. Zhong, G. Yang, K. Vellaisamy, D. L. Ma, C. H. Leung, J. Inorg. Biochem. 177 (2017) 276-286.
5. P. Zhang, P. J. Sadler, J. Organomet. Chem. 839 (2017) 5-14.
6. C. S. Allardyce, P. J. Dyson, Dalton Trans. 45 (2016) 3201-3209.
7. E. Alessio, Eur. J. Inorg. Chem. 2017 (2017) 1549-1560.
8. P. Jia, R. Ouyang, P. Cao, X. Tong, X. Zhou, T. Lei, S. Zhou, J. Coord. Chem. 70 (2017) 2175-2201.
9. B. Therrien, Coord. Chem. Rev. 253 (2009) 493-519.
10. We have identified about 20 complexes in this category for which cytotoxicity has been investigated by a SciFinder search of the Chemical Abstracts database. This information has been compiled in the Electronic Supporting Information (SI).
11. R. Sàez, J. Lorenzo, M. J. Prieto, M. Font-Bardia, T. Calvet, N. Omeñaca, V. Moreno, J. Inorg. Biochem. 136 (2014) 1-12.
12. J. Grau, V. Noe, C. Ciudad, M. J. Prieto, M. Font-Bardia, T. Calvet, V. Moreno, J. Inorg. Biochem. 109 (2012) 72-81.
13. M. V. Babak, D. Plazuk, S. M. Meier, H .J. Arabshahi, J. Reynisson, B. Rychlik, A. Blauz, K. Szulc, M. Hanif, S. Strobl, A. Roller, B. K. Keppler, C. G, Hartinger, Chem- Eur. J. 21 (2015) 5110-5117.
14. K. S. A. M. Shweshein, F. Andric, A. Radoicic, M. Zlatar, M. Gruden-Pavlovic, Z. Tesic, D. Milojkovic-Opsenica, Sci. World J. 2014 (2014) 1-10.
15. N. Gligorijevi , S. Aran elovi , L. Filipovi , K. Jakovljevi , R. Jankovi , S. Grguri -Šipka,, Ž. L. Teši , J. Inorg. Biochem. 108 (2012) 53-61.
16. S. Grguri -Šipka, I. Ivanovi , G. Raki , N. Todorovi , N. Gligorijevi , S. Radulovi , Ž. L. Teši , Eur. J. Med. Chem. 45 (2010) 1051-1058.
17. K. G. Liu, X. Q. Cai, X. C. Li, D. A. Qin, M. L. Hu, Inorganica Chim. Acta. 388 (2012) 78-83.
18. M. Patra, T. Joshi, V. Pierroz, K. Ingram, M. Kaiser, S. Ferrari, G. Gasser, Chem. Eur. J. 19 (2013) 14768-14772.
19. I. Ivanovi , S. Grguri -Šipka, N. Gligorijevi , S. Radulovi , A. Roller, Ž. L. Teši , B. K. Keppler, J. Serb. Chem. Soc. 76 (2011) 53-61.
20. T. D. Aicher, S. A. Boyd, M. J. Chicarelli, K. R. Condroski, R.J. Hinklin, A. Singh, US Pat. 20090156603 2007.
21. G. R. Lawton, H. R. Ranaivo, L. K. Chico, H. Ji, F. Xue, P. Martásek, L. J. Roman, D. M. Watterson, R. B. Silverman, Bioorg. Med. Chem. 17 (2009) 2371-2380.

22. High cytotoxic activity of complex **4** towards HCT-116 reported in ref [13] has recently been contradicted by ref [25].
23. C. A. Vock, C. Scolaro, A. D. Phillips, R. Scopelliti, G. Sava, P. J. Dyson, J. Med. Chem., 49 (2006) 5552-5561.
24. J. Zhao, K. E. Prosser, S. W. Chang, S. P. Zakharia, C. J. Walsby, Dalton Trans. 45 (2016) 18079-18083.
25. J. Zhao, D. Zhang, W. Hua, W. Li, G. Xu, S. Gou, Organometallics 37 (2018) 441-447.
26. F. Schmitt, P. Govindaswamy., O. Zava, G. Süss-Fink,L. Juillerat-Jeanneret, B. Therrien. J. Biol. Inorg. Chem. 14 (2009) 101-109.
27. S. Richter, S. Singh, D. Draca, A. Kate, A. Kumbhar, A. S. Kumbhar, Hey-Hawkins, Dalton Trans. 45 (2016) 13114-13125.
28. P. Chuklin, V. Chalermpanaphan, T. Nhukeaw, S. Saithong, K. Chainok, S. Phongpaichit, N. Leesakul, J. Organomet. Chem. 846 (2017) 242-250.
29. A. Inagaki, D. G. Musaev, T. Toshifumi, H. Suzuki, K. Morokuma, Rensburg, P. J. Steynberg, W Organometallics. 22 (2003) 1718-1727.
30. W. Janse van Rensburg, P. J. Steynberg, W. H. Meyer, M. M. Kirk, G. S. Forman, J. Am. Chem. Soc. 126 (2004) 14332-14333.
31. D. Benitez, W. A. Goddard, J. Am. Chem. Soc. 127 (2005) 12218-12219.
32. C. Kreitner, E. Erdmann, W. W. Seidel, K. Heinze, Inorg. Chem. 54 (2015) 11088-11104
33. D. Das, A. Dutta, P. Mondal, Comput. Theor. Chem. 1072 (2015) 28-36.
34. M.A. Bennett, T.W. Matheson, J. Organomet. Chem. 175 (1979) 87-93.
35. B. S. Jensen, J. S. Rodger, D. M. Spicer, J. Organomet. Chem. 556 (1998) 151-158.
36. D.D. Perrin, W.L.F. Armarego, Pergamon Press, New York (1988).
37. W. J. Geary, Coord. Chem. Rev. 7 (1971) 81-122.
38. M.J. Frisch, G.W. Trucks, H.B. Schlegel, G.E. Scuseria, M.A. Robb, J.R. Cheeseman, G. Scalmani, V. Barone, G.A. Petersson, H. Nakatsuji, X. Li, M. Caricato, A. Marenich, J. Bloino, B.G. Janesko, R. Gomperts, B. Mennucci, H.P. Hratchian, J.V. Ortiz, A.F. Izmaylov, J.L. Sonnenberg, D. Williams-Young, F. Ding, F. Lipparini, F. Egidi, J. Goings, B. Peng, A. Petrone, T. Henderson, D. Ranasinghe, V.G. Zakrzewski, J. Gao, N. Rega, G. Zheng, W. Liang, M. Hada, M. Ehara, K. Toyota, R. Fukuda, J. Hasegawa, M. Ishida, T. Nakajima, Y. Honda, O. Kitao, H. Nakai, T. Vreven, K. Throssell, J.A. Montgomery, Jr., J.E. Peralta, F. Ogliaro, M. Bearpark, J.J. Heyd, E. Brothers, K.N. Kudin, V.N. Staroverov, T. Keith, R. Kobayashi, J. Normand, K. Raghavachari, A. Rendell, J.C. Burant, S.S. Iyengar, J. Tomasi, M. Cossi, J.M. Millam, M. Klene, C. Adamo, R. Cammi, J.W. Ochterski, R.L. Martin, K. Morokuma, O. Farkas, J.B. Foresman, D.J. Fox, Gaussian, Inc., Wallingford CT, (2016).
39. M. Sekiya, T. Noro, T. Koga, T. Shimazaki, Theor. Chem. Acc. 131 (2012) 1247.
40. R. Aronson, M.R.J. Elsegood, J.W. Steed, D.A. Tocher, Polyhedron 10 (1991) 1727-1732.

□□□

41. M. A. Bennett, A. K. Smith, Dalton Trans. 2 (1974) 233-241.
42. A. Rodriguez-Barzano, J. D. A. Fonseca, A. John Blacker, P. C. McGowan, Eur. J. Inorg. Chem. 11 (2014) 1974-1983.
43. M.E. Reichmann, S. A. Rice, C. A. Thomas, P. A. Doty, J. Am. Chem. Soc. 76 (1954) 3047-3053.
44. N. Mudasir, H. Yoshioka, H. Inoue, J. Inorg. Biochem. 77 (1999) 239-247.
45. J.L. García-Giménez, G. Alzuet, M. Gonzáles-Alvarez, M. Liu-Gonzáles, A. Castiñeiras, J. Borrás, J. Inorg. Biochem. 103 (2009) 243-255.
46. F. Denizot, R. Lang, J. Immunol. Methods 89 (1986) 271-277.
47. F. H. Allen, Acta Crystallogr., Sect. B: Struct. Sci. 58 (2002) 380–388.
48. F. White, P. Sadler, M. Melchart, CSD Private Communication, (2015).
49. C. M. Standfest-Hauser, K. Mereiter, R. Schmid, K. Kirchner, Dalton Trans. 11 (2003) 2329-2334.
50. X. W. Yan, Y. R. Xie, Z. M. Jin, M. L. Hu, L. P. Zhou, Appl. Organomet. Chem. 32 (2018) 3923.
51. K. Nakamoto, M. Margoshes, R. E. Rundle, J. Am. Chem. Soc. 77 (1955) 6480-6486.
52. Thus, unlike many arene-Ru complexes investigated for cytotoxicity, 2-aminopyridine complexes do not have the high-lying filled and low-lying empty ligand -orbitals found e.g. in bipyridyl-type complexes. It is therefore not possible to interpret electronic spectra or voltammetry experiments analogously to those systems that have 'redox-non-innocent' ligands. However, as noted in the section on voltammetry, this situation appears to change in oxidized states.
53. P. Hosseinzadeh, Y. Lu, Biochim. Biophys. Acta (BBA)-Bioenergetics. 1857 (2016) 557-581.
54. While there is no direct expectation from the electronic structure calculations that the arene ligand should be displaced, an oft-quoted rationalization for irreversible oxidation processes, the bond strength to the *p*-cymene group may be weakened in such 17*e* complexes as evidenced by longer Ru–cymene-ring-centroid distances (see Figure S10 in the SI.)
55. R. S. Nicholson, Anal. Chem. 38 (1966) 1406-1406.
56. B. Draži , S. Grguri -Šipka, I. Ivanovi , Ž. L. Teši , G. Popovi , J. Iran. Chem. Soc. 9 (2012) 7-12.
57. G. Gasser, N. Metzler-Nolte, Curr. Opin. Chem. Biol. 16 (2012) 84-91.
58. A. F. Peacock, P. J. Sadler, Chem. Asian J. 3 (2008) 1890-1899.
59. A. M. Pyle, J. P. Rehmann, R. Meshoyrer, C. V, Kumar, N. J. Turro, J. K Barton, J. Am. Chem. Soc. 111 (1989) 3051-3058.
60. E. C. Long, J. K. Barton, Acc. Chem. Res. 23 (1990) 271-273.
61. R. N. Irobalieva, J. M. Fogg, D. J. Catanese, T. Sutthi Butpong, M. Chen, A. K. Barker, S. J. Ludke, S. A. Harris, M. F. Schmid, W. Chiu, L. Zechi Edrich, Nat. Comm. 6 (2015) 8440.
62. G. Pratviel, J. Bernadou, B. Meunier, Adv. Inorg. Chem. 45 (1998) 251-312.
63. R. Amutha, V. Subramanian, B. U. Nair, Chem. Phys. Letts. 344 (2001) 40-48.

64. T. Afrati, A.A. Pantazaki, C. Dendrinou-Samara, C. Raptopoulou, A. Terzis, D.P. Kessissoglou, Dalton Trans. 39 (2010) 765-775.
65. Y. M. Chang, C. K. M. Chen, M. H. Hou, Int. J. Mol. Sci. 13 (2012) 3394-3413.
66. N. Shahabadi, S. Kashanian, M. Khosravi, M. Mahdavi, Trans. Met. Chem. 35 (2010) 699-705.
67. G. R. Bishop, J. B. Chaires, John Wiley & Sons Inc., New York, (2002).
68. A. Rodger, B. Nordén, Oxford University Press, 1 (1997).
69. L. W. Yielding, D. E. Graves, B.R. Brown, K.L. Yielding. Biochem. Biophys. Res. Commun. 30 (1979) 424-32.
70. S. Moon, M. Hanif, M. Kubanik, H. Holtkamp, T. Söhnel, S. M. Jamieson, C. G. Hartinger. ChemPlusChem, 80 (2015) 231-236.
71. Q. A. Paula, A. A. Batista, E. E. Castellano, J. Ellena, J. Inorg. Biochem. 90 (2002) 144-148.
72. J. A. Davies, Adv. Inorg. Chem 24 (1981) 115-187.
73. R. E. Morris, E. R. Aird, P. del Socorro Murdoch, H. Chen, J. Cummings, N. D. Hughes, S. Parsons, A. Parkin, G. Boyd, J. I. Duncan, P. J. Sadler, J. Med. Chem. 44 (2001) 3616-3621.
74. R. E. Aird, J. Cummings, A. A. Ritchie, M. Muir, R. E. Morris, H. Chen, D. I. Jodrell, D, Br. J. Cancer. 86 (2012) 1652.
75. Patra *et al*. have reported that DMSO will displace monodentate pyridine ligands in type-A complexes and since DMSO was employed as the transfer vector for the metal complexes to the biological media in all these tests, the possibility exists that it is the aminopyridines that are the active agents – see reference [18].
76. N. J. Greenfield, Nature protocols. 1 (2006) 2876.

Ruthenium(II)-arene complexes with monodentate aminopyridine ligands: insights into redox stability, electronic structures and biological activity†

Flávia Marszaukowski[a], Ivelise Dimbarre Lao Guimarães[a], Juliana Paula da Silva[a], Luis Henrique da Silveira Lacerda[a], Sergio Ricardo de Lazaro[a], Márcio Peres de Araujo[b], Patrícia Castellen[a], Tania Toyomi Tominaga[c], René T. Boeré[d] and Karen Wohnrath[a]*

Highlights

- Four ruthenium(II) arene complexes with monodentate pyridine ligands, [(η^6–*p*-cymene)$RuCl_2$L]: L = 2-aminopyridine, 2-methylaminopyridine, 2-benzylaminopyridine, and pyridine, are synthetized and fully characterized.
- A crystal structure of [(η^6–*p*-cymene)$RuCl_2$(2-methylaminopyridine)] displays considerable complexity, due to the presence of the $CHCl_3$ solvent of crystallization, two independent molecules in the asymmetric unit and a wholesale disorder of the aminopyridine ligand. There are ligand N–H to metal-bound chloride hydrogen bonds.
- The lack of cytotoxic activity of these complexes against the HeLa cell line could be attributed to having only electrostatic interactions between partly hydrolyzed cationic complexes and the phosphate backbone of DNA, via a study of their interactions with Calf Thymus-DNA
- Cyclic voltammetry of these complexes determined a large electrochemical stability window (>2.2 V) extending well beyond the physiological E° range.

Ruthenium(II)-arene complexes with monodentate aminopyridine ligands: insights into redox stability and electronic structures and biological activity†

Flávia Marszaukowski[a], Ivelise Dimbarre Lao Guimarães[a], Juliana Paula da Silva[b], Luis Henrique da Silveira Lacerda[a], Sergio Ricardo de Lazaro[a], Márcio Peres de Araujo[b], Patrícia Castellen[a], Tania Toyomi Tominaga[c], René T. Boeré[d] and Karen Wohnrath[a]*

Supplementary Information

Table of Contents Page No.

X-ray Crystallography of complex **2**

Table S1 Crystal data and structure refinement for **2**

Identification code	**2**
Empirical formula	$C_{16}H_{22}Cl_2N_2Ru$
Formula weight	414.32
Temperature/K	106.1(2)
Crystal system	triclinic
Space group	P-1
a/Å	7.1596(2)
b/Å	13.0648(3)
c/Å	21.1857(6)
α/°	107.809(3)
β/°	93.451(2)
γ/°	90.028(2)
Volume/Å^3	1882.93(9)
Z	4
ρ_{calc}g/cm^3	1.462
μ/mm^{-1}	1.112
F(000)	840.0
Crystal size/mm^3	0.40 × 0.20 × 0.05
Radiation	MoKα (λ = 0.71073)
2Θ range for data collection/°	6.78 to 63.684
Index ranges	-9 ≤ h ≤ 8, -19 ≤ k ≤ 18, -31 ≤ l ≤ 31
Reflections collected	46573
Independent reflections	10400 [R_{int} = 0.0378, R_{sigma} = 0.0318]
Data/restraints/parameters	10400/40/461
Goodness-of-fit on F^2	1.318
Final R indexes [I>=2σ (I)]	R_1 = 0.0529, wR_2 = 0.1106
Final R indexes [all data]	R_1 = 0.0574, wR_2 = 0.1120
Largest diff. peak/hole / e Å^{-3}	0.86/-1.77
Empirical formula	$C_{16}H_{22}Cl_2N_2Ru$

Details of the structure determination

Large but thin plates of ruthenium complex **2** were grown by vapour diffusion of diethyl ether into a chloroform solution of the complex and were investigated by X-ray diffraction. The best data was obtained using Mo radiation but datasets were also obtained using a Cu source. Although the data quality is excellent, the structure is challenging due to multiple factors. It contains $CHCl_3$ of solvation, with an approximate refined occupancy of 92% but with large displacements. In addition there are two independent molecules in the asymmetric unit and both complexes display complete positional disorder of their 2-CH_3NH-pyridine ligands, with as a result significant overlapping of the atom sites. To reduce this complexity, the contribution of the solvent was removed using the Solvent Mask within Olex2. The solvent void was determined to have a volume of 285 Å^3 and to contain about 99 *e* (one $CHCl_3$ is actually about 58 *e*) according to the Solvent Mask routine. However, a *solvent accessible surface* analysis in Mercury CSD, release 3.10.1, assigns a volume of 51 Å^3 to the cavities. Note that the microchemical analysis of the synthetic sample indicated the presence of residual chloroform (see Section 2.5 of the main article; due to losses, only 17% CHCl3 was determined by this method.)

With the solvent out of the way, the next step was to develop a **meapy** ligand disorder model, which was very successful (see Fig. S1a) and could be refined anisotropically for the major components (75% for the Ru1 molecule and 63% for the Ru2 molecule) and isotropically for the minor components. Significant restraints are required in the model as the atom sites overlap extensively. In the structures there is NH···Cl H-bonding, and in order to preserve this for both of the **meapy** orientations, the ligands must be displaced left or right and thus even the Ru-bound pyridyl nitrogen atoms (N1, N3) have disordered positions. Literally the whole of the **meapy** groups are flipped over and offset in both independent molecules. Similar disorders were encountered in crystals of **2** grown by slow cooling of chloroform and also chlorobenzene solutions, and we were unable to crystallize this complex from any solvent that was not disordered (see, for example, the poorly refined structure depicted for **2** in Fig. S1b.)

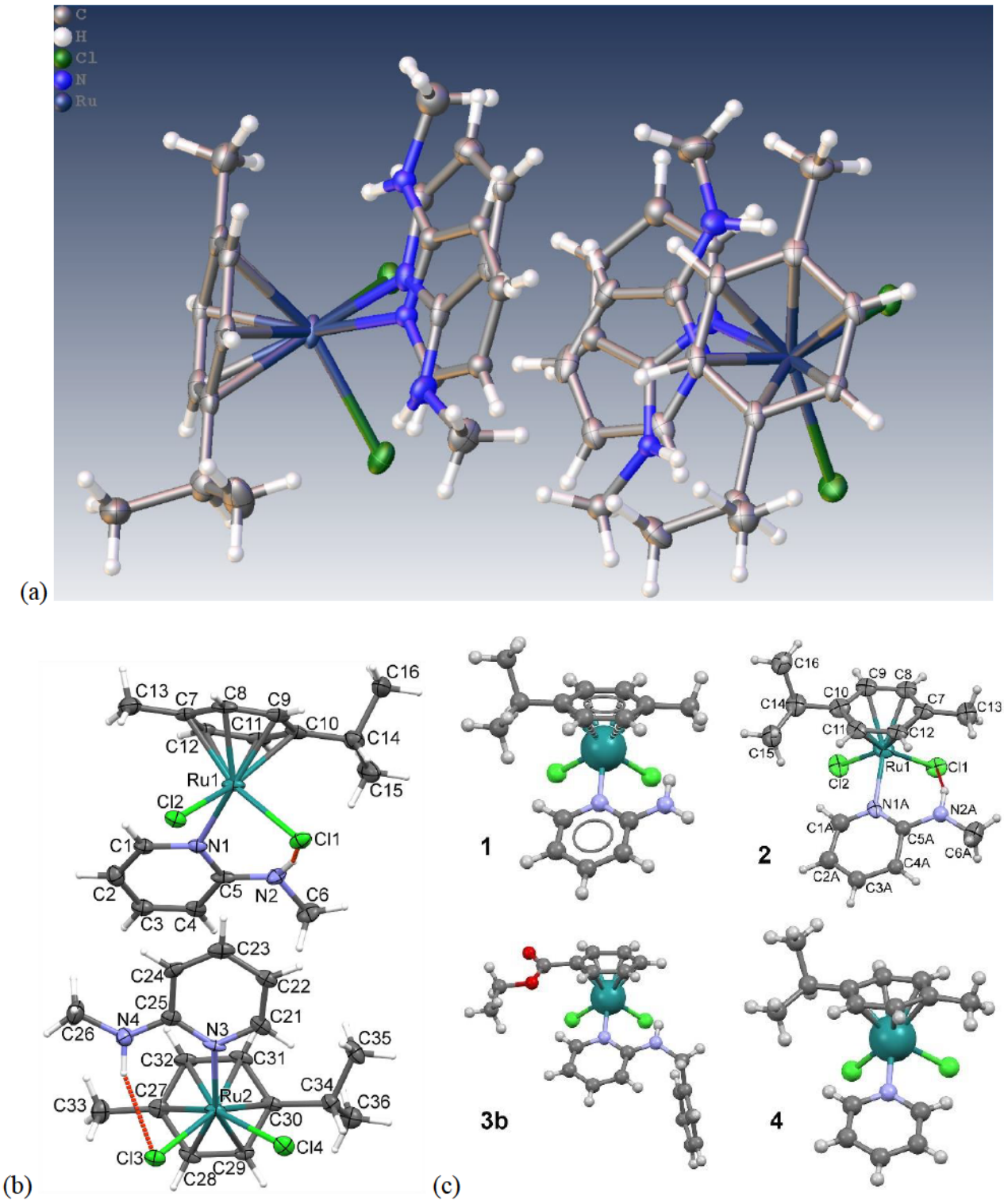

Figure S1 (a) Depiction of the disorder model developed for the structure of **2**. (b) Displacement ellipsoids (50% probability) plot of the two independent molecular structures of **2** as found in the crystal lattice, with the full atom numbering scheme. (c) Molecular structures of **1**–**4** from new and published crystal structures. **1**, MIXSOD01 [1]; **2**, displacement ellipsoids (40% probability) plot showing the atom numbering scheme and the major component of disordered **meapy** obtained from a solvent-free crystal in $P2_1/c$ grown by evaporation rather than vapour diffusion; **3b**, OHICAL [2]; **4**, JOBCOS [3].

Table S2 Selected interatomic distances (Å) and angles (°) from single crystal X-ray analysis for complexes **1**, **2**, **3b** and **4**. The atom numbering scheme employed is that of the major component in the crystal structure of **2** as in Fig. 1.

Parameter	**1** [a]	**2** X-ray [b]	**2** DFT [c]	**3b** [d]	**4** [e]
Ru1-Cl1	2.409(2)	2.434(1)	2.497	2.4073(4)	2.4194(4)
Ru1-Cl2	2.421(2)	2.424(1)	2.461	2.3915(5)	2.421(2)
Ru1-*c*Ar [f]	1.666	1.668	1.765	1.657	1.662
Ru1-N1	2.161(6)	2.177(6)	2.195	2.171(1)	2.4026(4)
N2···Cl1	3.243(7) [g]	3.213(9)	3.161	3.147(1)	—
H2A···Cl1	2.583	2.34(11)	2.190	2.648	—
*c*Ar-Ru-Cl1 [f]	127.35	126.49	124.24	126.61	129.00
*c*Ar-Ru-Cl2 [f]	126.70	127.20	126.74	127.09	126.86
*c*Ar-Ru-N1 [f]	127.64	125.62	127.03	126.91	126.83
Ru1-N1-C3	170.9(3)	169.0(4)	168.88	171.51(8)	172.79(7)
Cl1-Ru-Cl2	85.65(7)	86.34(6)	88.17	85.79(1)	87.33(1)
Cl1-Ru-N1	88.6(2)	93.61(19)	91.83	90.63(4)	85.94(3)
Cl2-Ru-N1	87.2(2)	87.7(2)	86.80	86.60(4)	86.81(3)
N2-H2A···Cl1	122.4	153(9)	158.25	117.05	—

[a] JOBCOS. [b] This work; mean values of the two independent molecules in the asymmetric unit. [c] For a picture, see the ESI. [d] OHICAL. [e] MIXSOD01. [f] The η^6–arene ring centroid as calculated in Mercury-CSD. [g] *d*(N2···Cl2') = 3.234(7) Å.

Molecular Structures of the Complexes

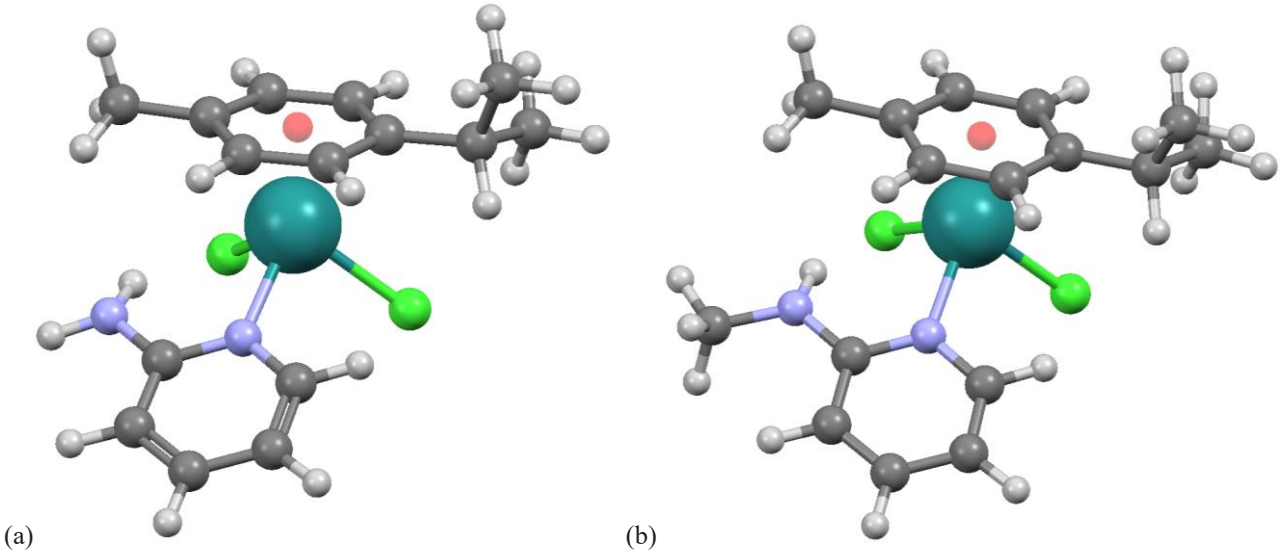

(a) (b)

Figures S2 DFT calculated structures of **1** and **2** in the gas phase (See page S28 and S32 for Cartesian coordinates)

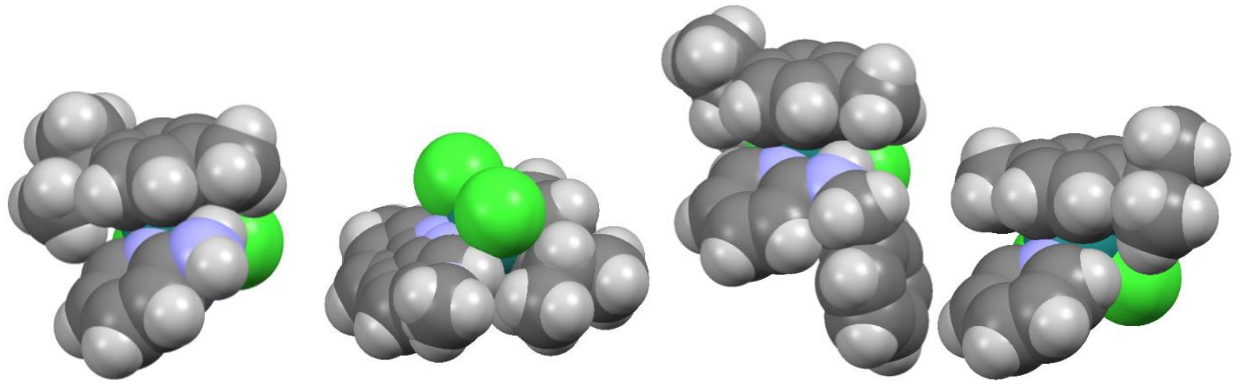

1 **2** **3** **4**

Figure S3 Space-filling representations of the structures of **1** - **4**

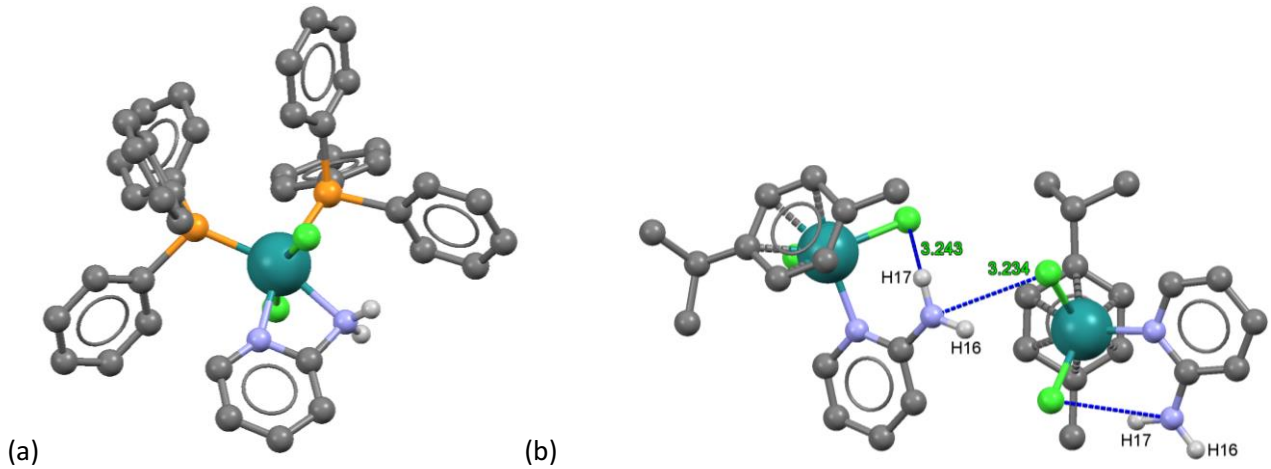

(a) (b)

Figure S4 (a) The κ2 *N,N*-chelating geometry of ligand **2-apy** as found in CSD refcode: IHIWAX [4]
(b) N-H···Cl hydrogen bonding the crystal lattice of **1** (CSD refcode: JOBCOS)

Vibrational spectroscopic data

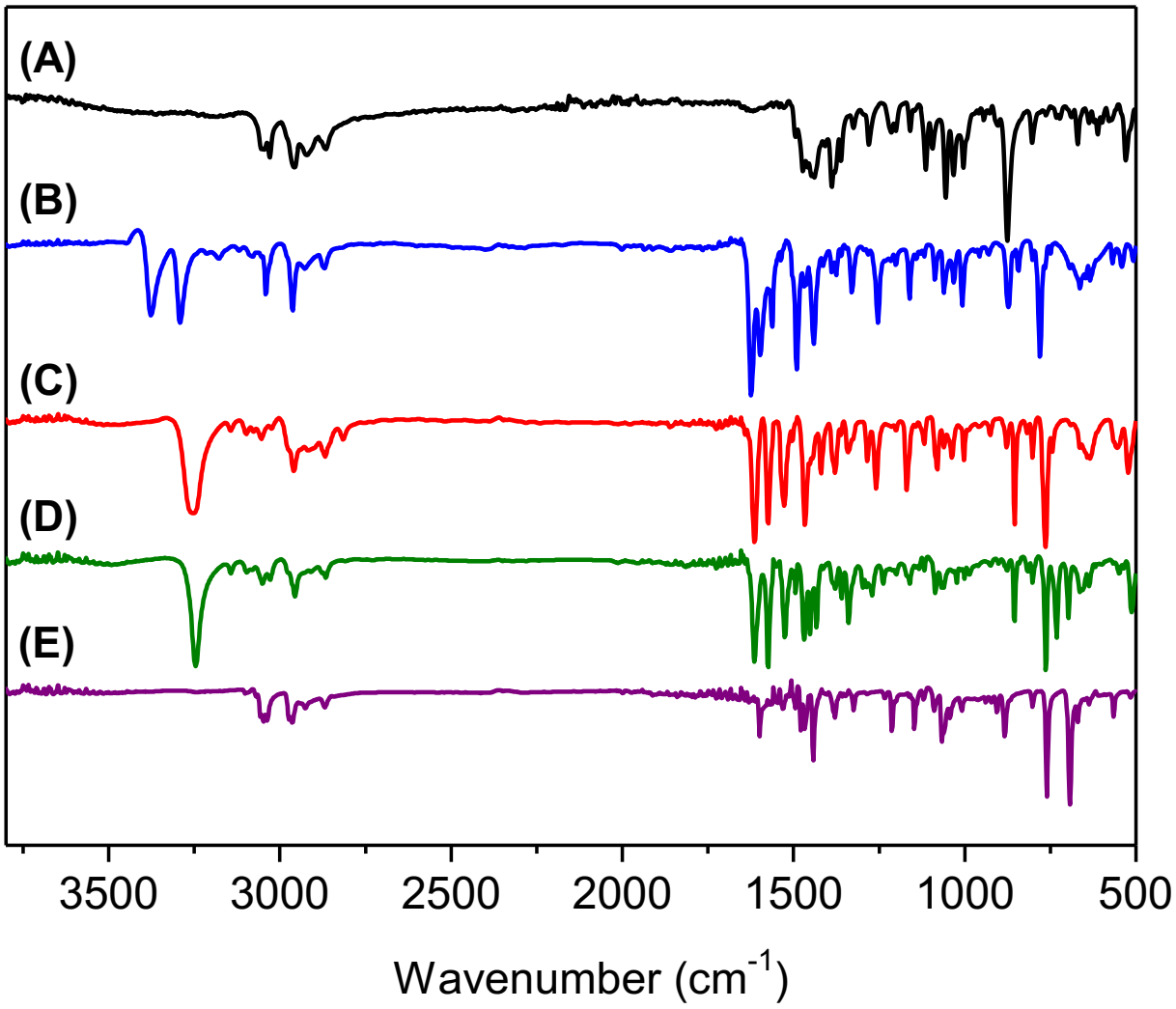

Figure S5 FTIR spectra for: (A) precursor complex; (B) complex **1**; (C) complex **2**; (D) complex **3**; (E) complex **4**.

Table S3 FTIR data for [{(*p*-cymene)Ru(μ-Cl)Cl}$_2$] and complexes **1**–**4** in the wavelength range 4000 to 400 cm^{-1}.

Assignment	Precursor	1	2	3	4
ν_{asN-H}	___	3372 3290	3259	3238	___
d(N···Cl), Å		3.234 intermol.[a] 3.243 intramol.[a]	3.165[b]	3.147[c]	___
$\nu_{asCsp2-H}$	3035	3040	3051	3046	3046
$\nu_{asCsp3-H}$	2963, 2912, 2870	2966, 2863	2953, 2870	2953, 2860	2963, 2852
$\nu_{as\ C=N}$	___	1594	1573	1573	1531
$\nu_{asC=C}$	1619, 1475, 1444	1611, 1469, 1438	1615, 1473, 1429	1618, 1475, 1434	1600, 1468, 1437
ν_{C-H}	1279	1251	1259	1237	1210
ν_{as}c	1059	1061	1073	1067	1067
δ_{sC-H} (aromatic ring)	874	864	853	843	881
δ_{sC-H} (aromatic ring)	760	753	749	754	763, 703

[a] Crystal lattice (CSD refcode: JOBCOS). [b] X-ray structure of **2** (this work). [c] Crystal lattice (refcode: OHICAL)

The Raman spectra (Figure S5) of all complexes shown two bands in the region 246-392 cm^{-1} can be attributed to asymmetric stretch of (Ru-Cl) bond [5]. The wavelength values of these bands for the complexes **1-4** in relation to the precursor complex undergo a small change, where the bands are observed in greater frequency. This difference can be attributed to the coordination of ruthenium to pyridine ligands that are relatively good π acceptors and can remove electron density from the metal center, strengthening the Ru-Cl bond and shifting this signal to higher energy [6]. The coordination of *N*-heterocyclic ligands to the metal center was confirmed through of the band $\nu_{(Ru\text{-}N)}$ at approximately 450 cm^{-1} [7]. The difference between the wavelength values, 448, 454, 458 and 465 cm^{-1} found to complexes **1-4**, respectively, is provided by the decreased in the basicity of the groups NH_2, MeNH, BzNH substituted on ortho position of pyridine ring. Other bands are in accordance to the FTIR spectra.

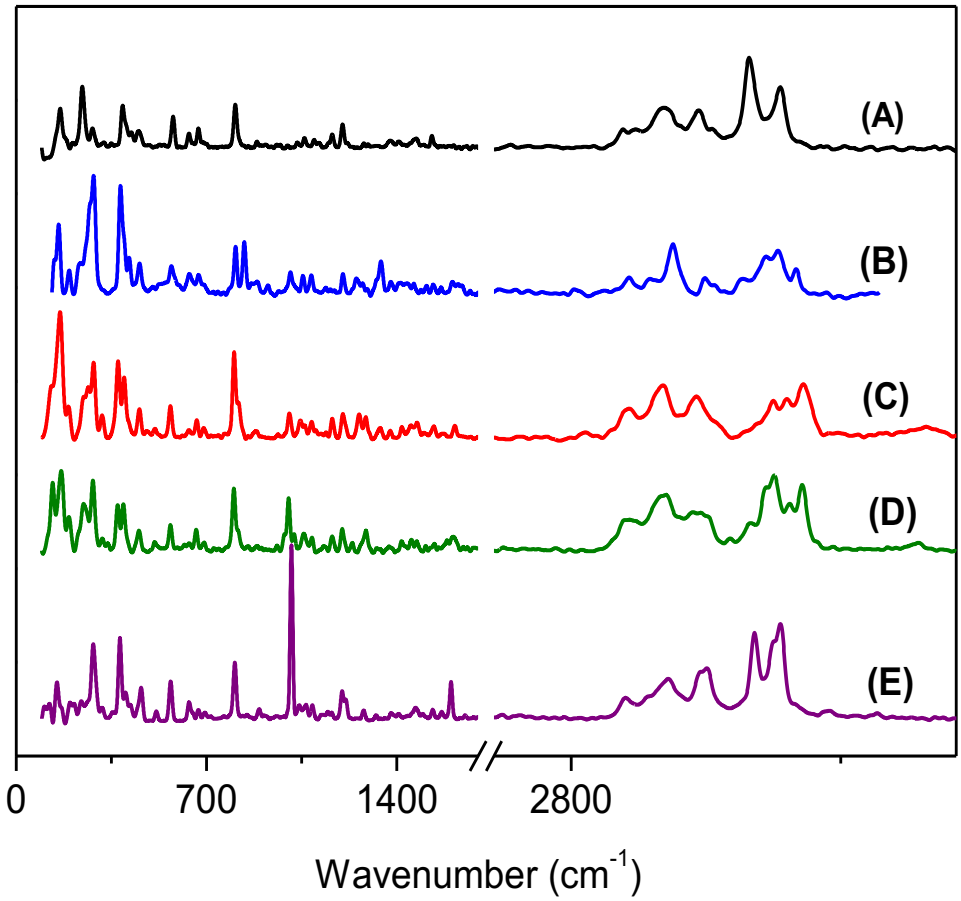

Figure S6 Raman scattering spectra, obtained in the solid state, for: (A) precursor complex; (B) complex **1**; (C) complex **2**; (D) complex **3**; (E) complex **4**.

Table S4 Raman scattering data for [{(*p*-cymene)Ru(μ-Cl)Cl}$_2$] and complexes **1**–**4**

Assignment	Precursor (cm^{-1})	**1** (cm^{-1})	**2** (cm^{-1})	**3** (cm^{-1})	**4** (cm^{-1})
$\nu_{asRu\text{-}Cl}$	246; 389	286; 392	283; 386	283; 382	273; 376
$\nu_{asRu\text{-}N}$	___	448	454	458	465
$\delta_{c\text{-}c}$	574	577	570	570	567
$\delta_{sC\text{-}H}$	806	800	799	796	797
$\nu_{asC\text{-}H}$	2919; 2963	2927; 2971	2875; 2917; 2963	2866; 2917; 2961	2871; 2927; 2971
$\nu_{asC\text{-}H}$	3028; 3070	3072	3060; 3101	3063; 3096	3036; 3071

Table S5 ^{1}H NMR data for complexes **1** – **4** in $CDCl_3$.[a]

Nucleus[b]	**1**	**2**	**3**	**4**
H^a	2.01 (s)	2.03 (s)	1.96 (s)	2.12 (s)
H^c	5.32 (d *5.4*)	5.28 (d *5.8*)	5.25 (d *5.5*)	5.24 (d *6.0*)
H^d	5.53 (d *5.4*)	5.51 (d *5.8*)	5.47 (d *5.5*)	5.46 (d *6.0*)
H^f	2.96 (sept *6.8*)	3.02 (sept *6.9*)	2.94 (sept 6.8)	3.02 (sept *6.9*)
H^g	1.29 (d *6.8*)	1.32 (d *6.9*)	1.28 (d *6.9*)	1.33 (d *7.0*)
H^h	8.54 (d *5.6*)	8.67 (d *5.0*)	8.71 (d *5.4*)	9.07 (m *2.6*)
H^i	6.54 (m *6.9*)	6.16 (t *6.2*)	6.61 (t *6.3*)	7.33 (m *4.7*)
H^i	7.30 (t *6.6*)	7.53 (t *7.2*)	7.44 (t *6.2*)	7.76 (tt *3.0*)
H^k	6.54 (m *6.9*)	6.47 (d *8.5*)	6.46 (d *8.4*)	—
H^m	—	2.87 (d *5.0*)	4.40 (d *5.5*)	—
$H^{n,o,p,q}$	—	—	7.36 (m *9.9*)	—
HN	6.16 (s *br.*)	7.70 (s *br.*)	8.10 (s *br.*)	—

[a] Ambient temperature. Spectra provided in Figs. S7,S8 [b] Identified as on Scheme 1. Entries are chemical shift (ppm from TMS) and (multiplicity *coupling* in Hz)

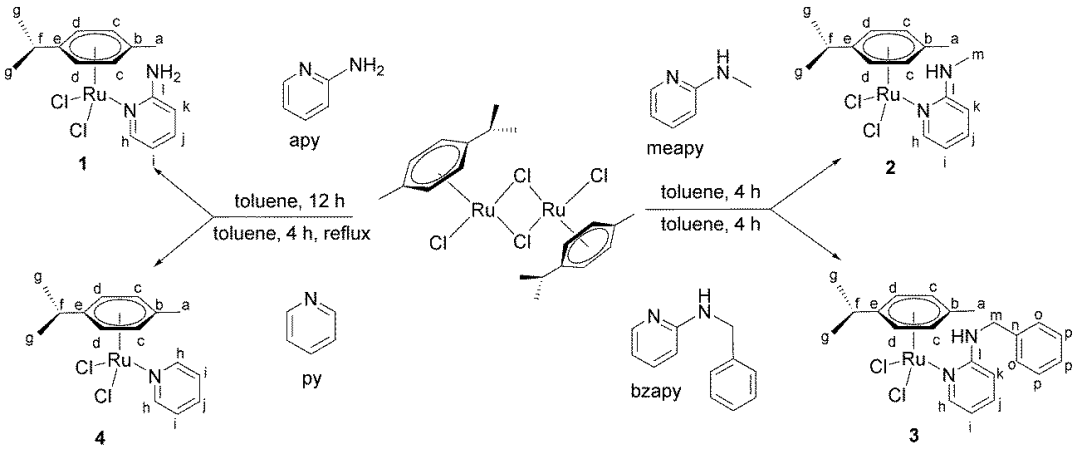

Scheme S1 Atom labels for unique C atoms, and by association their attached H-atoms in complexes **1-4**, as used in the NMR spectra.

The summarized NMR data provided in Table S5 may be compared to the actual ^{1}H NMR spectra shown on following pages. ^{13}C NMR spectra and a full set of 2D correlation spectra are also provided.

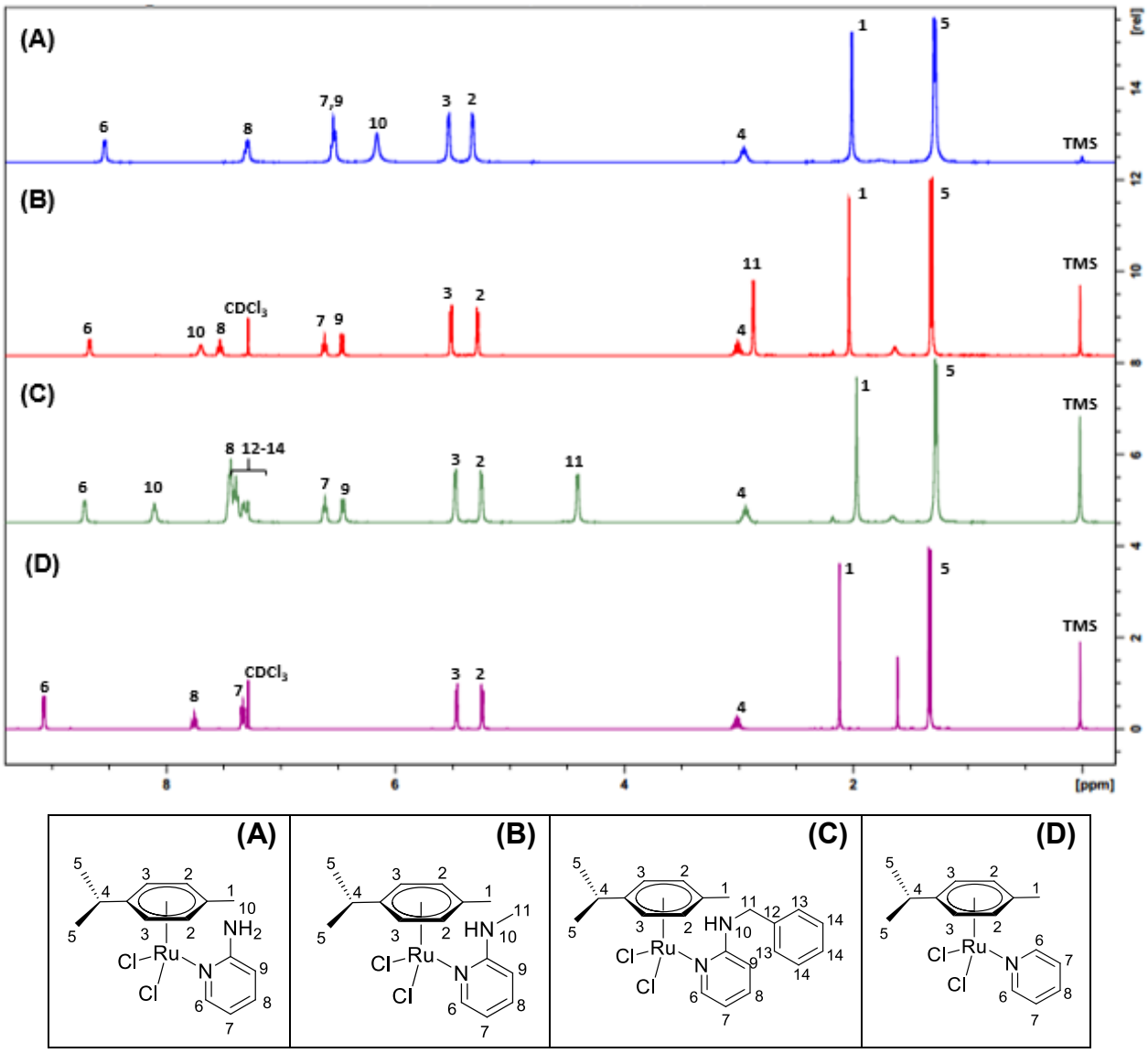

Figure S7 ^{1}H-NMR spectra in $CDCl_3$ (400 MHz) of the series of complexes [(η^6-*p*-cymene)$RuCl_2$(N)]. (A) complex **1**; (B) complex **2**; (C) complex **3**; (D) complex **4**.

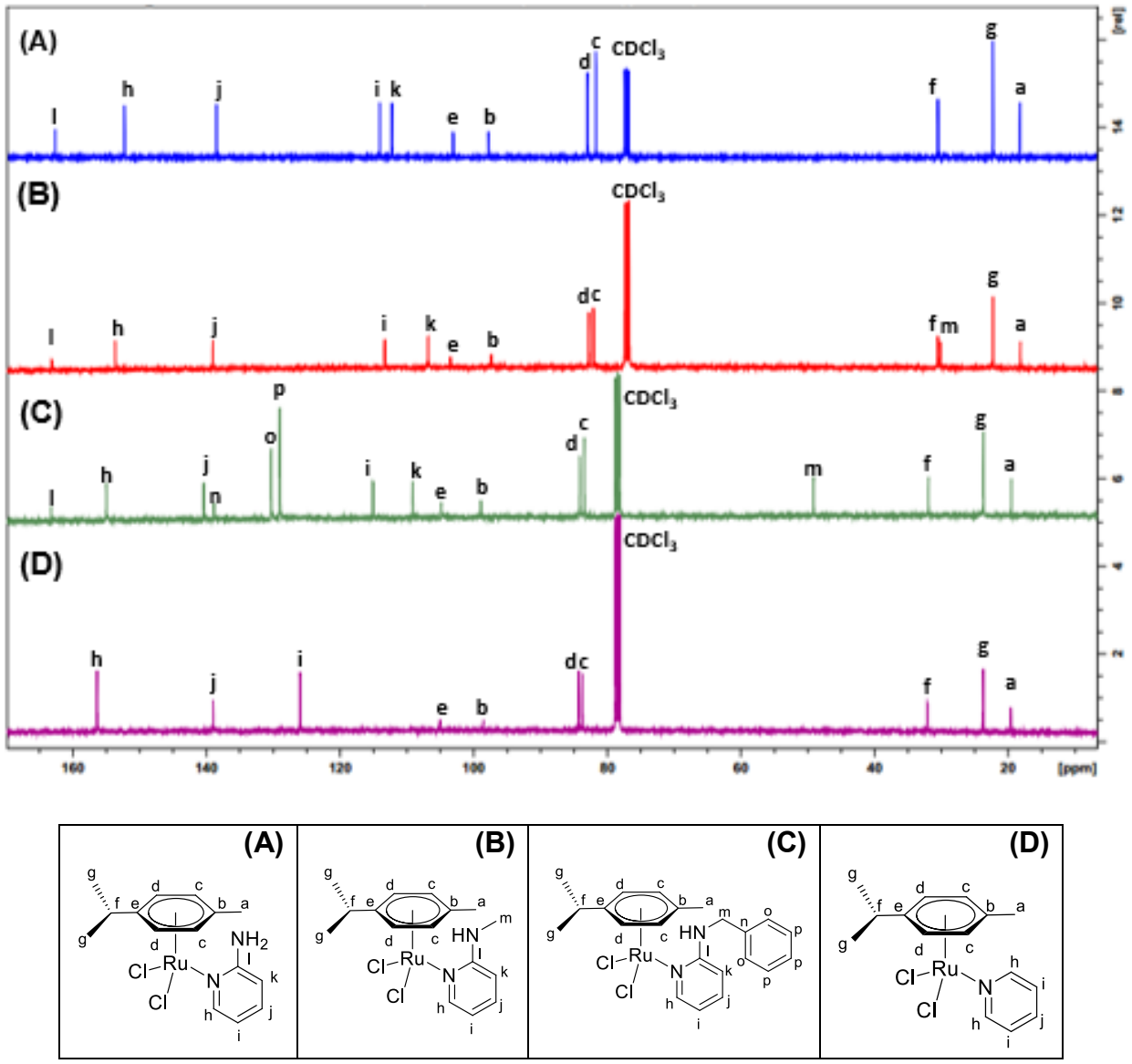

Figure S8 ^{13}C-NMR spectra in $CDCl_3$ (100.6 MHz) of the series of complexes [(η^6-*p*-cymene)$RuCl_2$(N)]. (A) complex **1**; (B) complex **2**; (C) complex **3**; (D) complex **4**

[(η^6-*p*-cimeno)RuCl$_2$(apy)]

- ^{1}H–^{1}H gCOSY

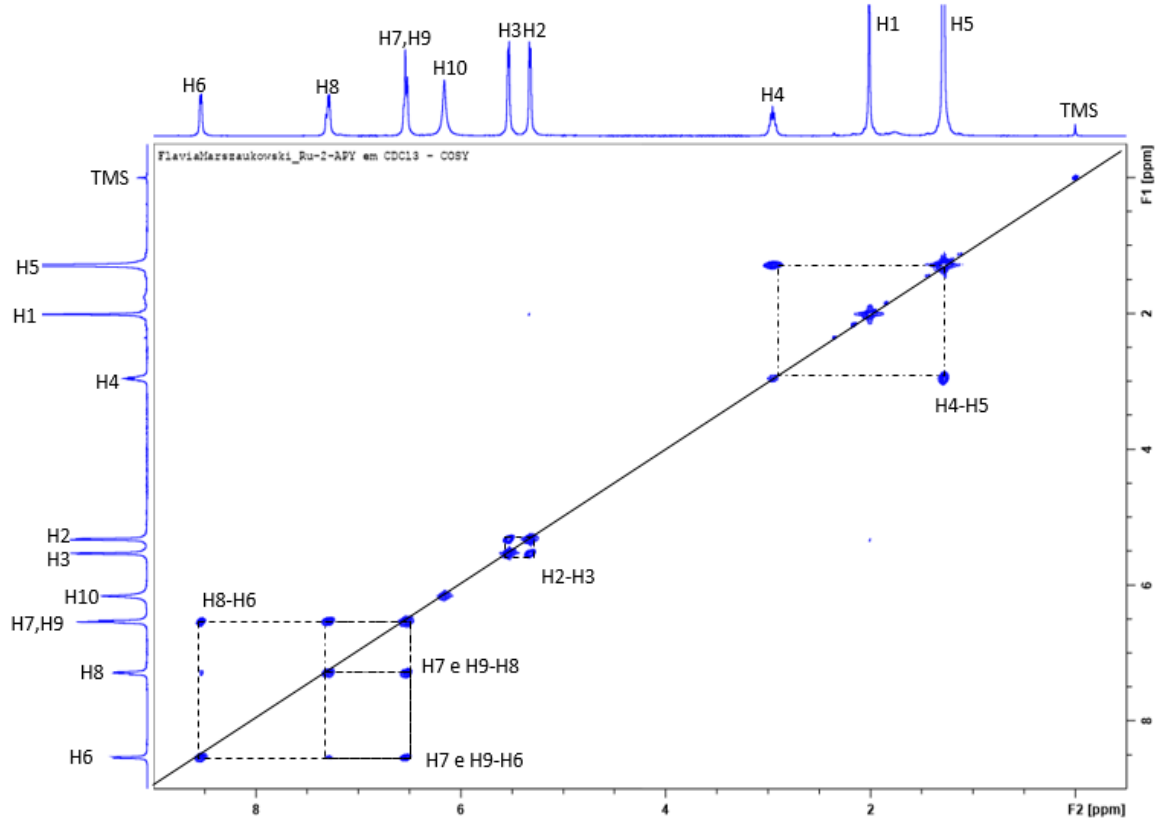

- ^{1}H–^{13}C gHSQC

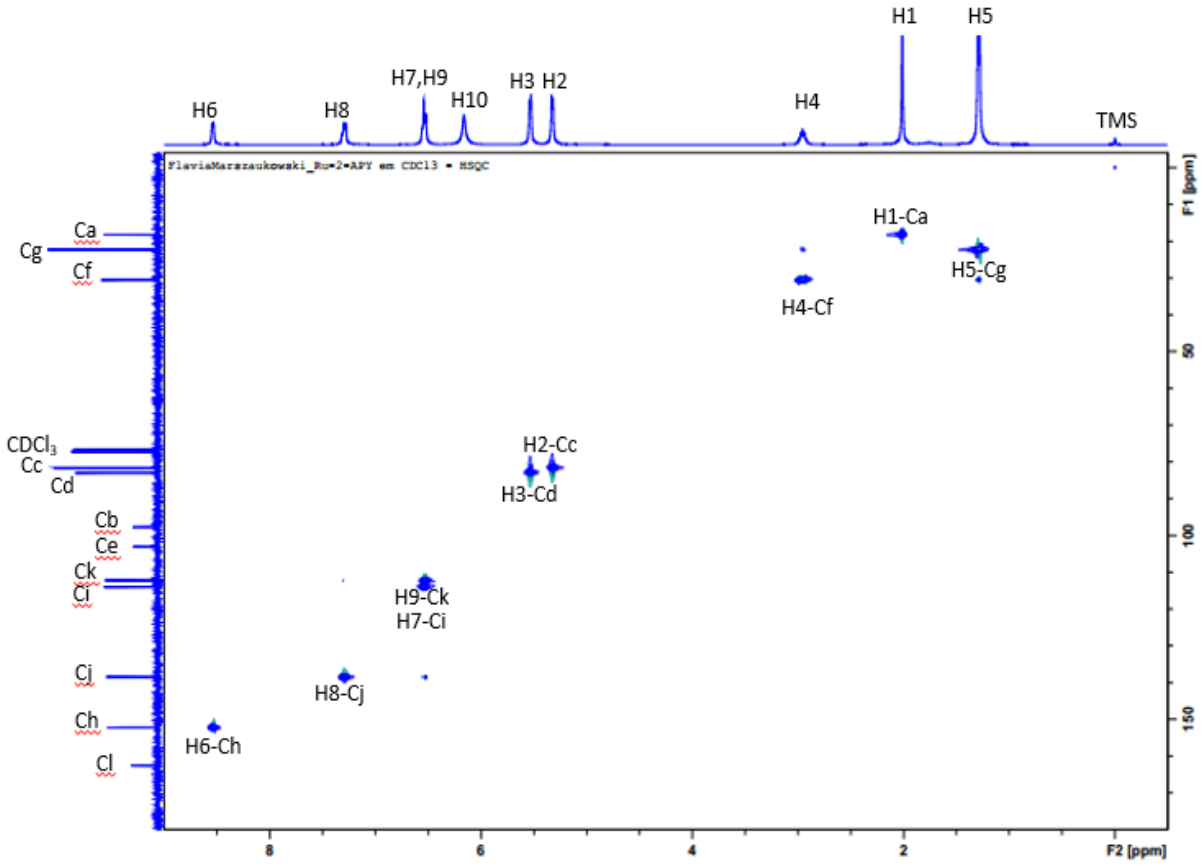

- $^{1}H–^{13}C$ gHMBC

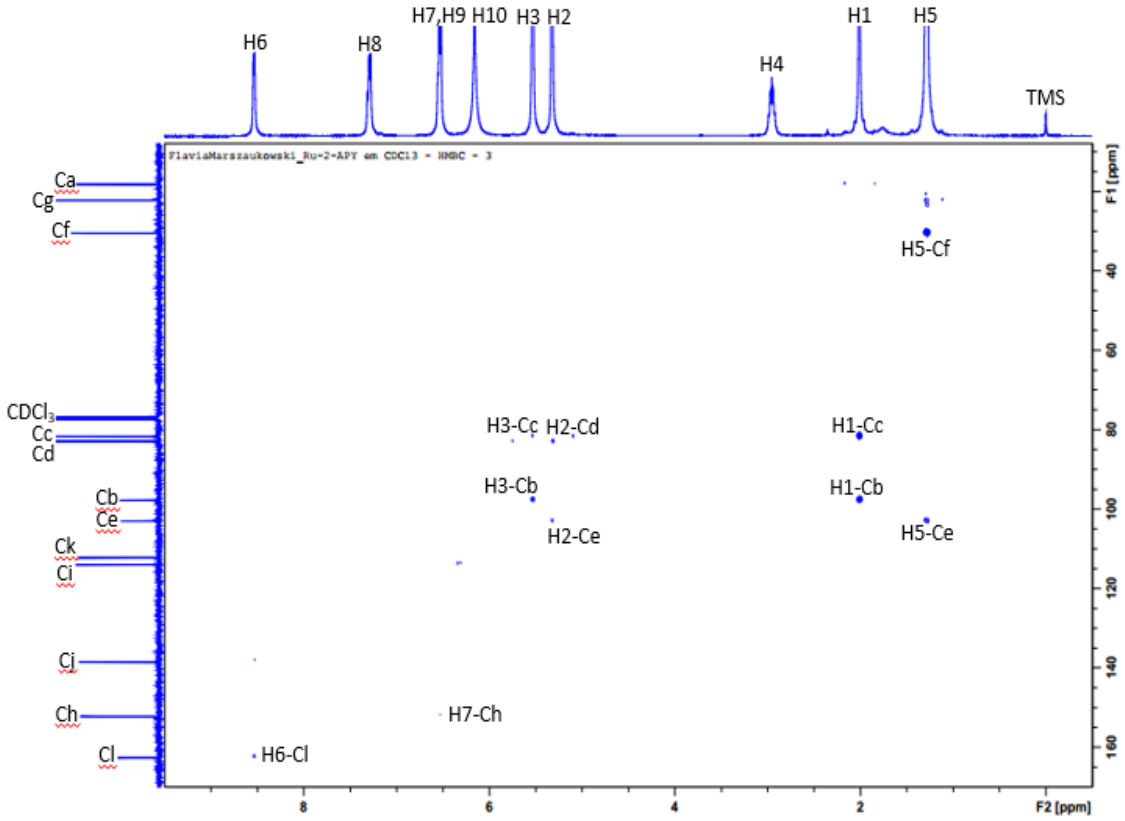

[(η^6-*p*-cimeno)$RuCl_2$(meapy)]

- $^{1}H–^{1}H$ gCOSY

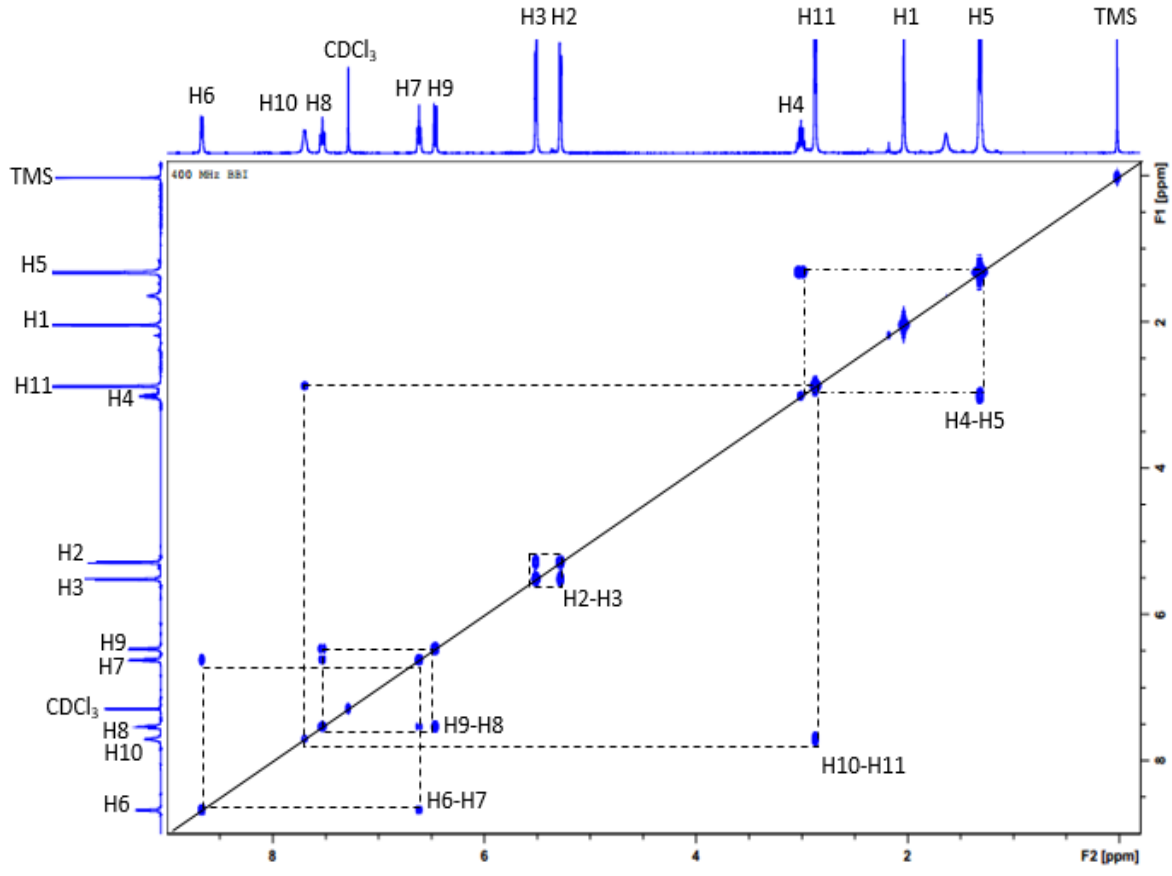

$^{1}H–^{13}C$ gHSQC

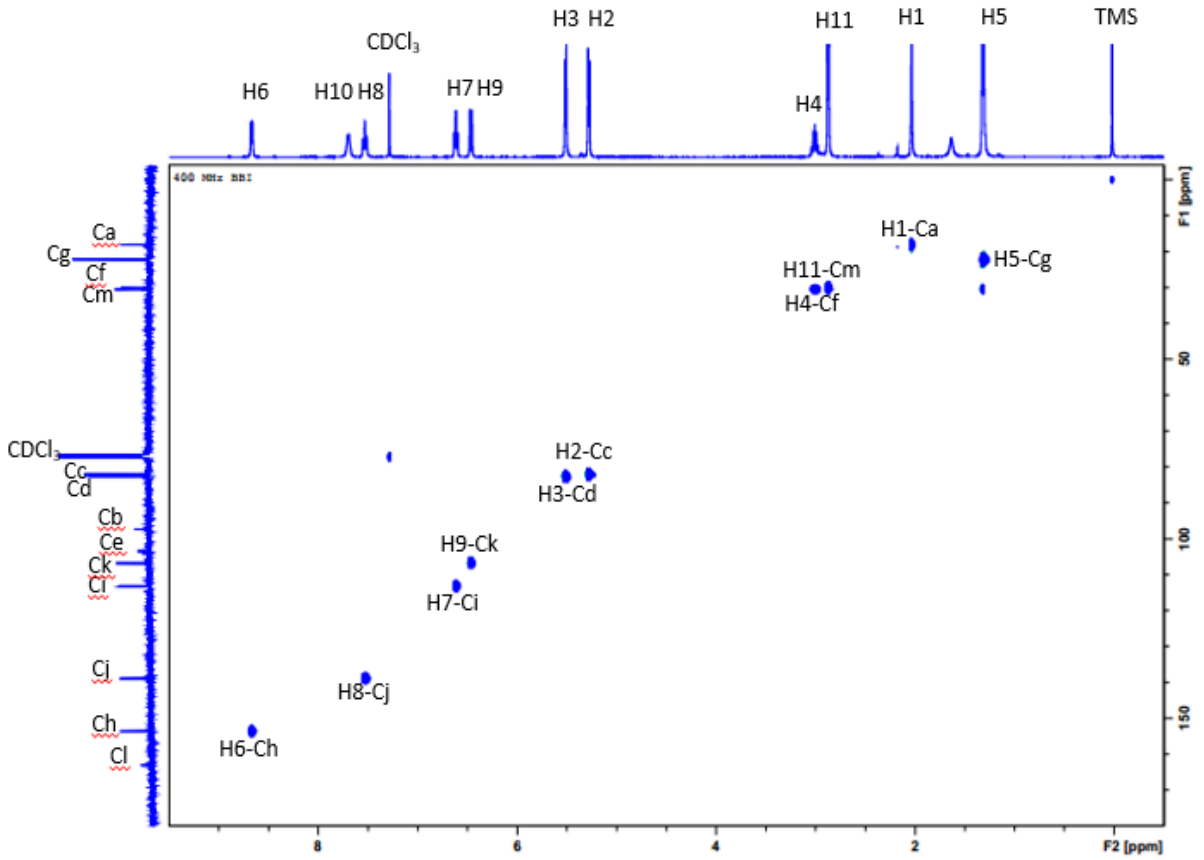

- $^{1}H–^{13}C$ gHMBC

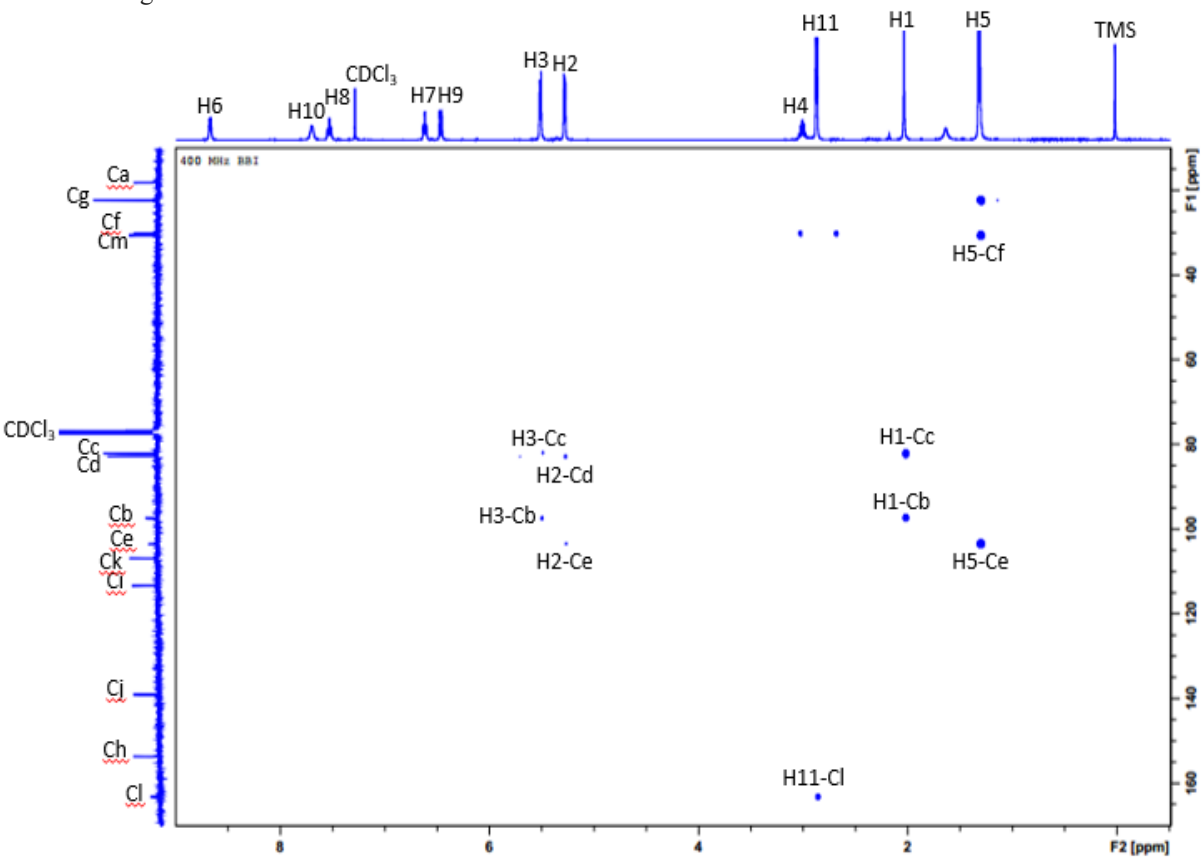

[(η^6-*p*-cimeno)RuCl$_2$(bzapy)]

- ^{1}H–^{1}H gCOSY

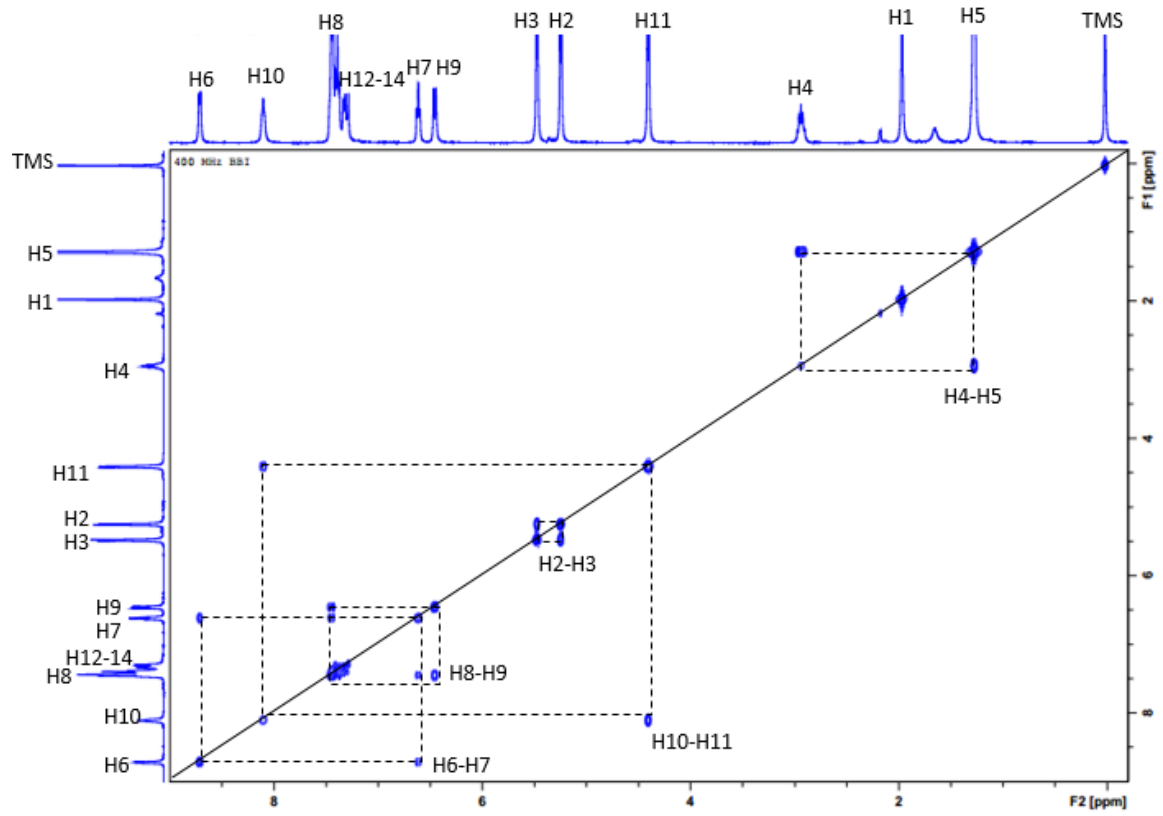

- ^{1}H–^{13}C gHSQC

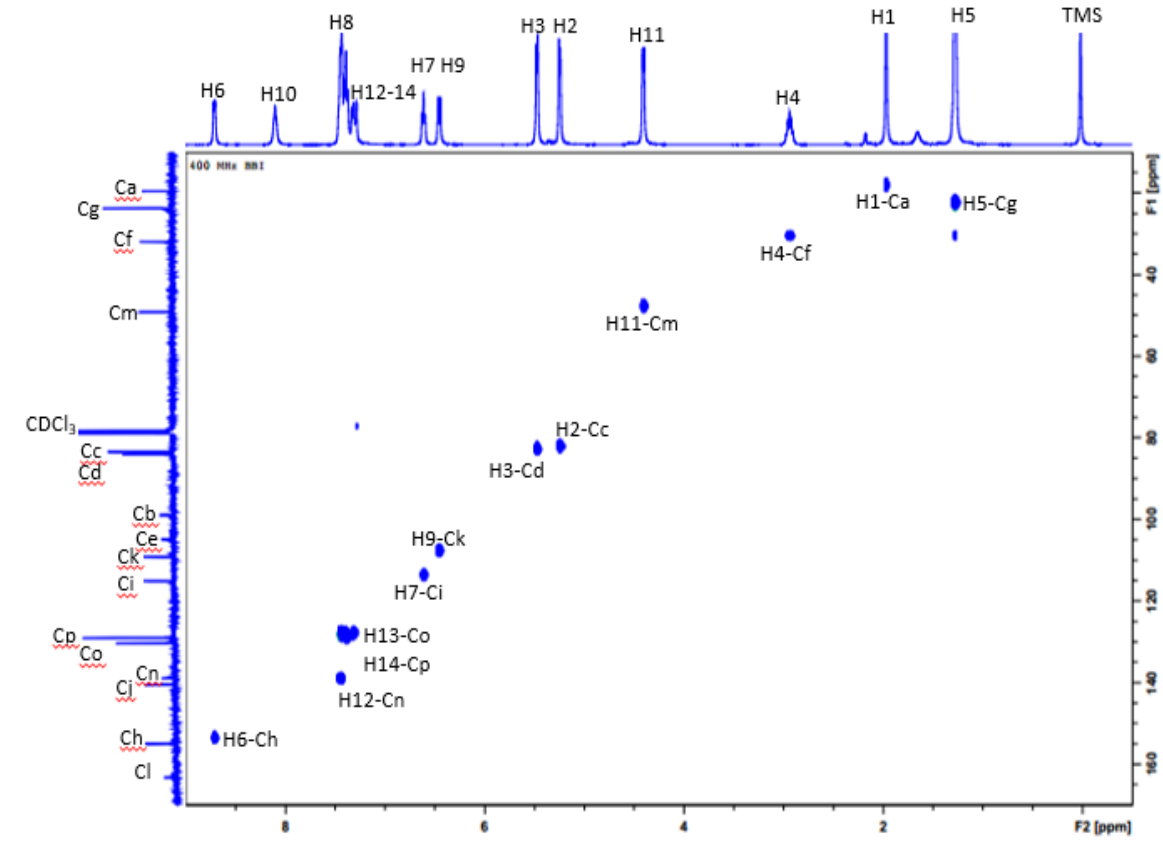

- $^{1}H–^{13}C$ gHMBC

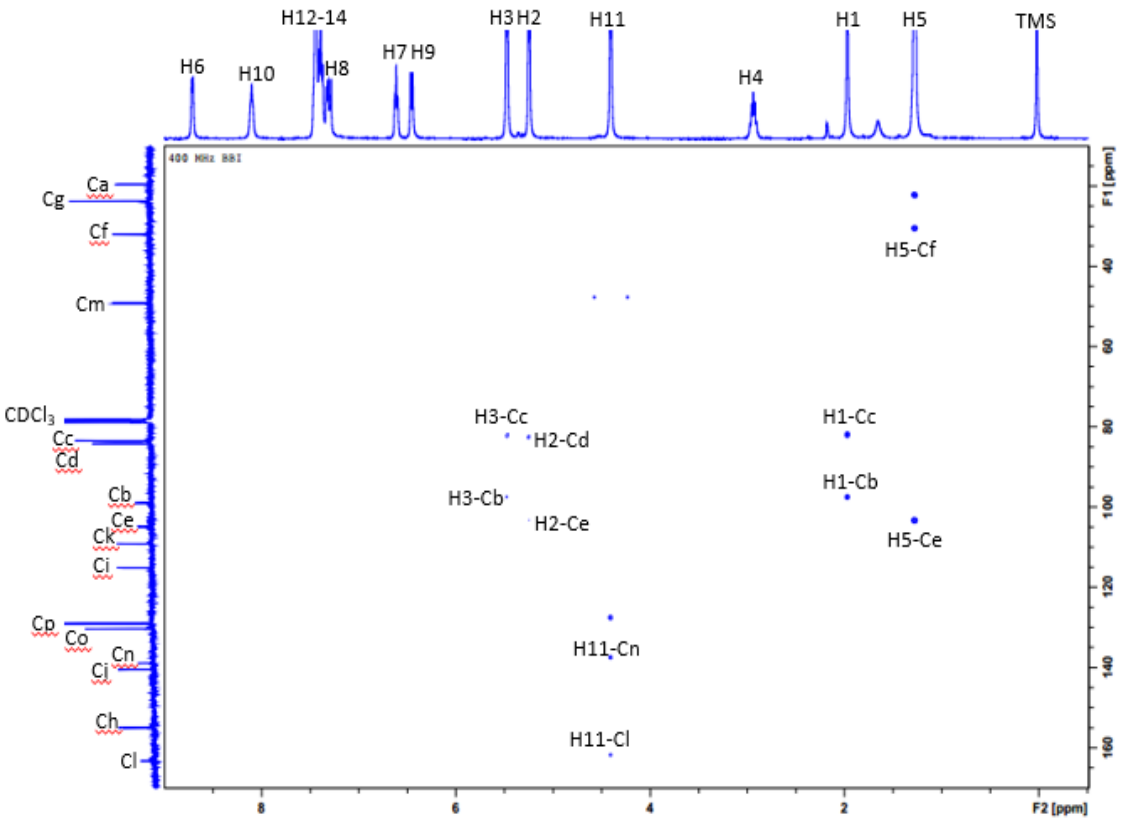

[(η^{6}-*p*-cimeno)RuCl$_2$(py)]

- $^{1}H–^{1}H$ gCOSY

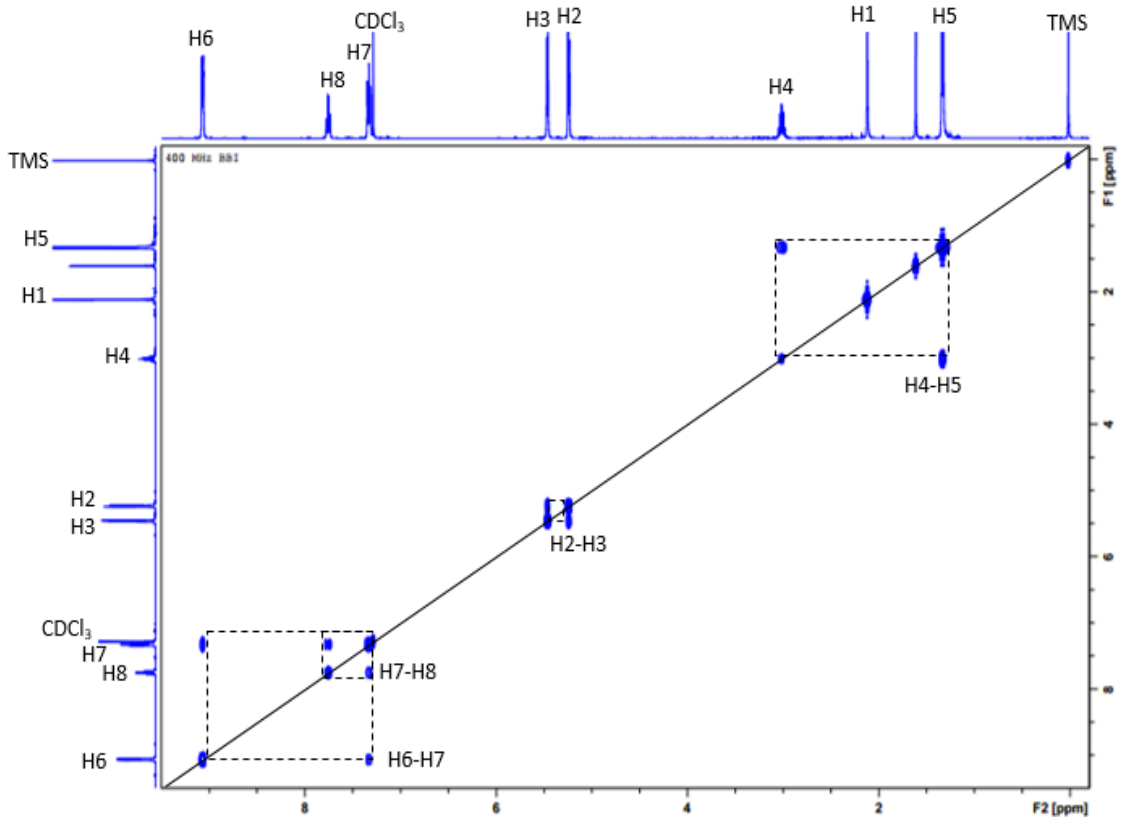

- $^{1}H–^{13}C$ gHSQC

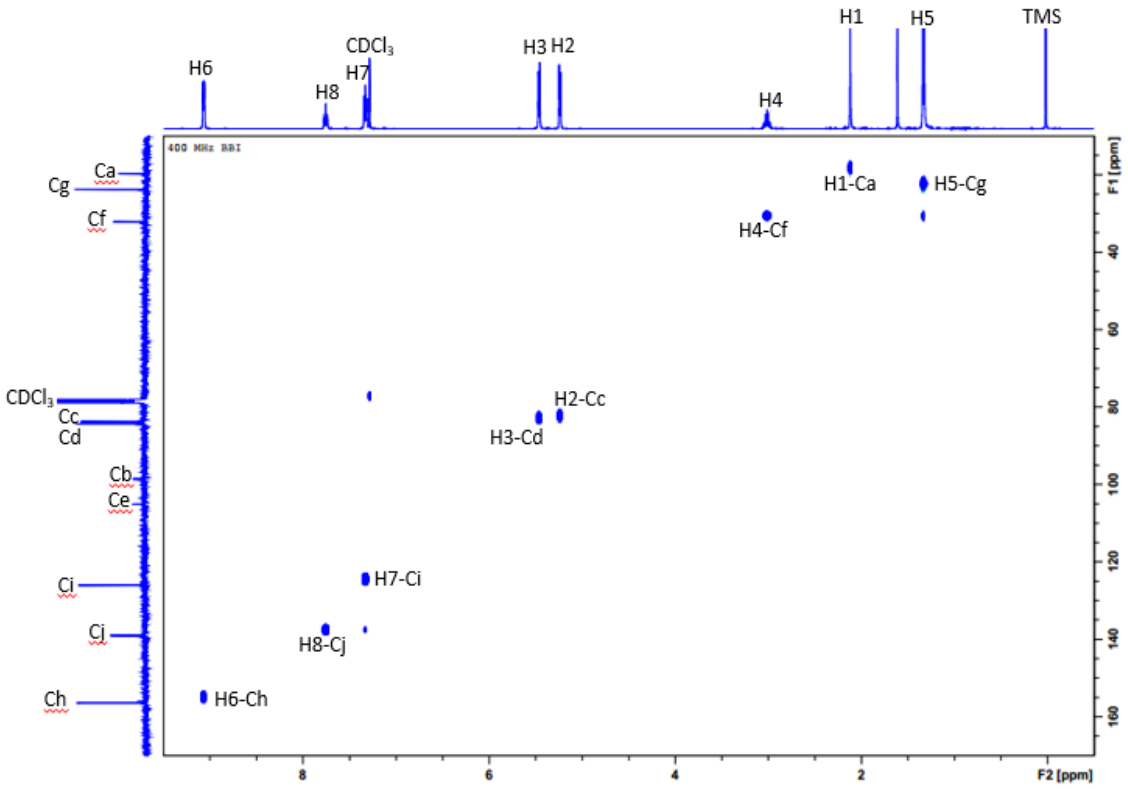

- $^{1}H–^{13}C$ gHMBC

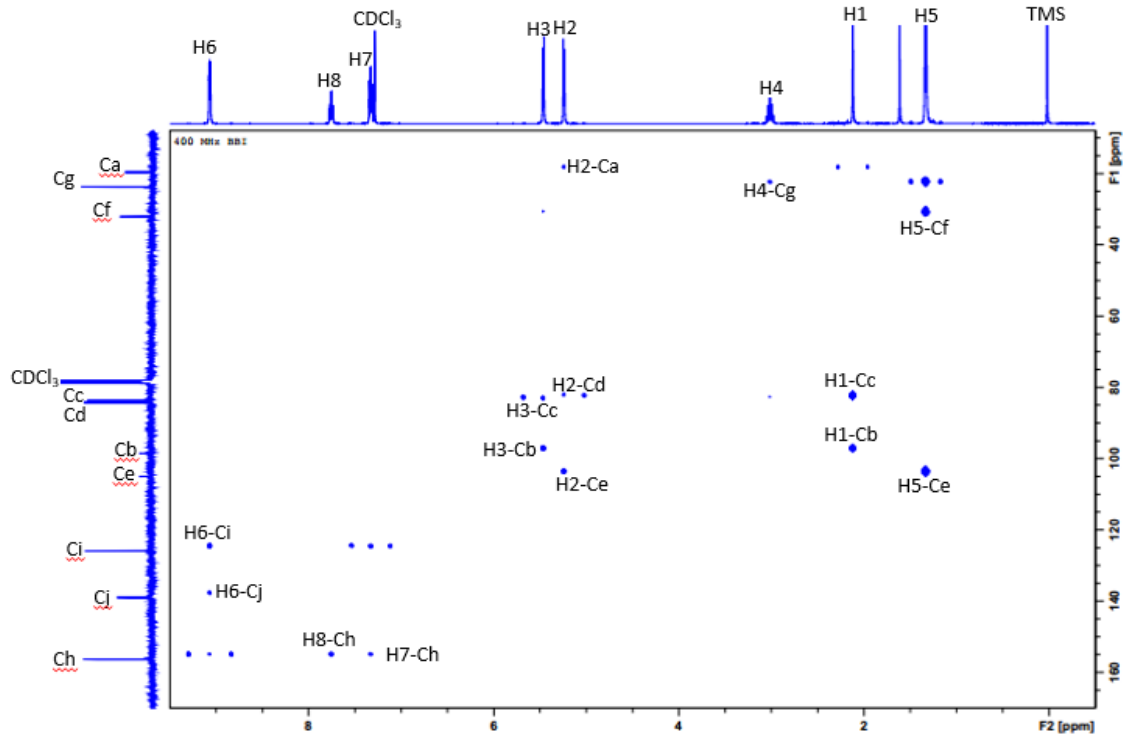

Figure S9 2D experiments such as Correlation Spectroscopy ($^{1}H–^{1}H$ gCOSY), Heteronuclear Single Quantum Coherence ($^{1}H–^{13}C$ gHSQC) and Heteronuclear Multiple Bond Coherence ($^{1}H–^{13}C$ gHMBC) of the series of complexes [(η^{6}-*p*-cimeno)$RuCl_2$(N)]

Computational study of model complexes **1** and **2**

Charge state – gas phase DFT geometries

-2

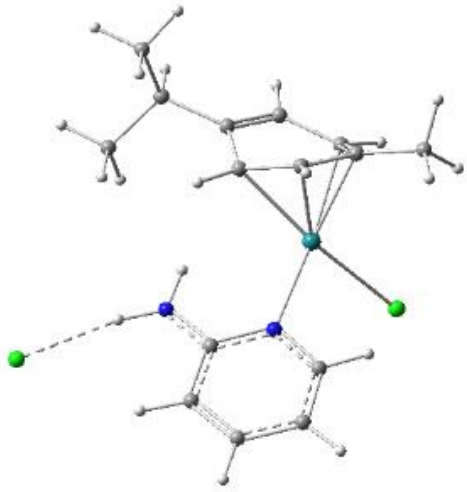

-1

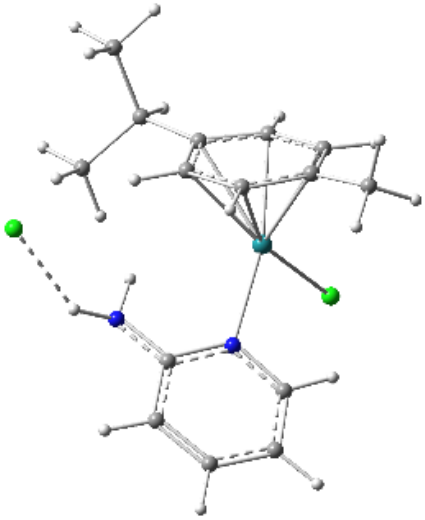

0

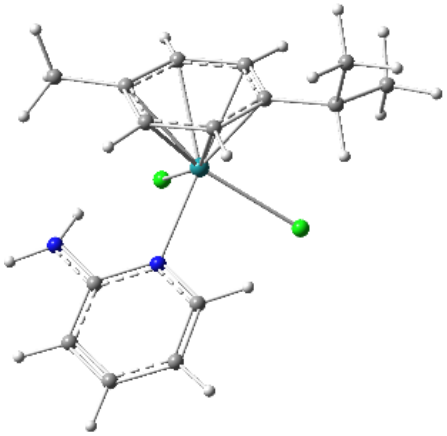

+1

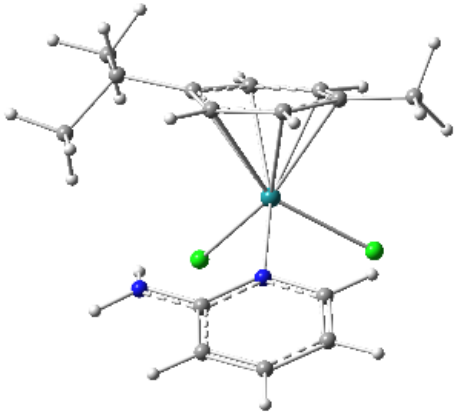

+2

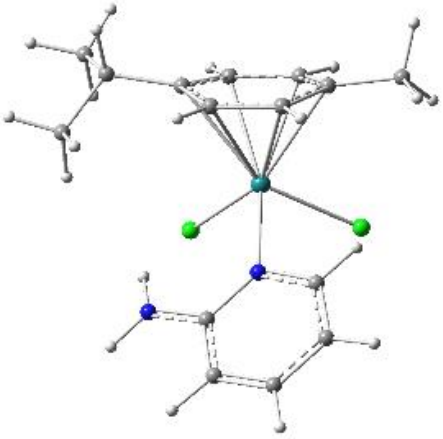

−2	−1	0	+1	+2
Centroid arene to Ru:				
1.791 (4 atoms)	1.813	1.766	1.937	1.950 Å
H-bonding to Cl:				
2.332, 3.341	*2.215, 3.112*	2.204, 3.152	2.281, 3.176	2.149, 3.048 Å

Figure S10 Results of the DFT calculations in the gas phase for neutral and charged forms of **1**

Table S6 Electronic absorption spectroscopic data and tentative assignments for complexes **1** – **4**.

Solvent		λ (nm)	E, ($mol^{-1}.L.cm^{-1}$)	Assignment
H_2O	**1**	229	12.200	$\pi\rightarrow\pi^*$ apy & *p*-cymene
		299	8.200	MLCT
		393	520	Ru(dπ)→Ru(dπ*)
	2	236	7.000	$\pi\rightarrow\pi^*$ meapy & *p*-cymene
		308	3.800	MLCT
		393	240	Ru(dπ)→Ru(dπ*)
	3	237	16.600	$\pi\rightarrow\pi^*$ bzapy & *p*-cymene
		309	8.800	MLCT
		405	840	Ru(dπ)→Ru(dπ*)
	4	256	10.200	$\pi\rightarrow\pi^*$ py & *p*-cymene
		394	800	Ru(dπ)→Ru(dπ*)
PBS buffer	**1**	227	13.800	$\pi\rightarrow\pi^*$ apy & *p*-cymene
		289	6.000	MLCT
		389	600	Ru(dπ)→Ru(dπ*)
	2	238	14.400	$\pi\rightarrow\pi^*$ meapy & *p*-cymene
		301	5.800	MLCT
		392	400	Ru(dπ)→Ru(dπ*)
	3	240	16.000	$\pi\rightarrow\pi^*$ bzapy & *p*-cymene
		300	5.600	MLCT
		403	600	Ru(dπ)→Ru(dπ*)
	4	256	5.400	$\pi\rightarrow\pi^*$ py & *p*-cymene
		394	500	Ru(dπ)→Ru(dπ*)
CH_3CN	**1**	233	9.200	$\pi\rightarrow\pi^*$ apy & *p*-cymene
		292	5.600	MLCT
		419	420	Ru(dπ)→Ru(dπ*)
	2	244	22.000	$\pi\rightarrow\pi^*$ meapy & *p*-cymene
		305	5.400	MLCT
		419	800	Ru(dπ)→Ru(dπ*)
	3	242	17.200	$\pi\rightarrow\pi^*$ bzapy & *p*-cymene
		305	4.400	MLCT
		420	600	Ru(dπ)→Benzapy(pπ*)
	4	244	28.200	$\pi\rightarrow\pi^*$ py & *p*-cymene
		408	720	Ru(dπ)→Ru(dπ*)

Cyclic Voltammetry

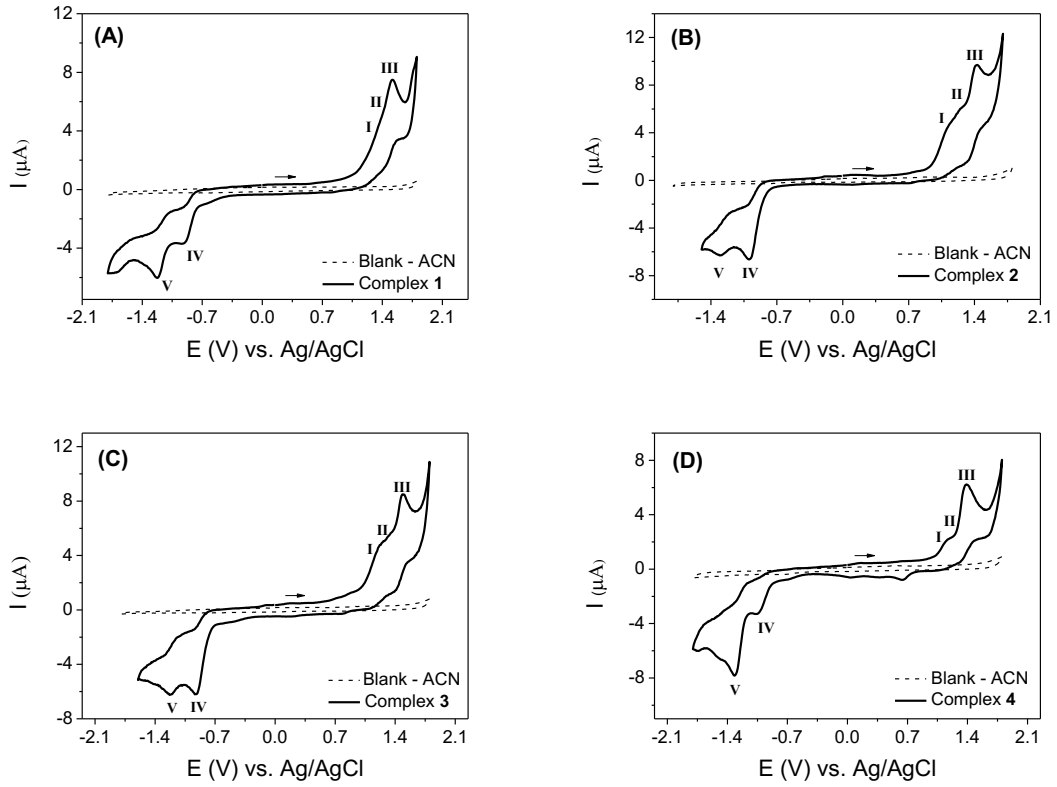

Figure S11 Cyclic voltammograms of the series of complexes [(η^6-*p*-cymene)$RuCl_2$(N)] at $2.0x10^{-3}$ mol·L^{-1} in PTBA/ACN 0.1 mol·L^{-1} *vs*. Ag/Ag^+; obtained at scan rate of 100 mV·s^{-1}. (A) complex **1**; (B) complex **2**; (C) complex **3**; (D) complex **4**.

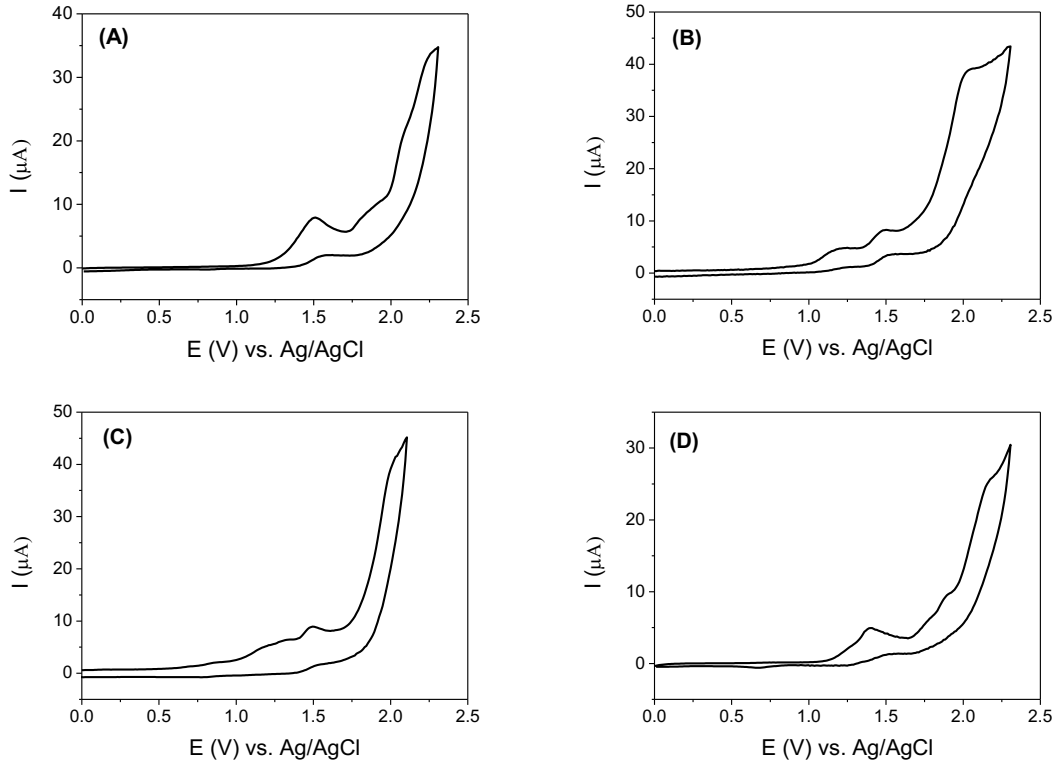

Figure S12 Cyclic voltammograms of **1** – **4** in the range 0 to +2.3 V. (A) complex **1**; (B) complex **2**; (C) complex **3**; (D) complex **4**; obtained at scan rate of 100 mV·s^{-1}.

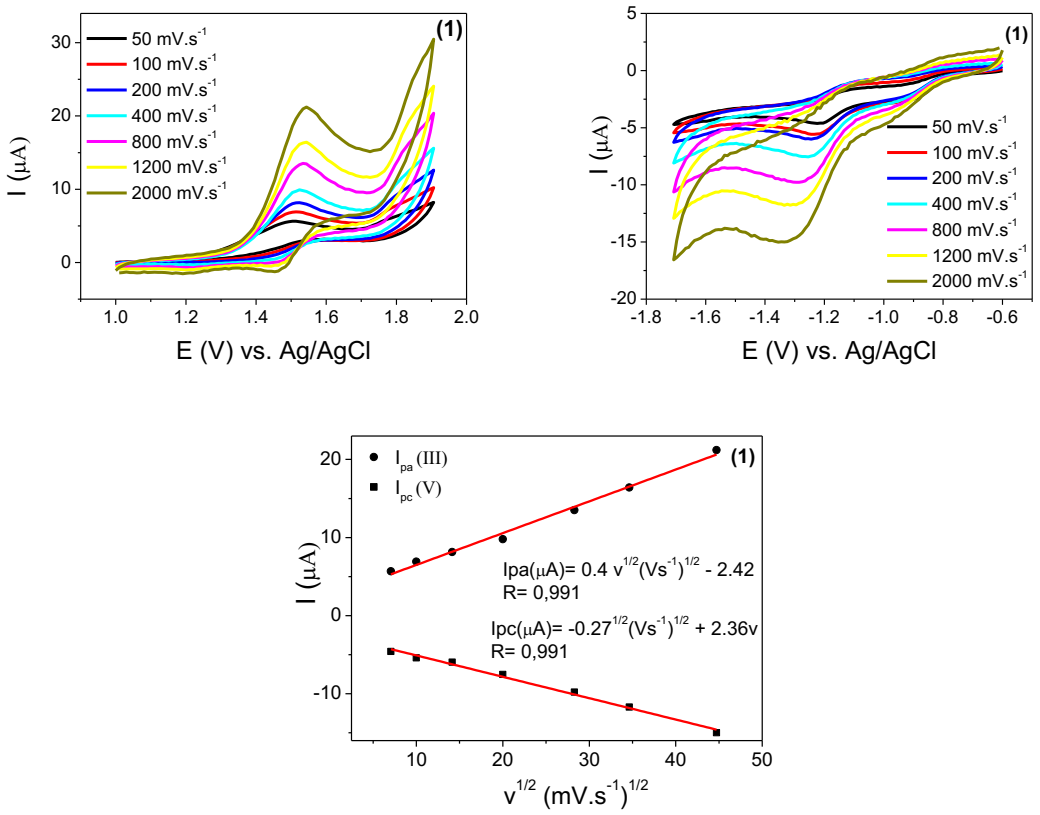

Figure S13 Cyclic voltammograms of complex **1** at 2.0x10^{-3} mol·L^{-1} in PTBA/ACN 0.1 mol·L^{-1} *vs.* Ag/Ag^{+}; obtained from 50 to 2000 mV.s^{-1} in anodic and cathodic regions. Plot of anodic currents (process III) and cathodic currents (process V) *vs.* square root of the scan rate ($v^{1/2}$).

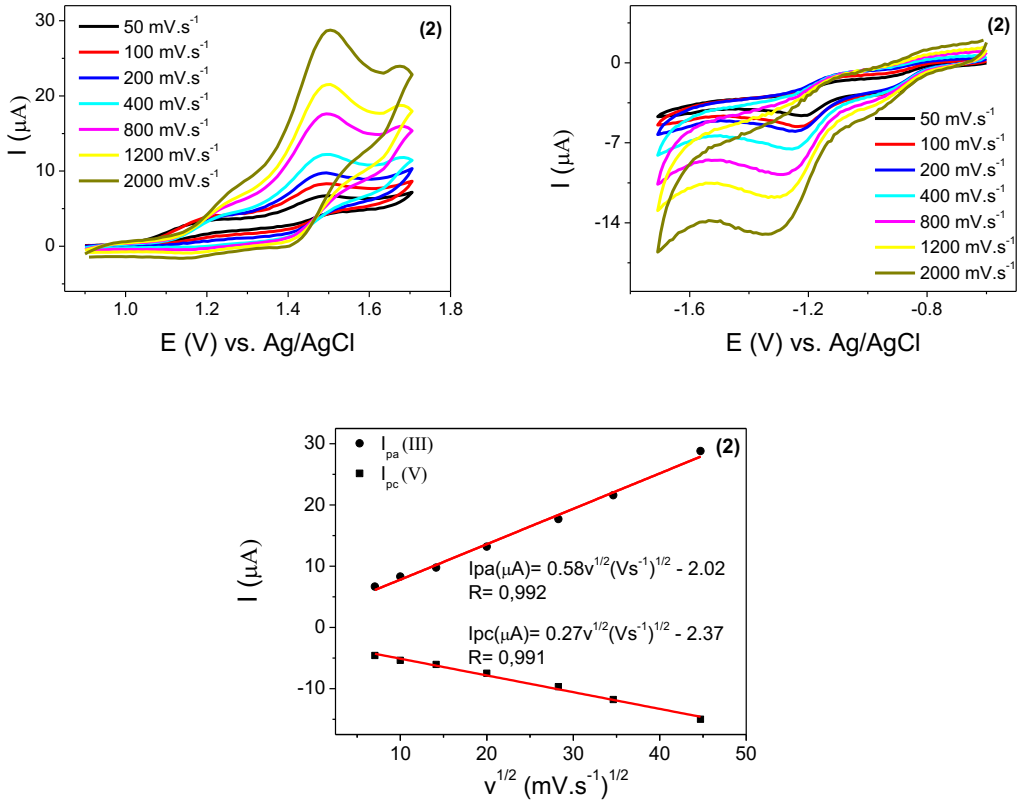

Figure S14 Cyclic voltammograms of complex **2** at 2.0x10^{-3} mol·L^{-1} in PTBA/ACN 0.1 mol·L^{-1} *vs.* Ag/Ag^{+}; obtained from 50 to 2000 mV.s^{-1} in anodic and cathodic regions. Plot of anodic currents (process III) and cathodic currents (process V) *vs.* square root of the scan rate ($v^{1/2}$).

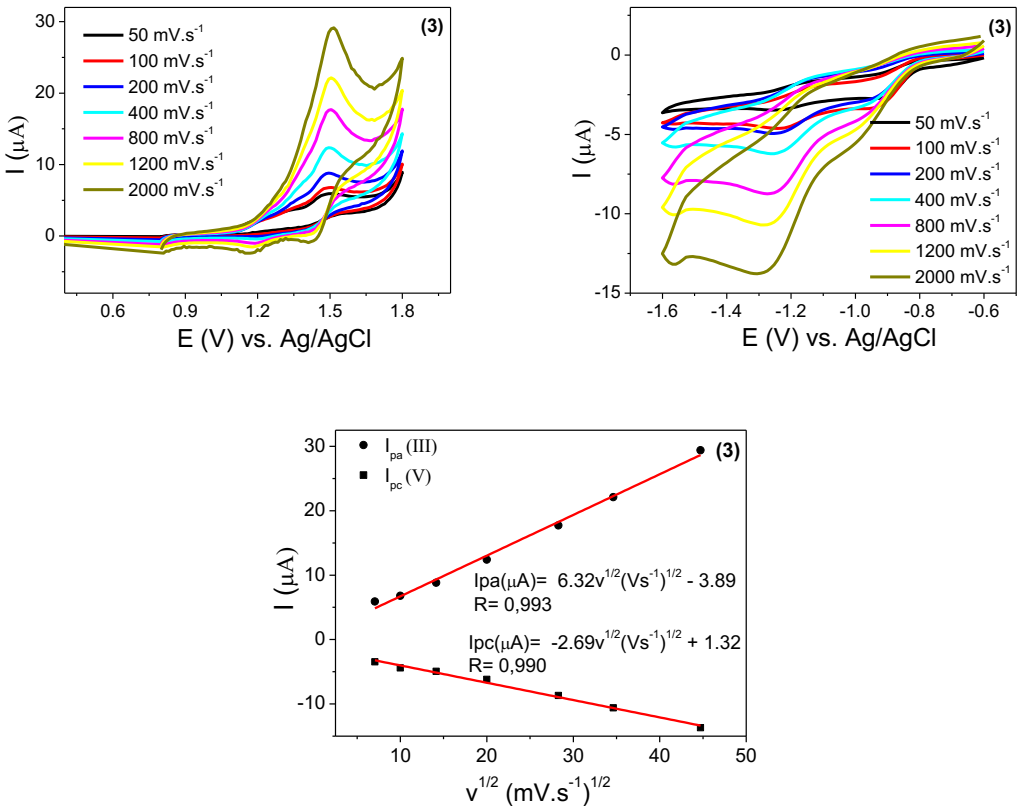

Figure S15 Cyclic voltammograms of complex **3** at 2.0x10^{-3} mol·L^{-1} in PTBA/ACN 0.1 mol·L^{-1} *vs*. Ag/Ag^{+}; obtained from 50 to 2000 mV.s^{-1} in anodic and cathodic regions. Plot of anodic currents (process III) and cathodic currents (process V) *vs*. square root of the scan rate ($v^{1/2}$).

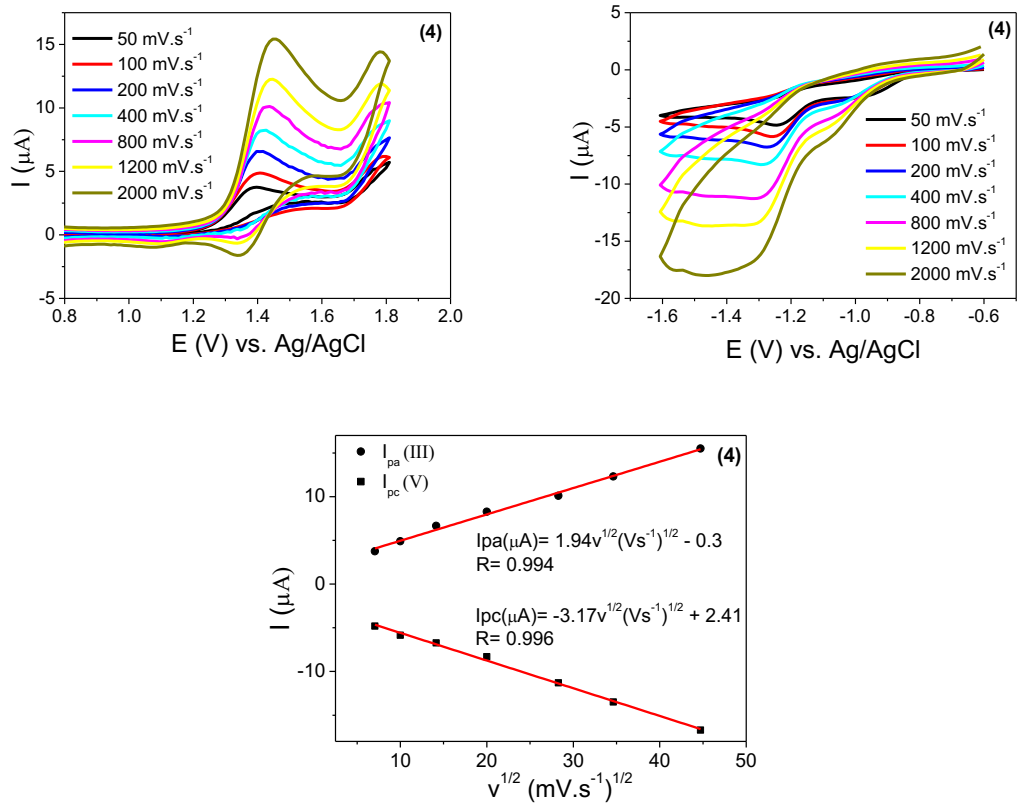

Figure S16 Cyclic voltammograms of complex **4** at 2.0x10^{-3} mol·L^{-1} in PTBA/ACN 0.1 mol·L^{-1} *vs*. Ag/Ag^{+}; obtained from 50 to 2000 mV.s^{-1} in anodic and cathodic regions. Plot of anodic currents (process III) and cathodic currents (process V) *vs*. square root of the scan rate ($v^{1/2}$).

Biological Tests

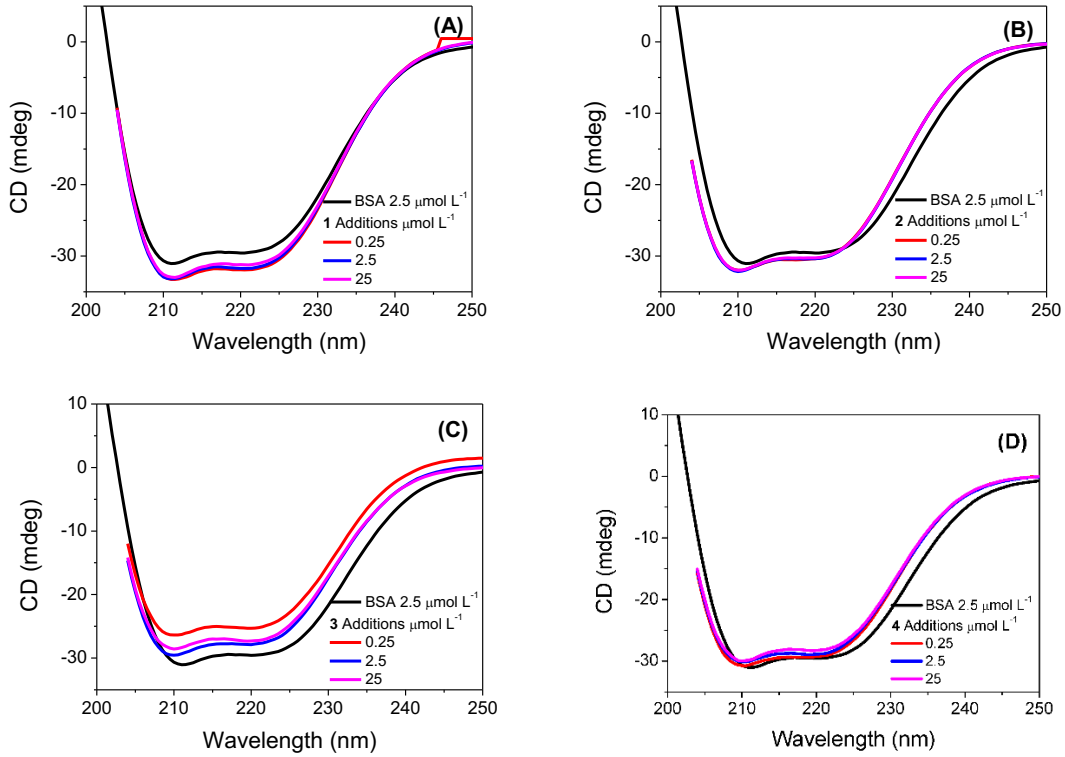

Figure S17 CD spectra for BSA (2.5 μmol·L^{-1}) in PBS buffer (pH 7.6) in the absence and after successive additions of complexes. (A) complex **1**; (B) complex **2**; (C) complex **3** and (D) complex **4**

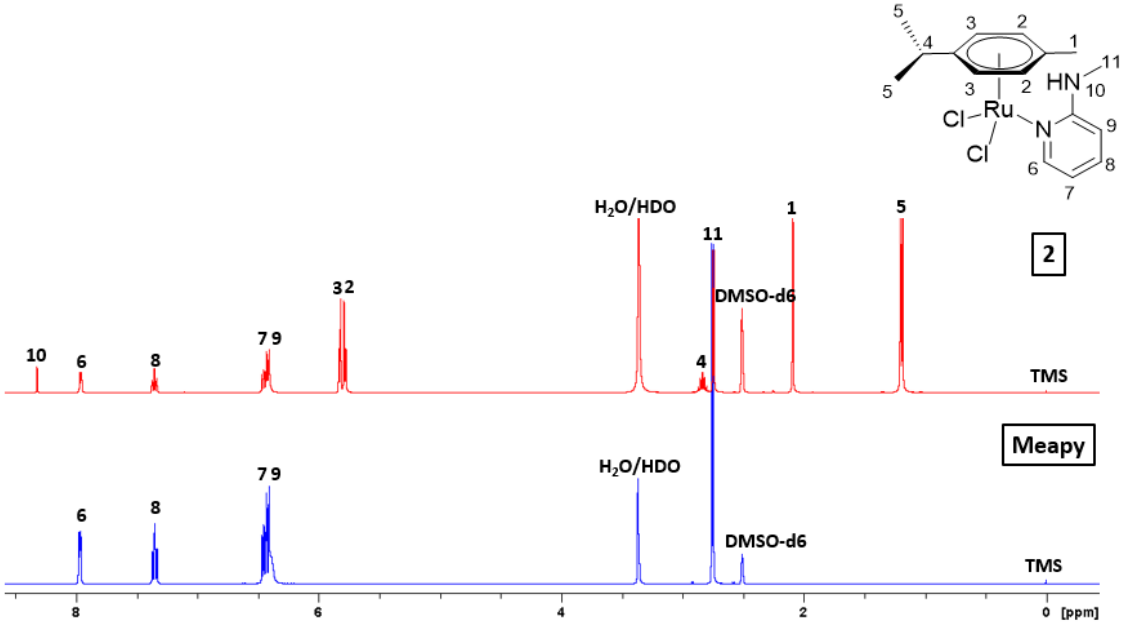

Figure S18 ^{1}H-NMR spectra in DMSO-d6 (400 MHz) of the complex 2 and meapy ligand.

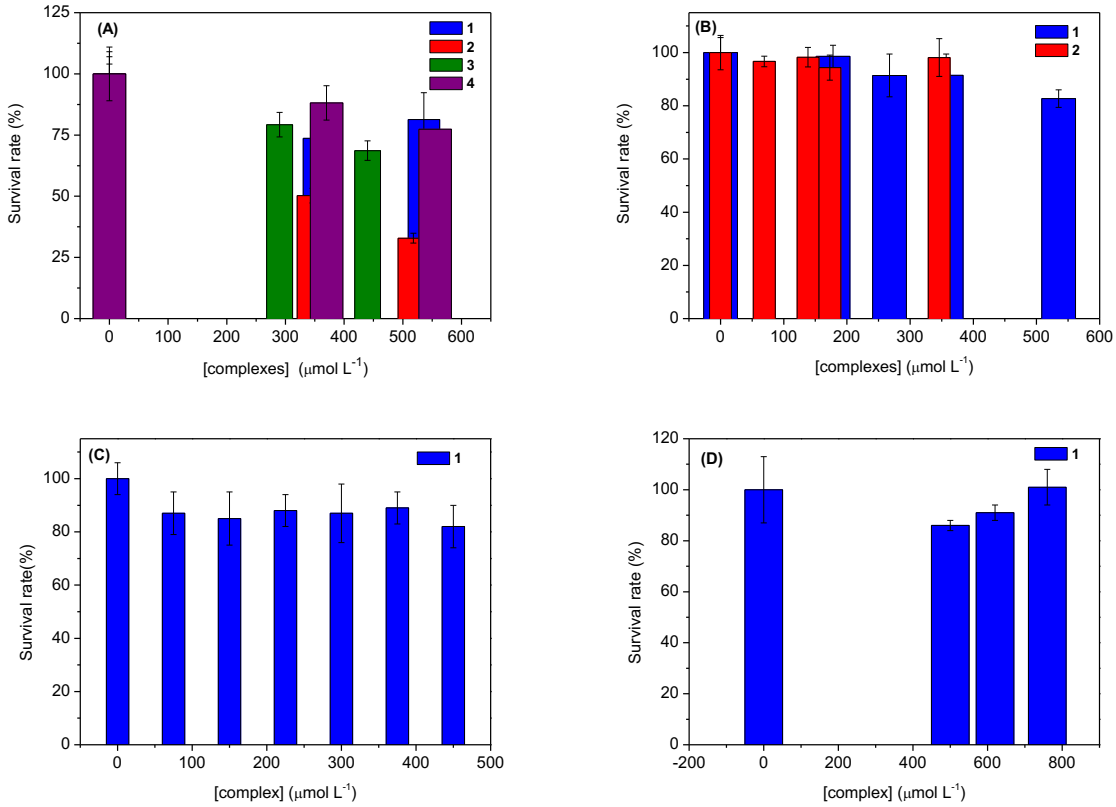

Figure S19 Survival rate of cells with the series of complexes [(η^6-*p*-cymene)$RuCl_2$(N)] with DMSO after 24 h incubation. (A): HeLa cells; (B): HEp-2 cells; (C) B16F10 cell; (D): Vero cells.

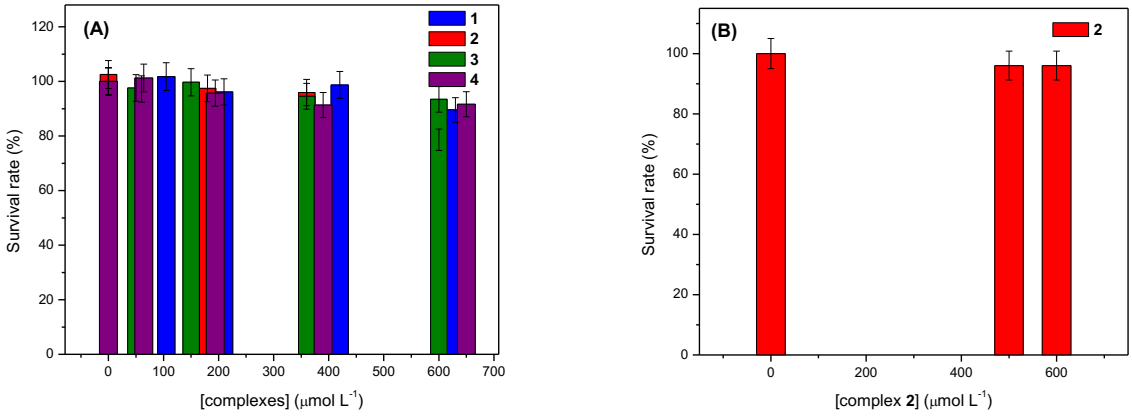

Figure S20 Survival rate of cells with the series of complexes [(η^6-*p*-cymene)$RuCl_2$(N)] after 24 h incubation. (A): HEp-2 cells; (B) B16F10 cell.

Comprehensive literature survey of cytotoxicity reported for Type A simple pyridine complexes.

A survey of cytotoxicity studies and other biological tests undertaken on Type A complexes employing relatively simple monodentate pyridine ligands was undertaken, using SciFinder to undertake a comprehensive listing of structures and citations in the Chemical Abstracts Database. Results are listed in the Tables below.

Complex	Structure	CAS Number	Method	Cell Lines	IC_{50}	DNA Interaction	Method	Reference
$C_{19}H_{27}Cl_2NRu$	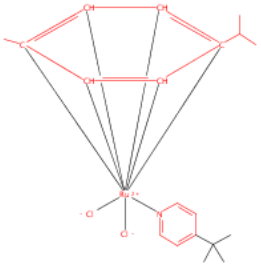	2104688-39-1	MTT assay	MCF-7 HCC1937	(48 h) µM 642.6 ± 6.6 385.1 ± 5.3	X	X	Chucklin, 2017 [8]
$C_{80}H_{108}Cl_8N_{10}Ru_4$		1192578-20-3	MTT assay	A2780	(24 h) µM 43 ± 5	X	X	Govender, 2009 [9]
$C_{19}H_{26}Cl_2N_2Ru$	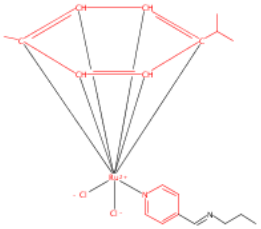	1192578-30-5	MTT assay	A2780	(24 h) µM 98 ± 5	X	X	Govender, 2009 [9]
$C_{21}H_{30}Cl_2N_2Ru$	[(hexamethylbenzene) RuCl2(L)]		MTT assay	A2780	(24 h) µM 94 ± 5	X	X	Govender, 2009 [9]
$C_{16}H_{21}Cl_2NRu$	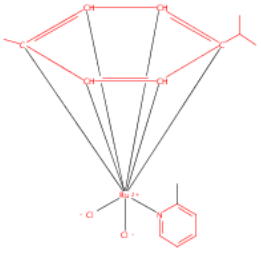	1372709-47-1	MTT assay	LoVo MiaPaca	(24 h) µM 78 288	Covalent binding mode	Electrophoretical mobility Atomic force microscopy Circular dichroism Viscosity measurements Fluorescence studies	Grau, 2012 [6]

$C_{16}H_{21}Cl_2NRu$	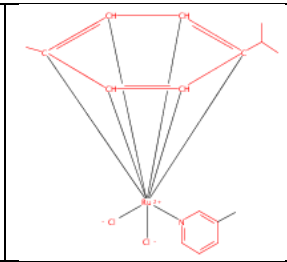	1372709-48-2	MTT assay	LoVo MiaPaca	(24 h) µM 90 155	Covalent binding mode	Electrophoretical mobility Atomic force microscopy Circular dichroism Viscosity measurements Fluorescence studies	Grau, 2012 [6]
$C_{16}H_{21}Cl_2NRu$	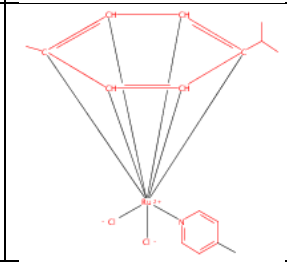	1372709-49-3	MTT assay	LoVo MiaPaca	(24 h) µM >50 240	Covalent binding mode	Electrophoretical mobility Atomic force microscopy Circular dichroism Viscosity measurements Fluorescence studies	Grau, 2012 [6] Patra, 2013 [11]
$C_{17}H_{21}Cl_2NRu$	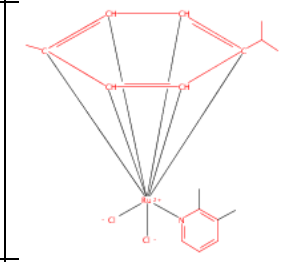	1372709-50-6	X	X	X	Covalent binding mode	Electrophoretical mobility Atomic force microscopy Circular dichroism Viscosity measurements Fluorescence studies	Grau, 2012 [6] Patra, 2013 [11]
$C_{17}H_{21}Cl_2NRu$	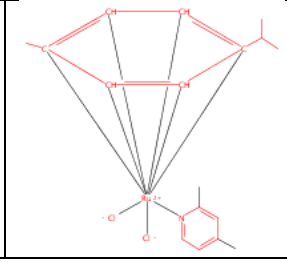	1372709-51-7	X	X	X	Covalent binding mode	Electrophoretical mobility Atomic force microscopy Circular dichroism Viscosity measurements Fluorescence studies	Grau, 2012 [6] Patra, 2013 [11]

$C_{17}H_{21}Cl_2NRu$	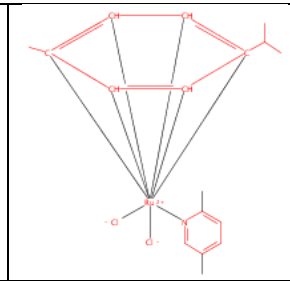	1372709-53-9	X	X	X	Covalent binding mode	Electrophoretical mobility Atomic force microscopy Circular dichroism Viscosity measurements Fluorescence studies	Grau, 2012 [6] Patra, 2013 [11]
$C_{17}H_{21}Cl_2NRu$	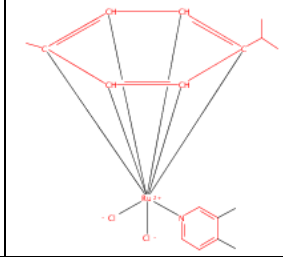	1372709-54-0	X	X	X	Covalent binding mode	Electrophoretical mobility Atomic force microscopy Circular dichroism Viscosity measurements Fluorescence studies	Grau, 2012 [6]
$C_{17}H_{21}Cl_2NRu$	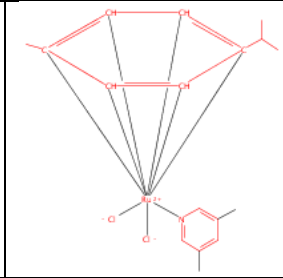	1372709-55-1	X	X	X	Covalent binding mode	Electrophoretical mobility Atomic force microscopy Circular dichroism Viscosity measurements Fluorescence studies	Grau, 2012 [6]
$C_{17}H_{21}Cl_2NRu$	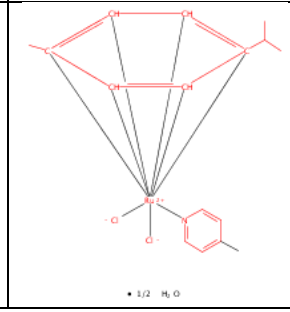	1372709-62-0	X	X	X	Covalent binding mode	Electrophoretical mobility Atomic force microscopy Circular dichroism Viscosity measurements Fluorescence studies	Grau, 2012 [6]

$C_{17}H_{21}Cl_2NORu$	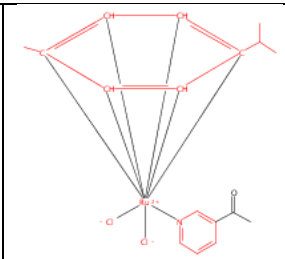	1221293-18-0	MTT assay	HeLa B16 FemX MDA-MB-361 MDA-MB-453 LS-174	(48 h/ 72 h) µM 275.71± 1.57 / 244.00± 1.91 n.d. / >300 >300 / 220.50± 6.36 >300 / 290.02± 6.65 >300 / >300 n.d. / >300	X	X	Grguric-Sipka, 2010 [10] Shweshein, 2014 [12]
$C_{17}H_{21}Cl_2NORu$	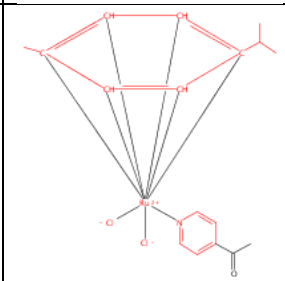	1221293-19-1	MTT assay	HeLa B16 FemX MDA-MB-361 MDA-MB-453 LS-174	(48 h/ 72 h) µM >300 / 295.75± 2.95 n.d. / >300 >300 / >300 >300 / >300 >300 / >300 n.d. / >300	X	X	Grguric-Sipka, 2010 [10] Shweshein, 2014 [12]
$C_{15}H_{19}Cl_3N_2Ru$	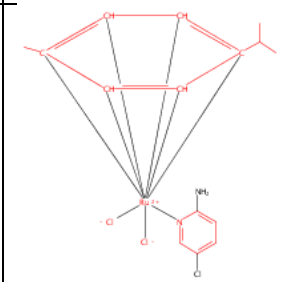	1221293-20-4	MTT assay	HeLa B16 FemX MDA-MB-361 MDA-MB-453 LS-174	(48 h/ 72 h) µM >300 / 283.20±3.12 n.d. / >300 >300 / >300 >300 / >300 >300 / >300 n.d. / >300	X	X	Grguric-Sipka, 2010 [10] Shweshein, 2014 [12] Gligorijevic, 2012 [13]
[(*p*-cymene)$RuCl_2$(5-fluorouracil-1-methyl isonicotinate)]			SRB assay MTT assay	BEL-7402 HL-60	µM 8.1 >200	X	X	Liu, 2012 [14]
[(*p*-cymene)Ru Cl_2(isonicotinamide)]	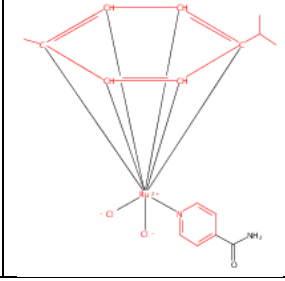	336876-10-9						Morris, 2001 [15] Aird, 2002 [16]

$C_{17}H_{23}Cl_2NORu$	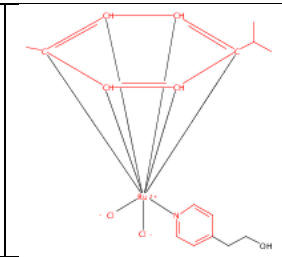	1616929-66-8	MTT assay	HL-60	(24 h) μM 202	Covalent binding mode	Electrophoretical mobility Atomic force microscopy Circular dichroism Viscosity measurements Fluorescence studies	Sáez, 2014 [17]
$C_{15}H_{19}Cl_2FN_2Ru$	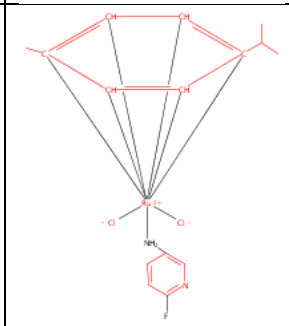	1607854-41-0	SRB assay MTT assay	A549 MCF-7	μM 46.1±1.5 61.5±1.0	Minor groove binding mode	UV–vis absorption titrations Fluorescence studies	Yan, 2018 [18]
$C_{15}H_{19}Cl_3N_2Ru$	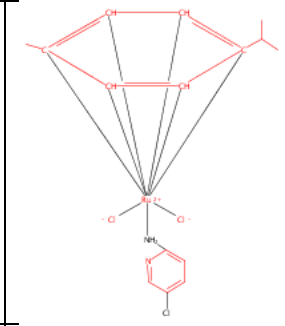	1607854-40-9	SRB assay MTT assay	A549 MCF-7	μM 8.2±1.0 47.4±1.1	Minor groove binding mode	UV–vis absorption titrations Fluorescence studies	Yan, 2018 [18]
$C_{15}H_{19}Cl_2BrN_2Ru$	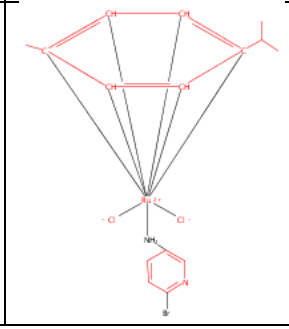	1607854-42-1	SRB assay MTT assay	A549 MCF-7	μM 72.7±0.8 >80±2.0	Minor groove binding mode	UV–vis absorption titrations Fluorescence studies	Yan, 2018 [18]

$C_{16}H_{20}Cl_2N_2O_3Ru$	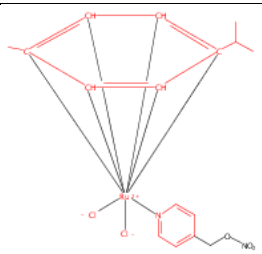	2073786-94-2	Fluorescent assay	A549	µM 180	X	X	Zhao, 2016 [19]
$C_{15}H_{19}Cl_2NRu$	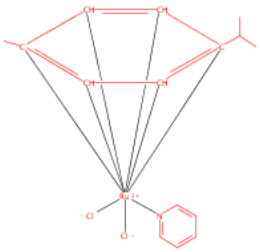	52490-96-7	MThhT assay	COLO205 HCT116 SW620	70 h) µM >100 3.4 (2.2–5.1) 4.1 (2.3–5.5)	X	X	Babak, 2015 [20]
	Same		MTT assay	TS/A HBL-100	(72 h) µM 757 522	X	X	Vock, 2006 [21]
	Same			A549	> 500	X	X	Zhao, 2016 [19]
	Same			A549 HCT-116 HepG2	> 500 > 500 * > 500	X	X	Zhao, 2018 [22]

* Note that this report contradicts the previous study by Babak et. al. 2015

Archival geometries from the DFT Structure optimizations

UB3LYP//6-31G*(d),SPK-DZCD hybrid DFT calculations were performed. The final geometries for the computed structures are shown below.

Complex **1** in the gas phase (singlet electronic state)

Tag	Symbol	NA	NB	NC	Bond	Angle	Dihedral	X	Y	Z
1	C							-1.17969	-0.33569	-1.64004
2	C	1			1.423303			-2.21456	-0.16608	-0.67772
3	C	2	1		1.435378	117.8759		-2.27866	1.083459	0.025736
4	C	3	2	1	1.417676	120.5347	2.189278	-1.36398	2.125034	-0.27138
5	C	4	3	2	1.434149	122.2412	1.059707	-0.36002	1.994968	-1.28723
6	C	5	4	3	1.422582	116.5274	-4.48097	-0.2595	0.726038	-1.9224
7	H	3	2	1	1.080586	120.1447	-174.341	-2.99054	1.219044	0.827304
8	H	6	5	4	1.085233	119.0224	-173.93	0.549049	0.551478	-2.6249
9	Ru	4	3	2	2.236065	72.78332	-56.3761	-0.15934	0.322382	0.275683
10	Cl	9	4	3	2.460359	128.6316	-37.2853	-0.63318	-1.38008	1.987543
11	Cl	9	4	3	2.494901	85.89516	-121.91	0.828674	1.748316	2.068744
12	C	9	4	3	3.186697	126.5914	164.7816	2.951423	-0.11716	-0.25815
13	C	12	9	4	2.351654	64.80147	-152.769	1.667627	-2.08409	-0.1428
14	C	12	9	4	1.418217	153.6416	-136.461	4.076187	-0.88177	-0.66016
15	C	13	12	9	1.38592	92.48102	172.9384	2.736724	-2.87634	-0.53031
16	H	13	12	9	1.080215	145.7152	-11.6689	0.710541	-2.51117	0.118846
17	C	14	12	9	1.383796	120.0717	-14.405	3.96676	-2.25383	-0.80287
18	H	14	12	9	1.084533	118.7515	166.5747	5.017588	-0.37252	-0.8352
19	H	15	13	12	1.082542	119.8976	178.7804	2.614154	-3.94935	-0.60461
20	H	17	14	12	1.084922	120.1051	-179.686	4.82817	-2.8399	-1.10544
21	N	13	12	9	1.36527	30.78613	-4.81789	1.745089	-0.72573	-0.02964
22	N	12	9	4	1.365091	84.91432	31.02621	3.043283	1.237377	-0.11578
23	H	22	12	9	1.020534	117.8601	28.80959	2.362137	1.700899	0.486444
24	H	22	12	9	1.007938	118.3891	-179.897	3.949611	1.6686	-0.20827
25	H	1	2	3	1.084216	119.6765	176.344	-1.06741	-1.28837	-2.14533
26	H	4	3	2	1.08385	118.9107	-175.174	-1.38445	3.027374	0.328694
27	C	5	4	3	1.505949	121.1044	177.0394	0.555832	3.141067	-1.62716
28	H	27	5	4	1.093248	111.2061	153.0252	1.507798	2.78146	-2.0267
29	H	27	5	4	1.098396	110.5211	-86.6653	0.091925	3.795057	-2.37787
30	H	27	5	4	1.094383	110.7563	32.78043	0.76604	3.745934	-0.73968
31	C	2	1	6	1.525774	119.4648	178.4998	-3.1988	-1.30435	-0.42551
32	H	31	2	1	1.098357	106.628	48.37952	-2.59895	-2.21463	-0.29149
33	C	31	2	1	1.551468	109.3118	-68.4282	-4.09604	-1.49357	-1.67699
34	H	33	31	2	1.09564	112.0478	56.96184	-3.50662	-1.68534	-2.58045
35	H	33	31	2	1.095474	109.7821	177.0284	-4.77028	-2.34345	-1.52474
36	H	33	31	2	1.096912	110.8423	-63.8123	-4.71043	-0.60249	-1.85506
37	C	31	2	1	1.538564	114.2791	167.0294	-4.06066	-1.12746	0.836663
38	H	37	31	2	1.095383	109.4029	-175.985	-4.68336	-2.0172	0.979741
39	H	37	31	2	1.093145	111.0465	-56.8614	-3.43545	-1.00612	1.725118
40	H	37	31	2	1.097756	111.5607	65.42955	-4.73624	-0.26692	0.7465

Complex $\mathbf{1}^{+}$ in the gas phase (doublet electronic state)

Tag	Symbol	NA	NB	NC	Bond	Angle	Dihedral	X	Y	Z
1	C							2.363276	1.009109	-0.089828
2	C	1			1.4313705			2.198324	-0.152598	-0.909614
3	C	2	1		1.4200711	116.23081		1.059946	-0.165302	-1.758458
4	C	3	2	1	1.4317499	121.56215	10.640077	0.260178	1.005511	-1.957143
5	C	4	3	2	1.4100713	121.65427	-3.7982322	0.516889	2.204069	-1.260107
6	C	1	2	3	1.4161132	121.44192	-7.857584	1.535177	2.147173	-0.246158
7	H	3	2	1	1.0834611	119.73183	-174.51621	0.83069	-1.052441	-2.336657
8	H	6	1	2	1.0843887	119.3374	179.83334	1.688384	3.007884	0.395405
9	Ru	6	1	2	2.3073189	74.499664	62.298516	0.117866	0.432852	0.367074
10	Cl	9	6	1	2.3662447	87.383362	137.28147	-0.946551	1.975093	1.811935
11	Cl	9	6	1	2.368391	121.59952	46.581311	0.633201	-1.02039	2.164793
12	C	9	6	1	3.1409819	154.1594	-99.612989	-1.980602	-1.836662	-0.191053
13	C	12	9	6	2.3632742	64.541308	-78.071596	-2.840948	0.364444	-0.189582
14	C	12	9	6	1.4192132	153.32783	-64.9481	-3.248929	-2.315992	-0.610285
15	C	13	12	9	1.3798272	92.358188	174.20074	-4.088789	-0.06207	-0.595663
16	H	13	12	9	1.0783315	146.39226	-9.4019524	-2.647948	1.403992	0.02229
17	C	14	12	9	1.3803558	120.40197	-11.613474	-4.294139	-1.438265	-0.816473
18	H	14	12	9	1.083836	118.45913	169.28473	-3.377776	-3.383202	-0.748711
19	H	15	13	12	1.0821065	119.74137	178.76871	-4.887067	0.657408	-0.722384
20	H	17	14	12	1.0838933	120.21631	-179.51972	-5.263699	-1.808422	-1.129142
21	N	12	9	6	1.3744919	33.931055	-81.899099	-1.780203	-0.490004	-0.002425
22	N	12	9	6	1.3621524	86.139208	103.98986	-0.948642	-2.707733	-0.012859
23	H	22	12	9	1.0115556	119.86889	27.654866	-0.171378	-2.452942	0.582277
24	H	22	12	9	1.0087045	118.63649	-176.72235	-1.118504	-3.692713	-0.148675
25	H	1	6	5	1.0818506	118.81543	177.53772	3.141761	1.029881	0.661125
26	H	4	3	2	1.0848584	118.85519	175.97359	-0.560381	0.965	-2.665634
27	C	5	4	3	1.5023388	122.79201	176.8312	-0.261181	3.466843	-1.498918
28	H	27	5	4	1.094874	111.00499	130.17163	-0.613204	3.895382	-0.554893
29	H	27	5	4	1.0974948	109.80929	-111.0591	0.38149	4.213987	-1.981872
30	H	27	5	4	1.0926881	111.76	8.5416113	-1.1219	3.295331	-2.149851
31	C	2	1	6	1.5277605	122.43138	170.69026	3.200188	-1.305991	-0.907305
32	H	31	2	1	1.1039712	103.6626	-115.50448	3.613062	-1.294809	-1.931103
33	C	31	2	1	1.5480726	113.84039	128.72784	2.55295	-2.696588	-0.697897
34	H	33	31	2	1.0940983	112.80616	50.26958	1.708912	-2.877103	-1.370255
35	H	33	31	2	1.093753	109.12857	169.90612	3.300509	-3.472109	-0.887682
36	H	33	31	2	1.0942547	110.18006	-71.657005	2.211071	-2.801972	0.336224
37	C	31	2	1	1.5401145	113.81053	0.9820428	4.374886	-1.107244	0.068675
38	H	37	31	2	1.0937328	109.21439	-175.53109	5.08302	-1.932647	-0.047547
39	H	37	31	2	1.0955023	112.43284	-56.796378	4.926156	-0.180347	-0.123909
40	H	37	31	2	1.0961488	111.51401	65.918317	4.036232	-1.110027	1.111195

Complex $\mathbf{1}^{2+}$ in the gas phase (triplet electronic state)

Tag	Symbol	NA	NB	NC	Bond	Angle	Dihedral	X	Y	Z
1	C							2.47504	0.688507	0.161987
2	C	1			1.4415074			2.238872	-0.289649	-0.870185
3	C	2	1		1.4178344	115.65648		1.201431	0.021602	-1.785113
4	C	3	2	1	1.4343587	121.77768	10.347568	0.589738	1.318497	-1.820889
5	C	4	3	2	1.4157237	121.6601	-0.3542041	0.986626	2.351885	-0.938357
6	C	1	2	3	1.4137592	121.84137	-10.424225	1.874829	1.968089	0.128346
7	H	3	2	1	1.0842368	119.78247	-174.51399	0.906949	-0.705831	-2.533238
8	H	6	1	2	1.0852174	119.26408	-178.16358	2.105297	2.682909	0.911681
9	Ru	6	1	2	2.3412795	72.842996	64.19477	0.148744	0.401031	0.344099
10	Cl	9	6	1	2.3330689	88.376598	144.32764	-0.979483	1.929034	1.698913
11	Cl	9	6	1	2.3584071	112.76221	49.016769	0.550318	-1.168655	2.05784
12	C	9	6	1	3.2345974	166.84616	-96.302815	-2.279331	-1.690678	-0.09388
13	C	12	9	6	2.3447968	62.375692	-65.589744	-2.688323	0.56678	-0.578319
14	C	12	9	6	1.4349234	152.66271	-65.081104	-3.623004	-2.022821	-0.472336
15	C	13	12	9	1.4049173	91.642318	-179.61552	-4.016123	0.289524	-0.9442
16	H	13	12	9	1.0788082	148.69707	-2.2769217	-2.330105	1.584112	-0.601612
17	C	14	12	9	1.3808066	120.19498	-0.9164077	-4.490018	-1.034548	-0.894509
18	H	14	12	9	1.0844856	118.51843	179.45969	-3.93671	-3.059198	-0.412167
19	H	15	13	12	1.0833546	119.03283	178.58167	-4.659441	1.106674	-1.247622
20	H	17	14	12	1.0833678	120.81061	-179.2648	-5.510077	-1.272375	-1.171283
21	N	13	12	9	1.3561721	32.183667	0.814774	-1.807194	-0.376524	-0.162396
22	N	12	9	6	1.3365967	88.363156	114.92614	-1.466409	-2.663797	0.328835
23	H	22	12	9	1.0221577	121.2835	8.9643395	-0.55187	-2.452948	0.733764
24	H	22	12	9	1.0155521	120.40592	178.12532	-1.804668	-3.61811	0.407661
25	H	1	6	5	1.0827994	118.67051	178.87415	3.15034	0.452669	0.974886
26	H	4	3	2	1.0853529	118.73608	175.41124	-0.146933	1.526937	-2.590213
27	C	5	4	3	1.497254	122.83284	172.68545	0.482786	3.757001	-1.054821
28	H	27	5	4	1.0943956	111.91538	134.89025	0.190583	4.167984	-0.083527
29	H	27	5	4	1.0998883	108.7939	-107.19751	1.292865	4.393068	-1.440755
30	H	27	5	4	1.0922516	112.36308	11.58102	-0.356963	3.841243	-1.748174
31	C	2	1	6	1.524144	122.5671	168.95755	3.055143	-1.571372	-0.988095
32	H	31	2	1	1.1054954	103.18945	-113.64783	3.601664	-1.435752	-1.939432
33	C	31	2	1	1.5497984	113.67895	131.34461	2.190535	-2.846985	-1.152836
34	H	33	31	2	1.0951207	113.15839	52.244046	1.461257	-2.770887	-1.966256
35	H	33	31	2	1.0930575	109.0482	171.30045	2.843034	-3.692715	-1.384699
36	H	33	31	2	1.0955162	110.43878	-70.808984	1.669994	-3.07976	-0.217417
37	C	31	2	1	1.5398948	114.11753	2.669216	4.10262	-1.75496	0.125621
38	H	37	31	2	1.0932101	109.09665	-175.21584	4.694756	-2.64963	-0.084257
39	H	37	31	2	1.0950925	112.4418	-57.000513	4.80564	-0.917121	0.180542
40	H	37	31	2	1.0962527	111.92461	66.198698	3.635766	-1.896048	1.107411

Complex **1**$^{-}$ in the gas phase (doublet electronic state)

Tag	Symbol	NA	NB	NC	Bond	Angle	Dihedral	X	Y	Z
1	C							1.77994	-2.021933	-0.020164
2	C	1			1.4283419			2.146003	-0.641656	-0.05169
3	C	2	1		1.4230057	116.96944		1.483307	0.222839	0.863967
4	C	3	2	1	1.4324529	120.852	4.2311084	0.562586	-0.297247	1.830251
5	C	4	3	2	1.4265043	122.17924	1.8820384	0.295272	-1.693325	1.950351
6	C	5	4	3	1.4267128	116.48457	-6.1940594	0.887959	-2.541434	0.968036
7	H	3	2	1	1.090005	121.06962	-176.62724	1.67106	1.296546	0.860353
8	H	6	5	4	1.0851983	119.55816	-173.12388	0.62876	-3.594942	0.943701
9	Ru	6	5	4	2.2491718	74.584472	-53.174062	-0.222992	-0.967557	-0.192771
10	Cl	9	6	5	2.4831545	98.035625	-134.37472	-1.325314	-2.464067	-1.839404
11	Cl	3	2	1	3.7838809	124.686	-168.71994	1.647236	4.001772	0.761266
12	C	9	6	5	3.1464284	152.02405	15.528788	-1.691411	1.80671	-0.410027
13	C	12	9	6	2.361594	65.415497	-99.454701	-3.131123	-0.0526	-0.192491
14	C	12	9	6	1.4212443	152.16468	-70.048614	-2.779346	2.678013	-0.132243
15	C	13	12	9	1.3876637	92.35395	167.99427	-4.231613	0.755979	0.053948
16	H	13	12	9	1.0820903	145.4112	-15.791999	-3.210913	-1.129825	-0.256829
17	C	14	12	9	1.3834846	119.69848	-26.703418	-4.035633	2.150779	0.108167
18	H	14	12	9	1.0835784	118.39505	154.51351	-2.597846	3.746277	-0.13571
19	H	15	13	12	1.083463	120.15153	178.24345	-5.209598	0.313783	0.201935
20	H	17	14	12	1.0861884	119.86414	-179.78493	-4.869732	2.81437	0.317287
21	N	13	12	9	1.3624257	30.676249	-7.6938851	-1.87387	0.441458	-0.369763
22	N	12	9	6	1.3504653	84.111423	90.874602	-0.465696	2.273108	-0.732288
23	H	22	12	9	1.0118092	115.81527	11.533506	0.235225	1.57057	-0.929539
24	H	22	12	9	1.0315275	123.96967	-136.22147	-0.063535	3.145225	-0.355821
25	H	1	2	3	1.0851084	119.34781	173.81112	2.184946	-2.696749	-0.767194
26	H	4	3	2	1.0856784	118.28514	-179.09652	0.069089	0.4015	2.498765
27	C	5	4	3	1.509237	121.83923	175.04228	-0.590923	-2.24333	3.041199
28	H	27	5	4	1.0955031	111.13266	148.84879	-1.117914	-3.143272	2.705771
29	H	27	5	4	1.1001288	111.21177	-91.205193	-0.004797	-2.512165	3.932528
30	H	27	5	4	1.0952588	111.06736	28.495286	-1.339881	-1.505934	3.349259
31	C	2	1	6	1.5246249	120.53511	172.51128	3.226722	-0.148517	-1.007379
32	H	31	2	1	1.1006886	106.72677	14.986868	3.384604	-0.948314	-1.746915
33	C	31	2	1	1.5503329	109.67927	-101.48049	4.555991	0.050054	-0.234627
34	H	33	31	2	1.0969178	111.34076	54.653601	4.848288	-0.863177	0.298102
35	H	33	31	2	1.097335	110.38907	175.00835	5.363916	0.319407	-0.926617
36	H	33	31	2	1.0960445	110.30574	-65.700824	4.453094	0.859143	0.497562
37	C	31	2	1	1.5428191	114.15816	134.08344	2.853447	1.13786	-1.77301
38	H	37	31	2	1.0976394	109.80032	-178.69206	3.668291	1.414747	-2.454314
39	H	37	31	2	1.0962544	110.70447	-59.776959	1.950974	0.982191	-2.375574
40	H	37	31	2	1.097882	112.13833	61.874682	2.684852	1.987005	-1.097826

Complex $\mathbf{1}^{2-}$ in the gas phase (singlet electronic state)

Tag	Symbol	NA	NB	NC	Bond	Angle	Dihedral	X	Y	Z
1	C							2.655109	1.703041	-0.729649
2	C	1			1.3623848			1.566003	2.237279	-0.109544
3	C	2	1		1.4846812	114.8762		0.834124	1.302779	0.782275
4	C	3	2	1	1.454839	119.45309	35.05734	1.576927	0.306823	1.539158
5	C	4	3	2	1.4445337	115.71457	-34.790833	2.738755	-0.2431	0.880054
6	C	5	4	3	1.4464341	114.39137	1.0737909	2.996928	0.306654	-0.432687
7	H	3	2	1	1.089665	117.43379	-174.49418	-0.09498	1.657675	1.227454
8	H	6	5	4	1.0888256	117.35848	-170.84742	3.764459	-0.176311	-1.035333
9	Ru	4	3	2	2.1083742	75.888341	-94.545375	0.979957	-0.714016	-0.206338
10	Cl	9	4	3	2.5853147	143.09187	159.76326	1.511185	-2.76803	-1.683726
11	Cl	3	2	1	6.1036545	107.71864	-135.68278	-5.133654	2.000317	-0.291813
12	C	9	4	3	3.2003492	103.3803	-64.618566	-2.211826	-0.766875	0.021614
13	C	12	9	4	2.3503808	64.415774	-103.93662	-1.125177	-2.79111	0.517554
14	C	12	9	4	1.4242238	154.10719	-90.762109	-3.459305	-1.332815	0.411385
15	C	13	12	9	1.3897037	92.416459	174.35781	-2.311322	-3.399795	0.909777
16	H	13	12	9	1.08159	145.29061	-9.4086037	-0.183227	-3.322359	0.49907
17	C	14	12	9	1.3838678	119.32498	-11.560331	-3.499443	-2.64165	0.859079
18	H	14	12	9	1.0862659	117.54556	168.17829	-4.340504	-0.701248	0.343672
19	H	15	13	12	1.0854272	120.03423	178.88482	-2.309191	-4.435924	1.233172
20	H	17	14	12	1.0879297	119.78439	179.84659	-4.447948	-3.080661	1.16107
21	N	13	12	9	1.3630092	31.135142	-3.3969441	-1.04506	-1.494626	0.104632
22	N	12	9	4	1.3530437	85.121997	80.271331	-2.1506	0.502783	-0.44201
23	H	22	12	9	1.0131567	117.12466	0.6378032	-1.23127	0.875569	-0.6478
24	H	22	12	9	1.0271507	120.20355	-172.60002	-2.997948	1.08242	-0.47458
25	H	1	2	3	1.0920208	121.76959	179.04975	3.266185	2.286063	-1.421878
26	H	4	3	2	1.0887982	122.68913	145.78367	1.27928	-0.017296	2.535067
27	C	5	4	3	1.5092471	122.85273	-179.35002	3.616508	-1.296061	1.511441
28	H	27	5	4	1.0963441	110.19644	146.25874	4.009564	-1.97183	0.742797
29	H	27	5	4	1.1054224	111.9389	-93.567352	4.475637	-0.851208	2.046195
30	H	27	5	4	1.0977275	111.09834	27.151422	3.050387	-1.904162	2.228885
31	C	2	1	6	1.5202442	123.23596	177.39059	1.135346	3.684953	-0.282509
32	H	31	2	1	1.1031517	107.118	3.2557624	1.819761	4.141747	-1.01726
33	C	31	2	1	1.5496555	111.77212	-114.19847	1.268468	4.485864	1.037435
34	H	33	31	2	1.0970785	110.6401	58.221954	2.302704	4.460509	1.40253
35	H	33	31	2	1.1002619	111.32559	179.09035	0.970316	5.536012	0.900064
36	H	33	31	2	1.0967326	110.26592	-61.004249	0.627401	4.049413	1.812913
37	C	31	2	1	1.5476864	112.63713	121.21556	-0.301756	3.816169	-0.841842
38	H	37	31	2	1.0995792	111.04266	-178.05423	-0.573378	4.87148	-0.988861
39	H	37	31	2	1.0954696	110.64364	-57.68011	-0.390411	3.299741	-1.803869
40	H	37	31	2	1.0959074	111.48316	62.116404	-1.039404	3.378185	-0.15989

Complex **2** in the gas phase (singlet electronic state)

Tag	Symbol	NA	NB	NC	Bond	Angle	Dihedral	X	Y	Z
1	C							1.251406	0.21945	-1.65745
2	C	1			1.419344			2.31627	0.028089	-0.73876
3	C	2	1		1.441193	117.5531		2.353544	-1.2153	-0.011
4	C	3	2	1	1.412128	120.8418	2.002931	1.386687	-2.21836	-0.24157
5	C	4	3	2	1.440612	121.8324	0.658726	0.337419	-2.05297	-1.21473
6	C	5	4	3	1.417505	117.0174	-3.22715	0.272683	-0.80632	-1.88628
7	H	3	2	1	1.080932	119.852	-174.079	3.090501	-1.36205	0.766028
8	H	6	5	4	1.084635	119.2195	-174.715	-0.55301	-0.61115	-2.56199
9	Ru	4	3	2	2.239039	72.59453	-56.2485	0.29063	-0.34668	0.314107
10	Cl	9	4	3	2.460525	122.4001	-44.4199	0.998262	1.090411	2.18178
11	Cl	9	4	3	2.49701	86.94032	-130.305	-0.96966	-1.73398	1.963999
12	C	9	4	3	3.188811	132.0088	156.3118	-2.68363	0.639924	-0.2766
13	C	12	9	4	2.356644	64.58671	-154.106	-1.10343	2.350713	0.08388
14	C	12	9	4	1.418907	152.9239	-134.664	-3.63652	1.614212	-0.67163
15	C	13	12	9	1.387778	92.51184	171.6907	-2.00192	3.342068	-0.28469
16	H	13	12	9	1.080466	145.7118	-13.0601	-0.10914	2.588329	0.433645
17	C	14	12	9	1.38615	119.9794	-17.3575	-3.29118	2.956617	-0.6817
18	H	14	12	9	1.081519	119.3945	163.8236	-4.63488	1.300259	-0.94439
19	H	15	13	12	1.082556	119.9299	178.6086	-1.70237	4.381841	-0.25198
20	H	17	14	12	1.085147	119.8742	-179.629	-4.02312	3.700808	-0.97833
21	N	13	12	9	1.36157	30.81011	-5.64644	-1.4058	1.023291	0.064096
22	N	12	9	4	1.364461	84.33196	31.45732	-2.98878	-0.68925	-0.23264
23	H	22	12	9	1.021538	115.3277	28.01162	-2.37865	-1.25845	0.356683
24	H	1	2	3	1.08458	119.5355	176.1233	1.156061	1.167536	-2.17548
25	H	4	3	2	1.083774	119.2211	-175.099	1.391088	-3.10929	0.37551
26	C	5	4	3	1.505485	120.6726	178.7751	-0.66363	-3.15061	-1.45884
27	H	26	5	4	1.093559	111.1039	160.6745	-1.56166	-2.76291	-1.94781
28	H	26	5	4	1.098118	110.5292	-79.2534	-0.23251	-3.92881	-2.10258
29	H	26	5	4	1.094634	110.5831	40.32787	-0.96016	-3.61801	-0.51447
30	C	2	1	6	1.527213	119.6806	177.9447	3.36443	1.123873	-0.55711
31	H	30	2	1	1.098973	106.7252	49.44226	2.816021	2.06357	-0.40232
32	C	30	2	1	1.551099	109.4746	-67.3311	4.199321	1.261488	-1.85708
33	H	32	30	2	1.095613	112.048	57.00331	3.570599	1.471912	-2.72932
34	H	32	30	2	1.095563	109.8727	177.1442	4.919706	2.080197	-1.75211
35	H	32	30	2	1.09694	110.7604	-63.7042	4.761134	0.340936	-2.05764
36	C	30	2	1	1.538997	114.2432	168.1515	4.287563	0.920264	0.657341
37	H	36	30	2	1.095418	109.414	-176.074	4.958231	1.781043	0.753276
38	H	36	30	2	1.093064	111.0603	-56.7922	3.708877	0.835555	1.580778
39	H	36	30	2	1.097793	111.4724	65.40645	4.916277	0.028137	0.53911
40	C	22	12	9	1.458239	122.9687	-176.621	-4.32572	-1.20581	-0.50138
41	H	40	22	12	1.096629	111.3711	63.78318	-4.63162	-1.00446	-1.53505
42	H	40	22	12	1.091536	108.1022	-177.559	-4.30662	-2.28763	-0.35729
43	H	40	22	12	1.099701	112.6939	-58.1612	-5.08646	-0.78495	0.172041

Geometry keys to Tables of Coordinates

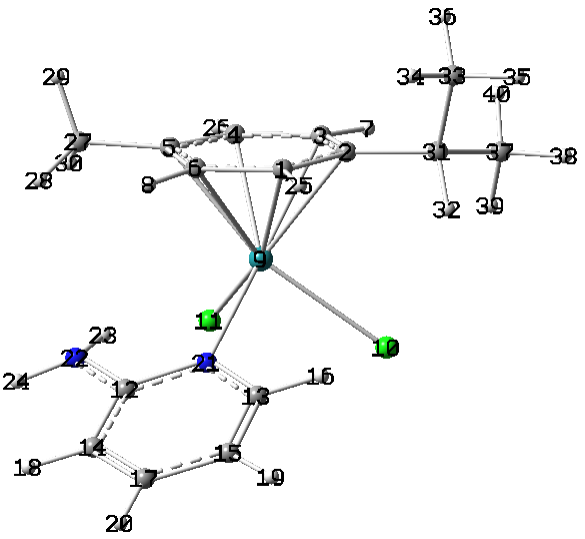

1, 1^{+}, 1^{2+}

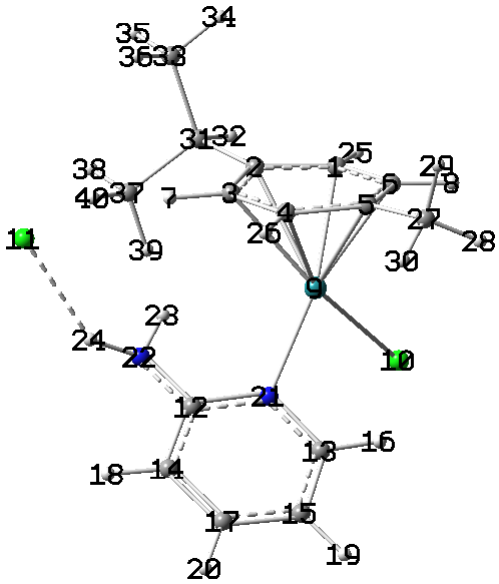

1^{-}

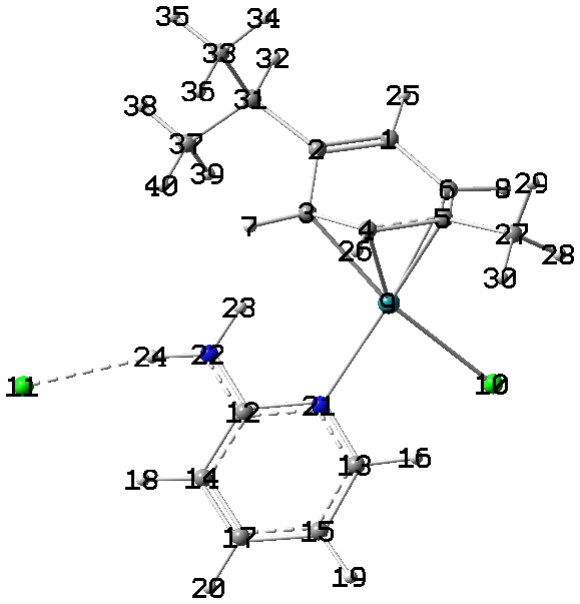

1^{2-}

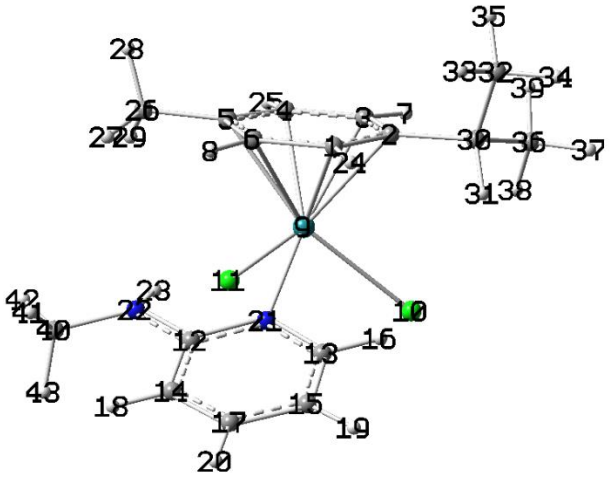

2

References for the Electronic Supporting Information

1. R. Aronson, M.R.J. Elsegood, J.W. Steed, D.A. Tocher, Polyhedron 10 (1991) 1727-1732.
2. F. White, P. Sadler, M. Melchart, CSD Private Communication, (2015).
3. M. V. Babak, D. Plazuk, S. M. Meier, H .J. Arabshahi, J. Reynisson, B. Rychlik, A. Blauz, K. Szulc, M. Hanif, S. Strobl, A. Roller, B. K. Keppler, C. G, Hartinger, Chem- Eur. J. 21 (2015) 5110-5117.
4. C. M. Standfest-Hauser, K. Mereiter, R. Schmid, K. Kirchner, Dalton Trans. 11 (2003) 2329-2334.
5. E. Smith, G. Dent, John Wiley & Sons Ltd, New Jersey, (2005).
6. J. Grau, V. Noe, C. Ciudad, M. J. Prieto, M. Font-Bardia, T. Calvet, V. Moreno, J. Inorg. Biochem., 109, (2012), 72-81.
7. R. During, Y. Omura, E. E. Mercer. J. Mol. Struct., 29, (1975), 53-63.
8. P. Chuklin, V. Chalermpanaphan, T. Nhukeaw, S. Saithong, K. Chainok, S. Phongpaichit, N. Leesakul, J. Organomet. Chem. 846 (2017) 242-250.
9. Govender, P., Antonels, N. C., Mattsson, J., Renfrew, A. K., Dyson, P. J., Moss, J. R., Smith, G. S., J. Organomet. Chem., 649, (2009), 3470-3476.
10. S. Grgurić-Šipka, I. Ivanović, G. Rakić, N. Todorović, N. Gligorijević, S. Radulović, Ž. L. Tešić, Eur. J. Med. Chem. 45 (2010) 1051-1058.
11. M. Patra, T. Joshi, V. Pierroz, K. Ingram, M. Kaiser, S. Ferrari, G. Gasser, Chem. Eur. J. 19 (2013) 14768-14772.
12. K. S. A. Shweshein, F. Andrić, A. Radoičić, M. Zlatar, M. Gruden-Pavlović, Ž. Tešić, D. Milojković-Opsenica, Sci. World J. 2014 (2014).
13. N. Gligorijević, S. Aranđelović, L. Filipović, K. Jakovljević, R. Janković, S. Grgurić-Šipka,, Ž. L. Tešić, J. Inorg. Biochem. 108 (2012) 53-61.
14. K. G. Liu, X. Q. Cai, X. C. Li, D. A. Qin, M. L. Hu, Inorganica Chim. Acta. 388 (2012) 78-83.
15. R. E. Morris, E. R. Aird, P. del Socorro Murdoch, H. Chen, J. Cummings, N. D. Hughes, S. Parsons, A. Parkin, G. Boyd, J. I. Duncan, P. J. Sadler, J. Med. Chem. 44 (2001) 3616-3621.
16. R. E. Aird, J. Cummings, A. A. Ritchie, M. Muir, R. E. Morris, H. Chen, D. I. Jodrell, D, Br. J. Cancer. 86 (2012) 1652-1657.
17. R. Sáez, J. Lorenzo, M. J. Prieto, M. Font-Bardia, T. Calvet, N. Omeñaca and V. Moreno, J. Inorg. Biochem., 136, (2014), 1-12.
18. X. W. Yan, Y. R. Xie, Z. M. Jin, M. L. Hu, L. P. Zhou, Appl. Organomet. Chem. 32 (2018) 1-8.
19. J. Zhao, K. E. Prosser, S. W. Chang, S. P. Zakharia, C. J. Walsby, Dalton Trans. 45 (2016) 18079-18083.
20. M. V. Babak, D. Plazuk, S. M. Meier, H .J. Arabshahi, J. Reynisson, B. Rychlik, A. Blauz, K. Szulc, M. Hanif, S. Strobl, A. Roller, B. K. Keppler, C. G, Hartinger, Chem- Eur. J. 21 (2015) 5110-5117.
21. C. A. Vock, C. Scolaro, A. D. Phillips, R. Scopelliti, G. Sava, P. J. Dyson, J. Med. Chem., 49 (2006) 5552-5561.
22. J. Zhao, D. Zhang, W. Hua, W. Li, G. Xu, S. Gou, Organometallics 2018.